Order Number 9224842

Surface tension anisotropy of succinonitrile and pivalic acid: New measurements and comparison with microscopic solvability theory

Muschol, Martin, Ph.D.

City University of New York, 1992

U·M·I
300 N. Zeeb Rd.
Ann Arbor, MI 48106

SURFACE TENSION ANISOTROPY OF SUCCINONITRILE AND PIVALIC ACID: NEW MEASUREMENTS AND COMPARISON WITH MICROSCOPIC SOLVABILITY THEORY

by

Martin Muschol

A dissertation submitted to the Graduate Faculty in Physics in partial fulfillment of the requirements for the degree of Doctor of Philosophy, The City University of New York.

1992

This manuscript has been read and accepted for the Graduate Faculty in Physics in satisfaction of the dissertation requirement for the degree of Doctor of Philosophy.

April 2, 1992 — Date

Chair of Examining Committee

April 9, 1992 — Date

Executive Officer

J. Gollub

J. Koplik

R. Marino

O. Martin

Supervisory Committee

The City University of New York

Abstract

Surface Tension Anisotropy of Succinonitrile and Pivalic Acid: New Measurements and Comparison with Microscopic Solvability Theory

by Martin Muschol

Adviser: Professor Herman Z. Cummins

Careful determinations of the surface tension anisotropy parameter ε_4 for succinonitrile (SCN), pivalic acid (PVA) and a PVA/1% ethanol mixture are reported. The size of the higher harmonic ε_8 is estimated. Our measurements are based on the observations of equilibrium shapes of isolated, single crystals in contact with their melts. The influence of thermal gradients on the measurements as well as orientation effects are analyzed in detail. Numerical interpolation routines, previously employed by Dougherty and Gollub, are utilized to enhance the optical resolution in our experiments. The anisotropy values found for SCN, PVA and PVA/1% ethanol are $\varepsilon_4 = 0.0055\pm0.0015$, 0.025 ± 0.002, and 0.026 ± 0.002 respectively. From these values, the selection parameter σ^*_{th} predicted by microscopic solvability theory for the three-dimensional axisymmetric case was computed and compared to the σ^*_{exp} values determined directly from previous dendritic growth experiments. We find that $\sigma^*_{th}/\sigma^*_{exp}$ is 0.56 ± 0.2 for SCN and 2.14 ± 0.5 for PVA. Possible sources for these discrepancies are discussed.

Acknowledgements

I would like to thank Professor Cummins for his guidance and advice throughout the course of my dissertation research. Thanks also to all the members of my thesis committee, especially Olivier Martin, who always made himself available for questions and discussions. I've enjoyed the many hours I spend with all my lab-mates, Lloyd Williams, Chester Chen, Gen Li, Xiaoke Chen, Tracy Turner, Weimin Du and Dongning Lu. The friendly support I received from our electronic shop and our machine shop, in particular the expert advice of Joe Altman, was essential to the success my work. Of course, I cannot forget my two closest friends, Marianne Sommer and Wolfgang Polifke. They helped me through the ups and downs of my life in- and outside of City College. There are many friends outside of school who gave me their sympathy. I'd like to thank them all. I'm very grateful for the support of my wife's family. They created a sense of family for me six thousand miles away from my parents home. I thank my parents for teaching me to value education and knowledge and my brothers and sisters for their steady support. I'm especially indebted to my wife Elizabeth for her trust in me and the love she gave to me, even when I was at my most unbearable.

Table of Contents

List of Tables

List of Figures

1. Introduction

Complex spatial patterns arise in a surprising variety of fields and over a wide range of length scales. Rayleigh-Bénard convection or dielectric breakdown patterns in physics, population growth or the spread of epidemics in biology, cloud formations and lightning patterns in meteorology, the shape and distribution of galaxies in astronomy are just a few examples. All these systems are dissipative, are modeled by nonlinear equations and are far away from thermodynamic equilibrium.

Moving phase boundaries are frequently studied examples of pattern forming systems in physics [P1]. Saffman-Taylor fingers in fluid mechanics and dendrites in solidification processes fall into this class. The Saffman-Taylor system consists of a long channel between two narrowly spaced plates (see Fig.6). A low viscosity fluid is pushed with constant pressure into one end of the channel displacing a fluid of higher viscosity inside the channel. While the low viscosity fluid displaces the high viscosity fluid the planar interface separating the two phases breaks up and eventually forms a single finger propagating down the length of the channel with constant speed and shape. The system is modeled by the Laplace equation for the pressure field in the two fluids. The speed of propagation is locally set by the gradient of the pressure. In addition, surface tension produces a pressure drop at the interface proportional to the local curvature.

Dendrites result from quenching the liquid temperature in a crystal-melt system. The solid-liquid interface starts to grow and breaks up in a similar fashion to the fluid interface of Saffman-Taylor experiments (see Fig.1). The system then reaches a new steady state of nearly parabolic shape with constant speed and tip radius propagating into the undercooled

melt. In contrast to the Saffman-Taylor problem, secondary arms grow on the side of the main tip and provide a time-dependent feature to this interface. The whole interface appears tree-shaped, and is designated as a dendrite, Greek for 'tree'. The macroscopic equation describing the system is the thermal diffusion equation. The thermal gradient at the interface determines the local interface velocity, and is analogous to the pressure gradient in the Saffman-Taylor problem. Surface tension suppresses the local melting temperature of the curved sections of the interface, again in analogy with the reduced pressure induced by surface tension in Saffman-Taylor fingers. The resulting steady state equations for both dendrites and Saffman-Taylor fingers are therefore formally very similar. There are also important differences. The presence of sidebranches in dendritic growth was already mentioned. Dendrites grow at a size fixed by the driving force (the melts undercooling) only, while the size of the Saffman-Taylor finger is set by the width of the growth channel, an external boundary condition. Most important, dendrites grow into crystallographically preferred directions (see Fig.27), indicating the importance of the underlying lattice structure in the pattern selection process.

Early theoretical approaches to these two problems produced solutions with a continuum of possible growth speeds for a given driving force, not the unique velocities observed experimentally. The reason was that these theories neglected the effects of surface tension across the phase boundary. Attempts to include this microscopic effect as a small perturbation to the macroscopic evolution equations proved to be mathematically inadequate. Over the last few years a new approach has been developed to resolve the question of how to treat surface tension and obtain the correct selection rules. The character of surface tension as a singular

perturbation to the macroscopic steady-state equations played a key role in both cases. Surface tension destroys the continuum of steady state solutions. For the Saffman-Taylor problem the constraints of the channel geometry selects the experimentally observed steady state. In free dendritic growth the presence of a weak anisotropy in the crystal-melt surface tension produces the necessary selection mechanism. This theoretical framework provides a very appealing answer since it helps to unify the approach to both problems while explaining the observed differences as well.

For the Saffman-Taylor system experimental confirmation of the theory was swift (eg. [C12,T5]). The first experiments on dendritic growth specifically designed to test the predictions of the new theory raised similar hopes for the solidification problem [D4], but further tests were hindered by the difficulties involved in measuring the central control parameter for dendritic growth: surface tension anisotropy. Several preliminary measurements existed, but almost all materials had only been examined once. The only material subjected to two investigations of its anisotropy, pivalic acid, yielded anisotropy values that differed by an order of magnitude. The main purpose of our study was therefore to measure the surface tension anisotropy with high accuracy for two commonly used dendritic growth materials: succinonitrile (SCN) and pivalic acid (PVA). The results of these measurements provided the basis for our comparison of existing experimental results with the theoretical predictions.

The overall layout of this dissertation is as follows. In chapter 2 we will review the theory of dendritic growth in some detail. After an introduction to the early stages of crystal-growth instability, the Mullins-Sekerka instability, we will focus on the development of the steady-state theory of dendritic growth. Details of the newly developed theories of

surface tension as a singular perturbation will be discussed, stressing the role that anisotropy plays in the selection mechanism of dendritic growth.

Our measurements of surface tension anisotropy are based on the observation of equilibrium crystal shapes. In chapter 3 we will explore the theoretical connections between surface tension anisotropy and resulting crystal shape anisotropies. We will also consider the influence of external temperature gradients on the observed equilibrium shapes.

In chapter 4 we review the existing literature on experiments in dendritic growth into undercooled melts or supercooled binary liquids. Again, we will focus on experiments concerning steady-state growth. In the same chapter we will also review previous measurements of surface tension anisotropy.

Chapter 5 introduces our experimental procedures and measurements. Details of the experimental apparatus, sample preparation and data-processing are presented. The results of our surface tension anisotropy measurements are summarized.

In the final chapter we compare our results with existing values of surface tension anisotropy. We then compare theoretical prediction based on measured surface tension anisotropy values with existing data on steady-state dendritic growth. The observed discrepancies between theory and experiments are explored.

2. Theory of Pattern Formation During Solidification

2.1. Overview of the Phenomena

We first consider the following system: a container filled with a pure material at its melting point. Part of the material is solid and the rest is molten, with a single planar interface separating the two phases. As we start to cool the molten side of the material the morphology of the initially flat crystal-melt interface displays a series of transitions (see Fig. 1) which are reminiscent of instabilities observed in fluid flows [B1,P1]. This series of transitions can roughly be divided into four stages: The Mullins-Sekerka instability, first coarsening phase, steady-state dendritic growth, and the final coarsening stage.

The initial stage is the destabilization of the planar interface, known as the Mullins-Sekerka instability [M1,M2,C1]. The interface develops small, wavy deformations described by a characteristic wavelength λ. These deformations are caused by fluctuations with a broad band of wavelengths which become unstable against infinitesimally small perturbations of the solid-liquid interface. As the amplitude of these initial deformations of the interface rapidly grows in size, they start to interact and compete with each other through the thermal diffusion field. Most of the initial perturbations get squeezed out leaving a few remaining. A typical increase in length scale during this coarsening process is of the order of ten, as observed in SCN [H1]. This stage of the solidification is still poorly understood. Recent numerical studies [J1,J2] suggest that this coarsening regime shows self-similar behavior with a characteristic length scale that grows linearly in time.

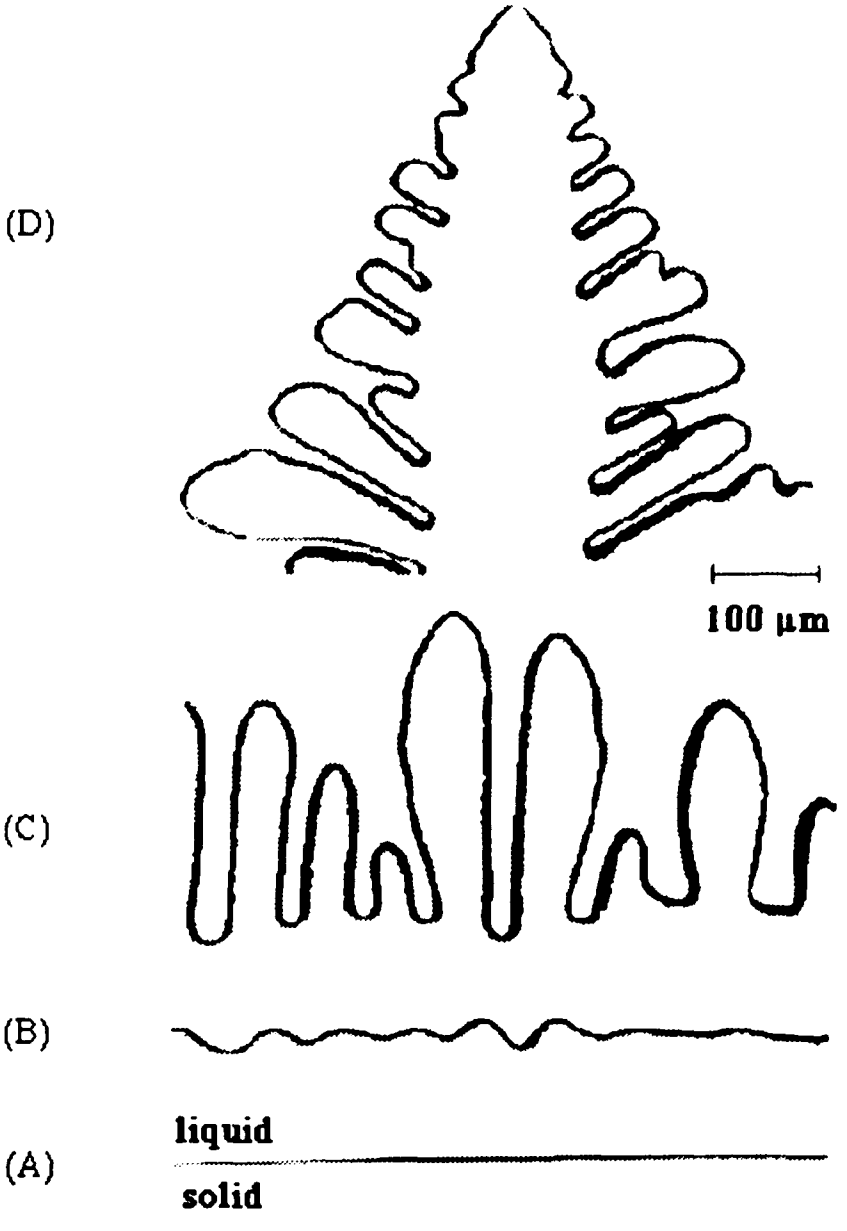

Fig. 1: Different stages of crystal growth in a SCN-dye system during directional solidification. The sequence of instabilities of a pure system during free growth is identical to the one observed in this binary system: (A) flat interface separating the solid (bottom) and liquid (top) phase. (B) initial instability (C) coarsening stage (D) dendritic steady-state

In the next stage the system slowly settles into a new steady state. A set of fingers with parabolically shaped tips emerges. They are equally spaced, grow at a constant speed v* and with a parabolic tip of constant tip radius ρ. It is not quite accurate to describe this stage as steady state since there is a secondary instability developing further down the sides of the parabolic tips. This sidebranching instability causes bumps to develop on the sides of each steady-state tip. When observed in a reference frame moving with the steady-state tip this irregular array of bumps becomes visible a few tip radii behind the tip and is moving down along the side of the parabolic finger with speed -v*, while growing in size [D1,H2]. The origin of this instability is similar to the Mullins-Sekerka instability [P2]. The flat portions of the finger are unstable against perturbation originating at the tip. The perturbations are therefore amplified and remain behind the growing tip region. It is the combined pattern of the steady state tip region and the secondary sidebranches emerging from its side that is called a dendrite.

In the late stages of solidification the liquid regions between the dendrites solidify, changing the morphology and characteristic length scale of the pattern in the system [G1]. This second coarsening stage will, in the case of a pure material, leave no visible trace of the dendritic growth structure [K1]. The only indirect evidence is the presence of grain boundaries wherever the different branches of one dendrite or two different dendrites coalesce.

The theoretical review presented in the rest of this section briefly discusses the initial Mullins-Sekerka instability and then focuses on the steady state theory of dendritic growth.

2.2 The Mullins-Sekerka Instability

The first detailed theoretical analysis of the initial morphological instability in crystal growth dates back almost thirty years to two articles by Mullins and Sekerka in 1963 and 1964 [M1,M2]. We review their argument for the case of a pure melt. The starting point in their analysis is the steady-state solution for the one-dimensional planar interface. As we will see, this steady-state only exists for a single undercooling and is an unrealistic starting point for most experiments. More general theories for arbitrary undercoolings have been developed [B24, P6, P7], but their presentation is beyond the scope of this thesis. We will limit ourselves therefore to the original ideas of Mullins and Sekerka.

To test the stability of the planar steady-state they add a small perturbation of the form $\exp[ikx+\omega_k t]$ and calculate the amplification rate ω_k for each of the modes k. If ω_k is negative the corresponding k-mode will decay and the planar interface is stable against perturbations of that wave number. If ω_k is positive, however, a k-mode with initial infinitesimal amplitude will grow exponentially in time and destroy the stability of the planar morphology. To carry out this analysis we must first write down the equations governing the solidification process together with the relevant boundary conditions.

2.2.1 The Basic Equations

The solidification of a pure melt is controlled by the rate of heat removal from the sample by thermal diffusion which obeys the diffusion equation

$$D_T \nabla^2 T = \partial_t T \tag{2.1}$$

When solving Eq. (2.1) we have to allow for different thermal diffusivities D_T in the two phases. We will use the symbol D_T (D_T') for the thermal diffusivities of the liquid (solid) phase. The solidifying interface acts as a heat source, releasing latent heat L at a rate of Lv_n, where v_n is the velocity component of a given interface segment along its normal vector $\hat{n}$ and $\hat{n}$ points from the solid into the liquid. Continuity of the heat flux requires that the latent heat is conducted away into the two phases at the same rate as it is generated [L1]:

$$Lv_n = \left[D_T' \, c_p' \nabla T' \big|_{sol} - D_T \, c_p \nabla T \big|_{liq} \right] \cdot \hat{n} \tag{2.2}.$$

The lowering of the interface temperature of the solidifying front due to surface tension and kinetic effects is given by [B2]

$$T_i = T_m \left(1 - \frac{\gamma}{L} \kappa \right) - \beta \, v_n \tag{2.3}.$$

Here, T_i is the actual interface temperature, T_m is the bulk melting temperature, γ is the solid-liquid interface tension, κ is the local curvature of the interface and β is the kinetic coefficient. The first term in brackets on the r.h.s. is the *Gibbs-Thompson relation* describing the lowering of the bulk melting temperature of a curved interface segment due to surface tension. We will derive a generalized version of this relation in chapter 3.1. The second term accounts for kinetic effects: the crystal interface has to be cooled below T_m in order to grow. For microscopically rough interfaces and small undercoolings the Wilson-Frenkel theory [W1]

predicts a linear relation between undercooling and growth speed as given in Eq. (2.3). The coefficient β is difficult to measure but for small undercoolings the kinetic term is generally negligible compared to the Gibbs-Thompson term [O1]. We will therefore exclude the kinetic term from all derivations except where explicitly mentioned. Finally the boundary condition in the melt far from the interface is

$$T \rightarrow T\infty \qquad \text{for} \quad z \rightarrow \infty \tag{2.4}$$

2.2.2 The Steady State Planar Interface Solution

We next transform Eqn. (2.1) into a frame moving with a constant speed v in the positive z-direction. Note that the unprimed symbol z now stands for the coordinate of the moving frame

$$D_T \nabla^2 T = (\partial_t - v\, \partial_z)\, T \tag{2.5}$$

A steady-state interface moving at constant speed v will be stationary in this reference frame and we can impose the boundary conditions of eqn.(2.2) and (2.3) easily. Dropping the time derivative from (2.5) we get the steady state equation:

$$(\nabla^2 + \frac{v}{D_T}\partial_z)T = 0 \tag{2.6}$$

The solution to the steady state problem is

$$T_0(z) = T_m - \frac{L}{c_p}\left[1 - \exp\left(-\frac{2z}{l_D}\right)\right] \qquad z>0 \tag{2.7.a}$$

$$T_0'(z) = T_m \qquad z<0 \tag{2.7.b}$$

where we already imposed the energy conservation (2.2) and the boundary condition of Eq. (2.4).The solid-liquid interface is at the origin z=0 of the moving frame and T(z) is the temperature in the liquid while the primed

T'(z) describes the temperature field inside the solid. The parameter $l_D \equiv 2D_T/v$ has the units of length and is called the *diffusion length*. A plot of Eq.(2.7) is shown in Fig.2 . The temperature decays in a few diffusion lengths to the so-called *unit undercooling* L/c_p. It is the only undercooling for which a planar steady state solution exist. For undercoolings less than L/c_p, the interface velocity is time-dependent and diminishes with $v \propto t^{-1/2}$ [Z1]. A peculiarity of the steady state solution is that the steady state velocity v is still arbitrary, and in practice is only limited by kinetic effects. They enter through Eq.(2.3) which we have not imposed on Eqs. (2.7).

2.2.3 Linear Stability Analysis in 2 Dimensions

Following Mullins and Sekerka we next add a small sinusoidal perturbation to the flat interface of the form

$$\zeta(x,t) = \hat{\zeta}_k \exp[ikx + \omega_k t] \tag{2.8}$$

where $\hat{\zeta}_k$ is the amplitude of the mode with wave vector k. For the temperature field the corresponding responses have the form

$$T_1(x,z,t) = T_0(z) + \hat{T}_k \exp[-qz]\exp[ikx + \omega_k t] \tag{2.9.a}$$

$$T_1'(x,z,t) = T_0'(z) + \hat{T}_k' \exp[q'z]\exp[ikx + \omega_k t] \tag{2.9.b}$$

where $T_0(z)$ ($T_0'(z)$) is the steady state temperature profile in the liquid (solid) phase as given in Eq. (2.7). Putting Eqs. (2.9) into (2.6) we obtain the relationship for the coupling of the wave vectors in the x- and the z-direction.

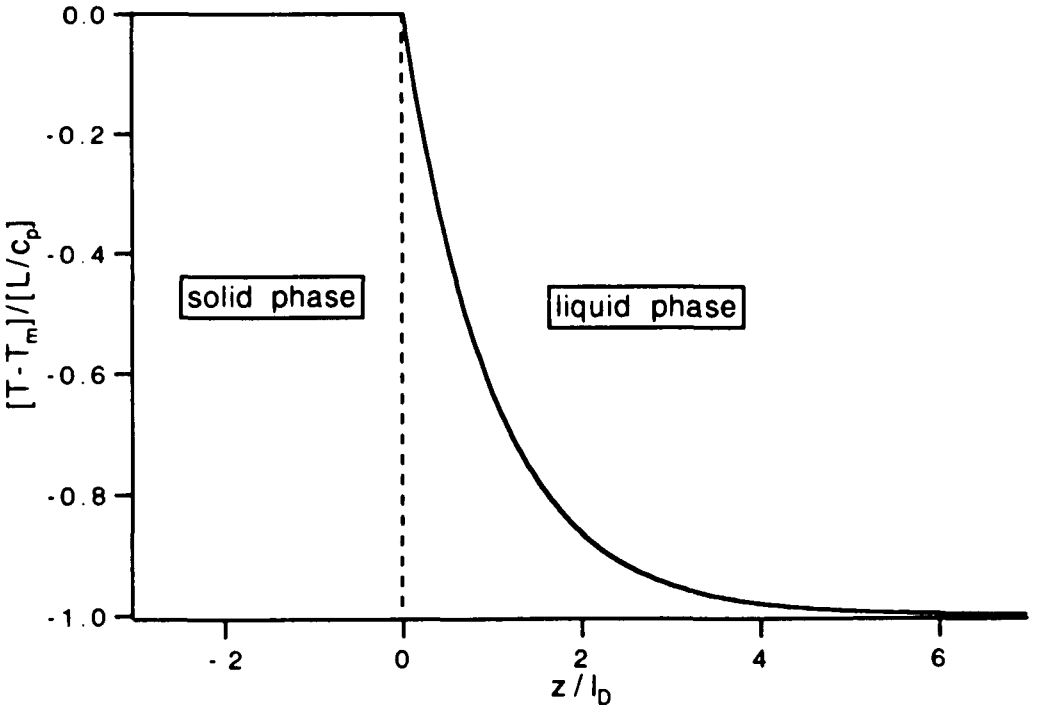

Fig. 2: Steady-state temperature profile in the moving frame of the interface. The natural unit of length chosen is the diffusion length $l_D=2D_T/v$ while temperature is scaled by the undercooling at infinity $\Delta T=L/c_p$.

$$q^2 - 2q / l_D - k^2 = 0 \qquad (2.10.a)$$

$$q'^2 + 2q'/ l_D - k^2 = 0 \qquad (2.10.b)$$

When imposing the boundary conditions we expand the resulting equations up to first order in the small amplitudes $\hat{\zeta}_k, \hat{T}_k$ and $\hat{T}'_k$. The l.h.s. of Eq.(2.3) then takes the form

$$T_l(x,\zeta,t) = T_m - \frac{L}{c_p}\left[1 - \exp\left(-\frac{2\zeta}{l_D}\right)\right] + \hat{T}_k \exp(-q\zeta)\exp(ikx + \omega_k t)$$

$$\cong T_m - \frac{2L}{c_p l_D}\hat{\zeta}_k \exp(ikx + \omega_k t) + \hat{T}_k \exp(ikx + \omega_k t) \qquad (2.11.a)$$

$$T'_l(x,\zeta,t) = T_m + \hat{T}'_k \exp(q'\zeta)\exp(ikx + \omega_k t)$$

$$\cong T_m + \hat{T}'_k \exp(ikx + \omega_k t). \qquad (2.11.b)$$

Evaluating the r.h.s. of Eqs. (2.11) we only keep the Gibbs-Thompson term. The curvature κ is given by

$$\kappa(\zeta) = -\frac{\partial_x^2 \zeta}{[1 + (\partial_x \zeta)^2]^{3/2}} \cong -\partial_x^2 \zeta \qquad (2.12)$$

Applied to the interface in Eq. (2.8) we obtain for the r.h.s. of (2.3), excluding the kinetic term

$$T_m\left(1 - \frac{\gamma}{L}k^2 \hat{\zeta}_k \exp(ikx + \omega_k t)\right) \qquad (2.13)$$

Together we get two relations between the perturbation amplitudes $\hat{\zeta}_k, \hat{T}_k$ and $\hat{T}'_k$.

$$\hat{T}_k = \left(\frac{2L}{c_p l_D} - \frac{T_m \gamma}{L}k^2\right)\hat{\zeta}_k \qquad (2.14.a)$$

$$\hat{T}'_k = -\frac{T_m \gamma}{L}k^2 \hat{\zeta}_k \qquad (2.14.b)$$

Finally we have to insure heat-flux conservation. The l.h.s. of (2.2) yields

$$Lv_n \equiv L(v + \partial_t \zeta) = Lv + \omega_k \hat{\zeta}_k \exp(ikx + \omega_k t) \tag{2.15}$$

while on the r.h.s

$$\begin{aligned}\nabla T \cdot \hat{n}|_{z=\zeta} &\equiv \partial_z T|_{z=\zeta} \\ &= -\frac{2L}{c_p l_D}\exp\left(-\frac{2\zeta}{l_D}\right) - \hat{T}_k q \exp(-q\zeta)\exp(ikx + \omega_k t) \\ &\equiv -\frac{2L}{c_p l_D}\left(1 - \frac{2}{l_D}\hat{\zeta}_k \exp(ikx + \omega_k t)\right) - \hat{T}_k q \exp(ikx + \omega_k t) \end{aligned} \tag{2.16.a}$$

$$\begin{aligned}\nabla T' \cdot \hat{n}|_{z=\zeta} &\equiv \hat{T}'_k q \exp(q\zeta)\exp(ikx + \omega_k t) \\ &\equiv \hat{T}'_k q \exp(ikx + \omega_k t) \end{aligned} \tag{2.16.b}$$

Introducing the quantity $\mu \equiv D_T c_p / D'_T c'_p$ we can write Eq.(2.2) as

$$\omega_k \hat{\zeta}_k = -\frac{2v}{l_D}\hat{\zeta}_k + \frac{D_T c_p}{L}\left[\mu q' \hat{T}'_k + q\hat{T}_k\right] \tag{2.17}.$$

We make the approximation that the wavelength of the front perturbation is much smaller than the diffusion length, or $kl_D << 1$. Under this condition Eqs.(2.10) yield $q \approx q' \approx k$. Eliminating the T_k's via (2.14) we arrive at the final expression for the growth-rates of the Fourier modes as a function of wavenumber k:

$$\omega_k = vk\left[1 - \frac{1}{2} d_o l_D (1 + \mu) k^2\right] \tag{2.18}$$

where $d_o \equiv \frac{\gamma T_m}{L^2 / c_p}$ is the *capillary length*, a microscopic length scale related to the surface tension γ of the material.

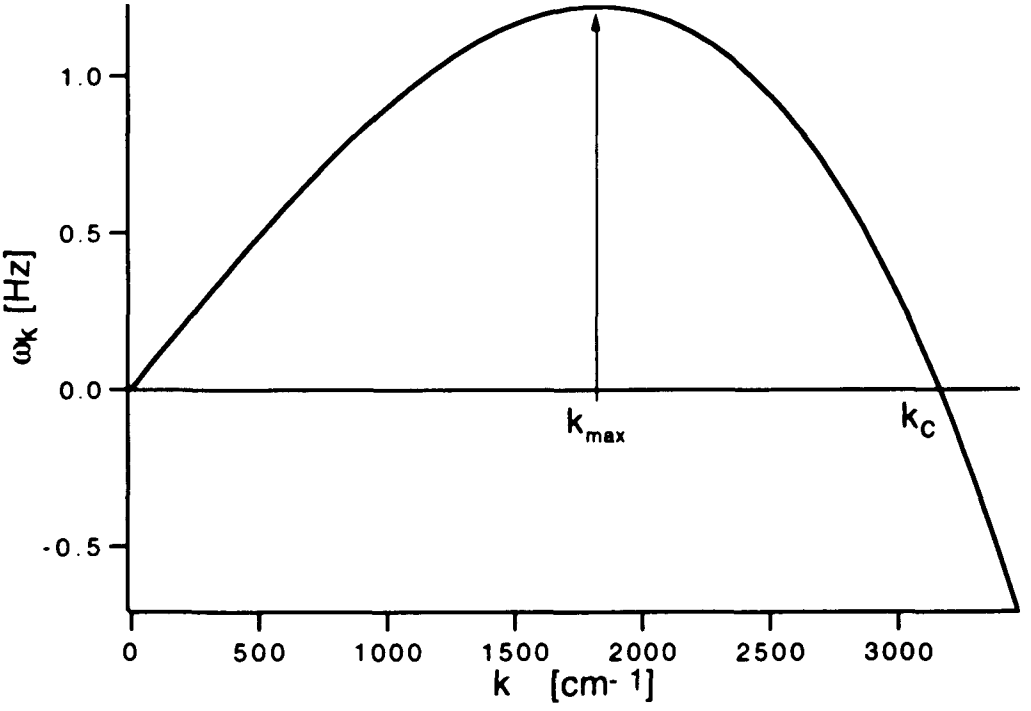

Fig. 3: Mullins-Sekerka relation for an interface moving with v = 10 μm/s. All other material parameters are those of SCN.

2.2.4 Discussion of the Dispersion Relation

To explore the underlying physics leading to the instability we will look at the case of zero surface tension. Then Eq. (2.18) is reduced to $\omega_k = vk$. An interface perturbation as given by Eq. (2.8) will be amplified by the diffusion field and grow at a rate increasing linearly with its wave vector k. Fig.3 shows a plot of the full Mullins-Sekerka relationship (2.18).The effect of surface tension is to suppress the instability at small length scales (large k). The critical wavevector $k_c>0$ for which $\omega_k=0$ is $k_c=(d_0 l_D)^{-1/2}$. It is the geometric mean of the two intrinsic length scales in the problem: the diffusion length l_D (typically $\approx$1 cm) and the capillary length d_o ($\approx 10^{-8}$ cm). This, a posteriori, justifies our assumption $kl_D<<1$. The k-mode with the maximum growth rate is $k_{max} = (3d_0 l_D)^{-1/2}$ and the corresponding wavelength is

$$\lambda_{max} = 2\pi(3d_0 l_D)^{1/2}. \tag{2.19}$$

λ_{max} is the typical length scale we expect for structure to emerge in the early stages of the instability.

We have also made the 'quasi-stationary' approximation. Instead of putting our perturbative ansatz (2.8) and (2.9) back into the time-dependent diffusion equation (2.5) we used the steady-state equation (2.6). This is acceptable as long as the diffusion field relaxes much faster than the interface can respond. We can estimate the relaxation time of the diffusion field as

$$\omega_{Diff} \approx \partial_t T_l \approx \partial_z^2 T_l \approx D k_{max}^2 \tag{2.20}$$

while the time scale for the interface relaxation is of the order of

$$\omega_{int} \approx v k_{max} \tag{2.21}$$

and their ratio

$$\frac{\omega_{Diff}}{\omega_{int}} \approx k_{max} l_D >> 1 \qquad (2.22)$$

The analysis is therefore self-consistent with the assumptions and approximations we have made along the way.

We should comment here on the underlying simplifications of this Mullins-Sekerka analysis. First of all, the analysis is done starting from the steady-state solutions of the planar interface, as mentioned in the introduction to this section. In practice, experimentally accessible undercoolings are small compared to the unit undercooling assumed. We also have neglected kinetic effects, which have been included in later analyses . There are several papers dealing with these issues and we refer the reader to them for a more detailed discussion [B23,C2,C3,P6,P7,S1, S2].

2.3. Dendritic Steady-State Theory before Microscopic Solvability

Before discussing steady-state theories of dendritic growth we comment on the general structure of the problem. The diffusion equation together with the appropriate boundary conditions (Eq.(2.1)-(2.4)) were introduced in section 2.2. The solidification problem was first formulated by Stefan [C4] who studied the freezing dynamics of ice, neglecting surface tension effects. Even though the diffusion equation itself is linear, the boundary conditions (2.2) and (2.3) make the problem nonlinear. In addition, the shape of the crystal-melt interface is not known in advance but is part of the solution we are looking for. This makes the equations hard to solve and there are no exact analytical solutions available except for a few special cases.

2.3.1 Ivantsov Solution and Maximum Growth-Speed Hypothesis

In 1947 Ivantsov [I1] derived solutions to the Stefan problem for zero surface tension. The solid-liquid interface is then an isotherm and a parabola of revolution satisfies the equations. The forward velocity v of the propagating parabola and the radius of curvature ρ at the tip are related to the dimensionless undercooling of the melt far from the interface. In three dimensions this relationship is [L1]

$$\Delta = p \exp(p) E_1(p) \tag{2.23}$$

where $\Delta \equiv (T_i - T_\infty)/(L/c_p)$ is the *dimensionless undercooling*, $p \equiv \rho v/2D$ is the *peclet number* and $E_1(x)$ is the exponential integral defined as

$$E_1(x) = \int_x^\infty \frac{\exp(-y)}{y}\, dy \tag{2.24}$$

The equivalent relationship in two dimensions is [B3]

$$\Delta = \sqrt{\pi p}\, \exp(p)\, \mathrm{erfc}\left(\sqrt{p}\right) \tag{2.25}$$

where erfc(x) is the complimentary error function

$$\mathrm{erfc}(x) = \frac{2}{\sqrt{\pi}} \int_x^\infty \exp(-y^2) dy \tag{2.26}$$

Eq. (2.23) and (2.25) are plotted in Fig.4 . Note that the undercooling only fixes the product of v and ρ. In experiments, however, a fixed undercooling produces a unique tip radius and growth velocity [G2]. This is called the *selection problem of dendritic growth.*

An obvious reason for the lack of a selection criterion in the Ivantsov analysis is the exclusion of surface tension. Just as in the case of the Mullins-Sekerka analysis in chapter 2.2, surface tension provides an additional length scale for the problem and produces a natural cut-off length: Ivantsov parabolas with very small tip radii ρ will therefore tend to be suppressed. For a given undercooling, the tip velocity of Ivantsov parabolas increases with decreasing tip radius since ρv is constant. One therefore might expect surface tension to make the growth speed vs. tip radius curve bend over at small ρ and to introduce a maximum speed at some length scale yet to be determined. These considerations naturally led to the idea of selection of the fastest growing dendrite at a given undercooling and is called the *maximum growth speed hypothesis.* As straightforward as this concept appears it should be derived from the full set of equations. Since no analytical solutions to the full problem were available, however, various approximations have been attempted. Sekerka et.al [S3] replaced the varying curvature of the parabola by its fixed three-

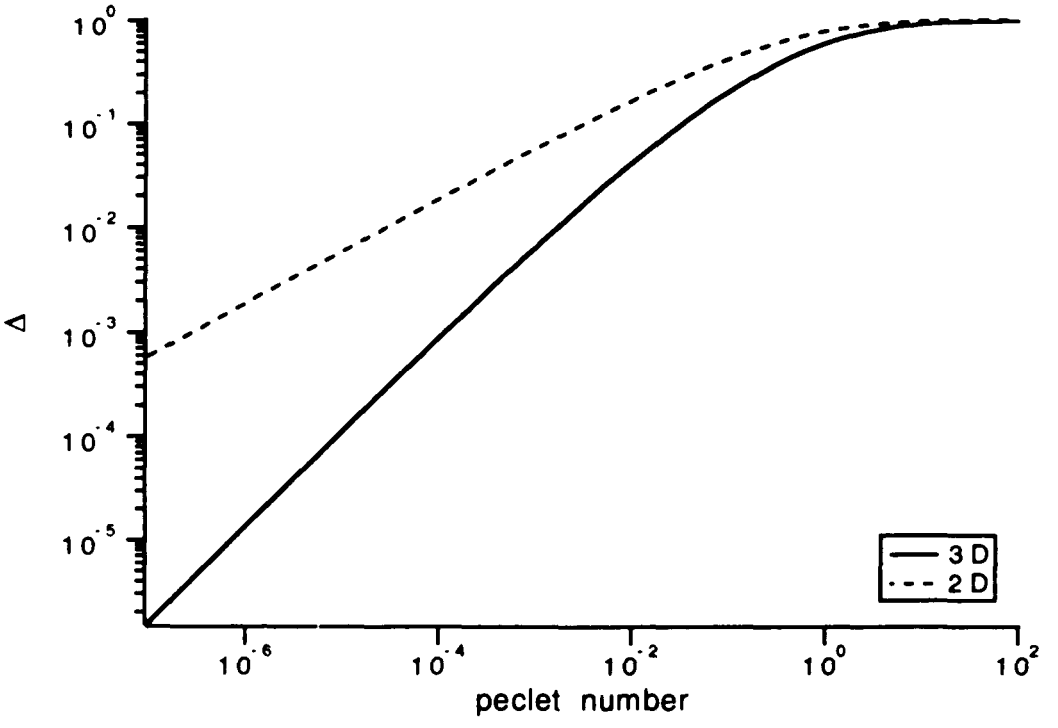

Fig. 4: Relationship between the peclet number and the dimensionless undercooling Δ in both 2 and 3 dimensions.

dimensional value of $2/\rho$ at the tip. The interface was still taken as isothermal, but at the tip temperature $T_i=T_m(1-2\gamma/L\rho)$ in accord with Eq. (2.3). The relationship between the dimensionless undercooling Δ, the tip radius ρ and the steady-state velocity v in 3 D then becomes

$$\Delta = \frac{2d_o}{\rho} + p\exp(p)E_1(p) \tag{2.27}$$

Temkin chose to preserve the Gibbs-Thompson term (2.3) but imposed the continuity condition (2.2) only at the tip of the parabola [T1]. He found

$$\Delta = \left(1 + b\frac{2Dd_o}{\rho^2 v}\right)p\exp(p)E_1(p) \tag{2.28}$$

where b is a weekly p-dependent function. In the limit of small peclet number we can replace b by a constant [L1]

$$b \cong \begin{cases} 1.819 & D'=0, \beta=0; \\ 2.949 & D'=1, \beta=1. \end{cases} \tag{2.29}$$

Note that both equations (2.27) and (2.28) show an important scaling behavior. We can introduce a dimensionless velocity, the ratio of the capillary length and the diffusion length, $V=d_0/l_D$ and a dimensionless tip radius $\bar{\rho} = \rho / d_o$. Then the peclet number is just $p=V\bar{\rho}$ and we can generate a plot of the two selection criteria (2.27) and (2.28) independent of material parameters. The two resulting $(\bar{\rho},V)$-relations for a fixed undercooling Δ together with the Ivantsov result (2.23) are plotted in Fig.5.

These maximum growth speed approaches failed to agree with careful experimental tests by Glicksman in SCN [G2]. The selected speed found in his experiments is also shown in Fig.5 and is obviously far from the maxima in growth speed predicted by Sekerka or Temkin.

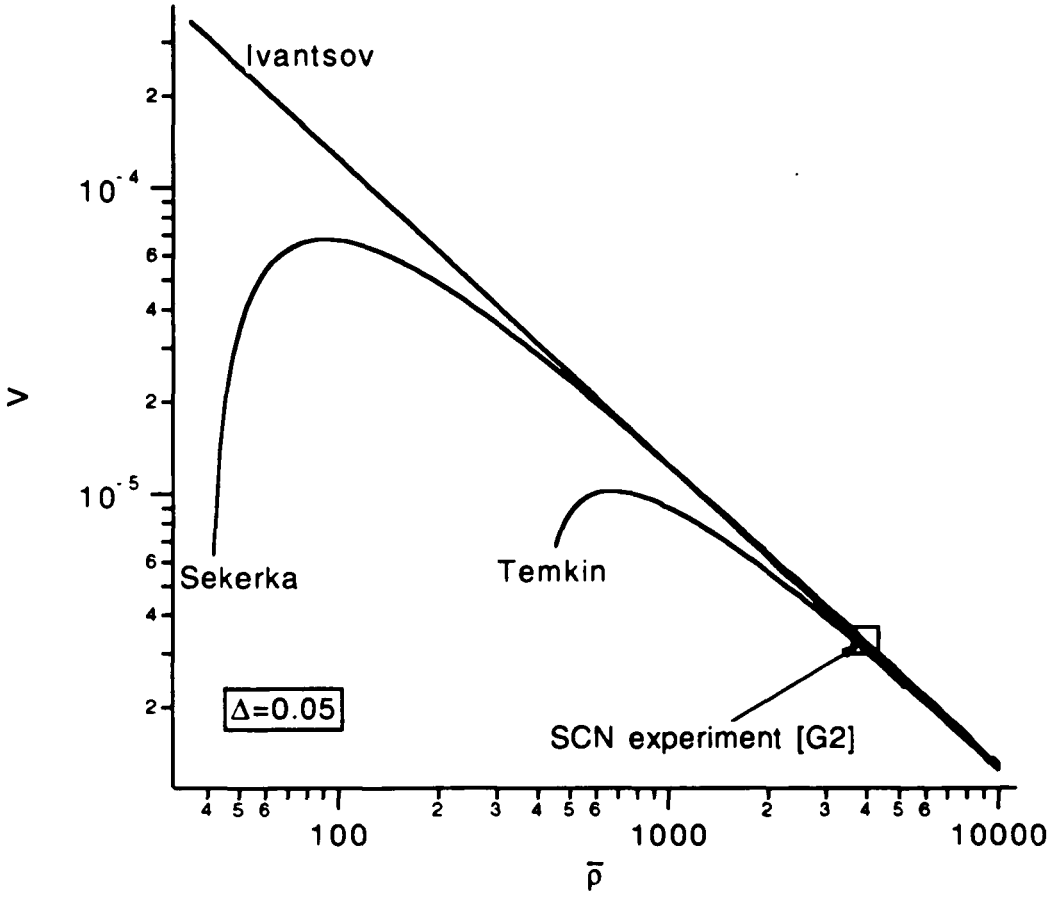

Fig. 5: Relationship between the tip radius $\bar{\rho} = \rho / d_o$ and the growth velocity $V = d_o / l_D$ for two common modifications of the Ivantsov solution by Temkin and Sekerka. The small square represents experimental results obtained by Glicksman in SCN [G2].

2.3.2 Marginal Stability

Langer and Müller-Krumbhaar took a different approach to the selection problem. They performed a linear stability analysis of the Ivantsov solution [L1-L6]. The analysis is in spirit similar to the Mullins-Sekerka analysis in section 2.2; mathematically, however, it is much more tedious. The main result was that the Ivantsov solution was argued to be unstable against a tip-splitting instability below a certain critical value of a newly introduced stability parameter

$$\sigma = \frac{2d_o D}{\rho^2 v} = \left(\bar{\rho}^2 V\right)^{-1}. \tag{2.30}$$

where $\bar{\rho}$ and V are the dimensionless tip radius and growth velocity introduced in the previous section. Above the critical value of σ the dendritic tip would remain stable. We should bear in mind that this stability criterion is different from the simple Mullins-Sekerka case. It is only the stability of the tip region that is guaranteed by (2.30). The sides of the dendrite are always unstable. This picture naturally explained the existence of sidebranches as experimentally observed. They are the result of a secondary instability. In the tip region the presence of surface tension can suppress this instability unless the radius of curvature becomes too large which leads to tip-splitting. This analysis does not automatically provide a selection criterion since all states above the stability threshold are stable and are in fact growing faster than the dendrite just on the verge of stability (see the Ivantsov curve in Fig.5). Langer and Müller-Krumbhaar proposed that the selected operating point for the real dendrite was the marginally stable one right at the stability threshold. They proposed that

nonlinear effects would provide a mechanism to drive the dendrite to this state.

To estimate the value of σ that produced marginal stability they approximated the parabolic tip by a sphere with the same radius of curvature and performed a Mullins-Sekerka analysis for this sphere. Their result was [L1]

$$\frac{1}{\sigma^*} = \frac{1}{2} j(j+2)(1+\mu+j^{-1}) \tag{2.31}$$

where σ^* is the value of σ at marginal stability and j is the index of the spherical harmonic $Y_{j,m}(\theta,\phi)$ used as a base function in the linear stability analysis. We are still left with the arbitrary choice of the index j. Experiments by Glicksman in SCN (μ~1) [H2] produced a value of σ^* = 0.0195 very close to σ^* = 0.0192 from eqn. (2.31) for j=6. Note that the value of σ^* depends on the material properties only through the "asymmetry parameter" μ which is the ratio of the diffusion constants in the two phases.

2.4. Microscopic Solvability Theory

The Langer and Müller-Krumbhaar stability analysis didn't provide a well-founded criterion to explain why dendrites would select the marginally stable state as their operating point. They suggested that such a criterion would emerge only from a nonlinear analysis of the full set of equations [L7]. The complex structure of this nonlinear moving boundary problem inspired the search for simplified models which still retained the essential features of the real problem at hand.

2.4.1 Local Models and the Saffman-Taylor problem

Two candidates emerged: the geometric model suggested by Brower et al. [B6-B8] and the boundary layer model by Ben-Jacobs et al [B3-B5]. In both models the motion of the interface is uncoupled from the non-local interaction with the diffusion field. The geometric model relates the normal velocity of an interface segment to its curvature κ. The boundary layer model replaces the diffusion field by a thermal boundary layer which is thin compared to the local radius of curvature of the interface, and produces a set of five equations describing the evolution of the interface. It goes over into the real dendritic problem in the limit of large undercoolings $\Delta \approx 1$ when the diffusion length indeed reaches that limit [B3]. Details of both models can be found in the references but are not essential to the following discussion.

In the absence of surface tension both models display a continuum of needle-crystal solutions similar to the Ivantsov solution. In addition the planar geometry is linearly unstable. Including surface tension destroys the

needle-like solutions altogether [B6,B4]. This result is contrary to previous approaches which consider surface tension as a regular perturbation of the Ivantsov solution. Only when crystalline anisotropy was included in the model equations, either through an anisotropic kinetic term [B4] or an anisotropic surface tension term [K1], did a discrete set of needle-solutions emerge.

In the late 1950's Saffman and Taylor published a theoretical paper dealing with the displacement of a viscous by a non-viscous fluid in a Hele-Shaw cell [S4] neglecting surface tension effects. The control parameter equivalent to the undercooling of the dendritic problem is the average velocity V of the intruding liquid. For any given velocity V they derived finger-like solutions which occupied an arbitrary fraction λ of the cell width. Only the ratio of propagation speed v of the finger to its width λ was fixed by the control parameter V (see Fig.6). In their experiments, however, they observed fingers of fixed width λ for given displacement velocity V, approaching the value of $\lambda=1/2$ for large V. McLean and Saffman [M3] and Vanden-Broeck [V1] rewrote the mathematical problem in the form of an integro-differential equation including surface tension effects. Their numerical solutions produced only a discrete set of ratios v/λ at a given driving force.

These results posed two challenges for the solidification problem. Could a similar breakdown of the continuum solutions occur in dendritic growth and how could one understand this? And secondly, if there was a discrete set of solutions which one would be selected?

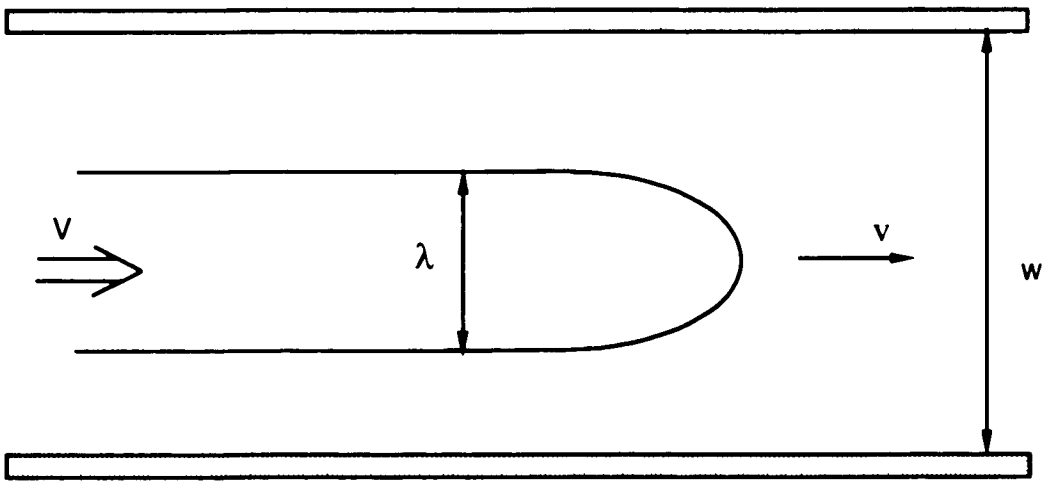

Fig. 6: Saffman-Taylor geometry. A channel of width w contains the high and low viscosity fluid. The low viscosity fluid intrudes the high viscosity fluid with an average velocity V. A finger-shaped interface of width λ develops between the two fluids and propagates with velocity v.

2.4.2 The Integro-Differential Equation of Steady-State Dendritic Growth

All investigations of the above questions start by rewriting the set of equations (2.1) -(2.4) in the form of an integro-differential equation. We will therefore derive this central equation for the symmetric model (equal thermal conductivities in the solid and liquid phase) in two dimensions by the following steps:

(1) Introduce the Green's function for the diffusion equation in free space and incorporate boundary condition (2.4).

(2) Build in the effect of the moving interface by matching the thermal fields in the solid and in the liquid at the boundary, requiring continuity of heat flux (Eq. (2.2)).

(3) Specialize to the case of a steady-state shape propagating into the melt and find the temperature distribution along the interface.

Finally we include the effect of the surface tension on the local temperature along the interface via boundary condition (2.3).

2.4.2.1. The Green's Function of the Diffusion Equation in Free Space

The differential equation for the Greens function of the diffusion equation

$$(D\nabla^2 - \partial_t)G(\vec{r},t) = -\delta(\vec{r})\delta(t) \tag{2.32}$$

is satisfied by

$$G(\vec{r},t) = \frac{1}{4\pi Dt}\exp(-\frac{r^2}{4Dt}) \tag{2.33}$$

We can verify this by noting that for t>0

$$\partial_t G(\vec{r},t) = \frac{D}{4\pi Dt}\left[-\frac{d}{2Dt} + \left(\frac{r}{2Dt}\right)^2\right]\exp\left(-\frac{r^2}{4Dt}\right) \qquad (2.34)$$

and $$\partial_x^2 G(\vec{r},t) = \frac{1}{4\pi Dt}\partial_x\left[-\frac{2x}{4Dt}\exp\left(-\frac{r^2}{4Dt}\right)\right]$$

$$= \frac{1}{4\pi Dt}\left[-\frac{1}{2Dt} + \left(\frac{x}{2Dt}\right)^2\right]\exp\left(-\frac{r^2}{4Dt}\right) \qquad (2.35)$$

therefore $$\Delta G(\vec{r},t) = \frac{1}{4\pi Dt}\left[-\frac{1}{Dt} + \left(\frac{r}{2Dt}\right)^2\right]\exp\left(-\frac{r^2}{4Dt}\right) \qquad (2.36)$$

and G(r,t) satisfies (2.32) for all times t>0. We can see that G(r,t) has the proper singular behavior, because

$$\int G(\vec{r},t)d^2x = \frac{1}{4\pi Dt}\left[\int_{-\infty}^{\infty}\exp\left(-\frac{x^2}{4Dt}\right)dx\right]^2$$

$$= \frac{1}{4\pi Dt}\left[\sqrt{4\pi Dt}\right]^2 = 1 \qquad (2.37)$$

is constant and equal to one, even as t→0. G(r,t) therefore represents an elementary solution to the diffusion equation in free space.

2.4.2.2 Boundary Condition at Infinity and at the Interface

We can use G(r,t) to express the temperature distribution throughout the solid and the liquid in closed form:

$$T(\vec{r},t) = T_\infty + \int dS\int_{-\infty}^{t} dt' G(\vec{r}-\vec{r}',t-t')Lv_n(\vec{r}',t')/c_p \qquad (2.38)$$

Since $G(r,t) \to 0$ for $|r-r'| \to \infty$, there is no contribution of the integral to the temperature at infinity. The only term surviving at infinity is the constant T_∞, which automatically satisfies the boundary condition (2.4). Next we go across the interface and show that Eq. (2.38) also satisfies boundary condition (2.2):

$$
\begin{aligned}
-Dc_p\left[\hat{n}\cdot\nabla T\right]_{liq-sol} &= -Dc_p \int_{box}(\hat{n}\cdot\nabla T)da \\
&= -Dc_p \int_{box}(\nabla^2 T)d^3r \\
&= -Dc_p \int_{box} d^3r\,\nabla^2\left[\int dS'\int_{-\infty}^{t} dt' G(\vec{r}-\vec{r}',t-t')Lv_n(\vec{r}',t)/c_p\right] \\
&= -DL\int_{box} d^3r\int dS'\int_{-\infty}^{t} dt'\nabla^2 G(\vec{r}-\vec{r}',t-t')v_n(\vec{r}',t') \\
&= -L\int_{box} d^3r\int dS'\int_{-\infty}^{t} dt'\left[-\delta(\vec{r}-\vec{r}',t-t')+\partial_t G\right]v_n(\vec{r}',t') \\
&= Lv_n(\vec{r},t) - L\int dS'\int_{-\infty}^{t} dt' v_n(\vec{r}',t')\partial_{t'}\left[\int_{box} d^3r G(\vec{r}-\vec{r}',t-t')\right] \\
&= Lv_n(\vec{r},t) \qquad (2.39)
\end{aligned}
$$

The subscript "box" on the integral in the first line refers to a small Gaussian pill box across the interface. In line two above we used the first identity of Green with one of the functions constant and equal to one. The last step follows from Eq. (2.37). The time derivative therefore vanishes, and with it the second term on the right side of the second to last line.

2.4.2.3. Steady-State Equation

We now focus on the case of steady-state growth : A solid with constant shape propagates into the melt ahead of it. Its shape is given by:

$$\vec{\eta}(\vec{r},t) = (x, \zeta(x) + vt) \tag{2.40}$$

where $\zeta(x)$ describes the constant steady-state shape and v is its growth velocity. We change variables from arc length s to x (see Fig. 7):

$$v_n ds' = v(\hat{y}\cdot\hat{n})ds' = v\cos(\theta)ds' = v\,dx' \tag{2.41}$$

The integral on the r.h.s. of Eq. (2.38) becomes:

$$I \equiv \frac{Lv_n}{c_p}\int ds' \int_{-\infty}^{t} \frac{dt'}{4\pi D(t-t')} \exp\left\{-\frac{(\vec{\eta}-\vec{\eta}')^2}{4D(t-t')}\right\}$$

$$= \frac{Lv}{4\pi D c_p}\int_{-\infty}^{\infty} dx' \int_{-\infty}^{t} \frac{dt'}{t-t'} \exp\left\{-\frac{(x-x')^2 + (\zeta-\zeta'-v(t-t'))^2}{4D(t-t')}\right\}$$

$$= \frac{Lv}{4\pi D c_p}\int_{-\infty}^{\infty} dx' \exp\left\{\frac{v}{2D}(\zeta-\zeta')\right\} \times$$

$$\int_{-\infty}^{t} \frac{dt'}{t-t'} \exp\left\{-\frac{(x-x')^2 + (\zeta-\zeta')^2}{4D(t-t')} - \frac{v^2}{4D}(t-t')\right\} \tag{2.42}$$

We substitute:

$$t - t' = \tau \Rightarrow dt' = -d\tau, \int_{-\infty}^{t} dt' \rightarrow \int_{-\infty}^{0} -d\tau = \int_{0}^{\infty} d\tau \tag{2.43}$$

and perform the integration over time

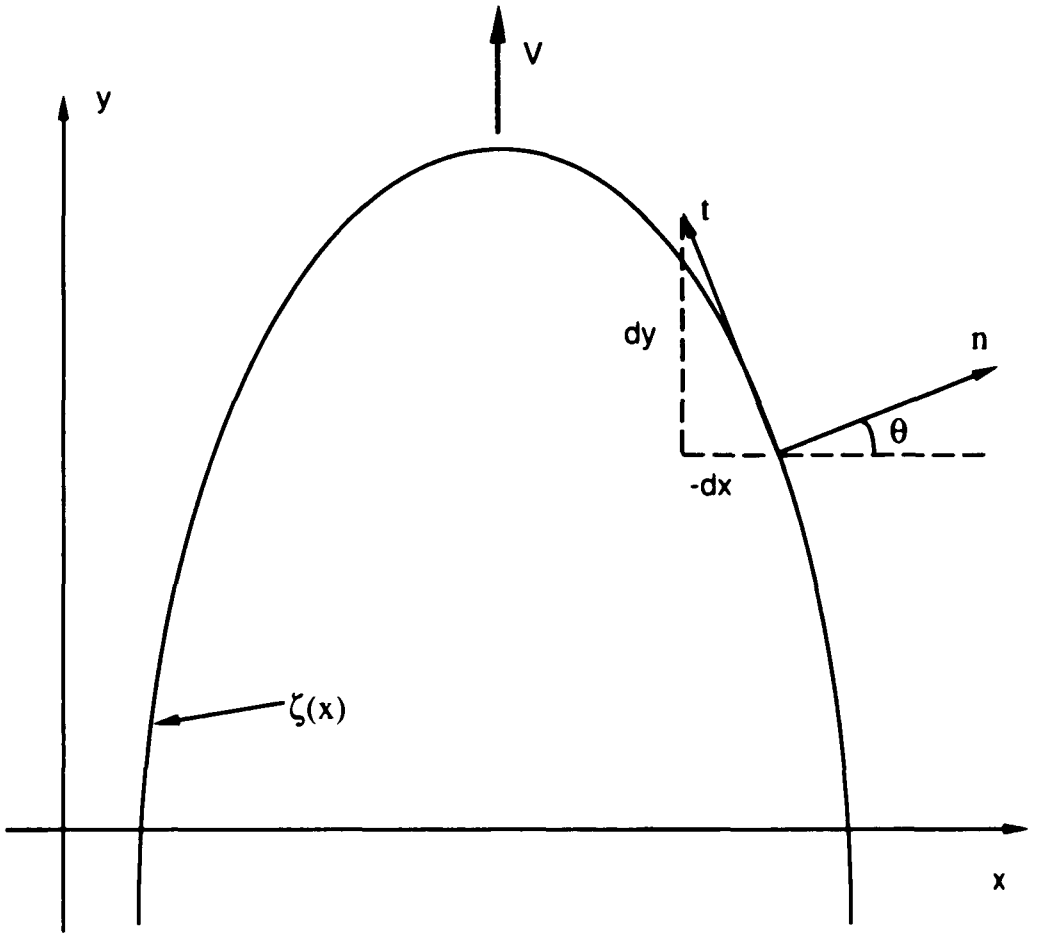

Fig. 7: Steady-state interface $\zeta(x)$ propagating with speed V. The normal vector n together with the normal angle θ is shown for some point along the interface.

$$J \equiv \int_{-\infty}^{t} \frac{dt'}{t-t'} \exp\left\{ -\frac{(x-x')^2 + (\zeta-\zeta')^2}{4D(t-t')} - \frac{v^2}{4D}(t-t') \right\}$$

$$= \int_0^{\infty} \frac{d\tau}{\tau} \exp\left\{ -\frac{(x-x')^2 - (\zeta-\zeta')^2}{4D\tau} - \frac{v^2}{4D}\tau \right\}$$

$$= \int_0^{\infty} \frac{d\tau}{\tau} \exp\left\{ -\frac{v}{2D}\sqrt{(x-x')^2 + (\zeta-\zeta')^2} \times \right.$$

$$\left. \left[\frac{1}{2}\left(\frac{\sqrt{(x-x')^2 + (\zeta-\zeta')^2}}{v\tau} + \frac{v\tau}{\sqrt{(x-x')^2 + (\zeta-\zeta')^2}} \right) \right] \right. \qquad (2.44)$$

Now we set

$$w = \frac{v\tau}{\sqrt{(x-x')^2 + (\zeta-\zeta')^2}} \Rightarrow dw = \frac{v}{\sqrt{(x-x')^2 + (\zeta-\zeta')^2}} d\tau \qquad (2.45)$$

and put this back into the integral J

$$J = \int_0^{\infty} \frac{dw}{w} \exp\left\{ -\frac{v}{2}\sqrt{(x-x')^2 + (\zeta-\zeta')^2} * \frac{1}{2}\left(w + \frac{1}{w}\right) \right\} \qquad (2.46)$$

Finally we substitute:

$$u = \ln(w) \Rightarrow du = \frac{dw}{w}, \int_0^{\infty} \frac{dw}{w} \rightarrow \int_{\ln(0)}^{\ln(\infty)} du = \int_{-\infty}^{\infty} du \qquad (2.47)$$

to obtain

$$J = \int_{-\infty}^{\infty} \exp\left\{ -\frac{v}{2D}\sqrt{(x-x')^2 + (\zeta-\zeta')^2} * \frac{1}{2}(\exp(u) - \exp(-u)) \right\} du$$

$$= \int_{-\infty}^{\infty} \exp\left\{ -\frac{v}{2D}\sqrt{(x-x')^2 + (\zeta-\zeta')^2} * \cosh(u) \right\} du$$

$$= 2\int_0^{\infty} \exp\left\{ -\frac{v}{2D}\sqrt{(x-x')^2 + (\zeta-\zeta')^2} * \cosh(u) \right\} du$$

$$= 2K_0\left(\frac{v}{2D}\sqrt{(x-x')^2+(\zeta-\zeta')^2}\right) \tag{2.48}$$

In the second to last line above we used the symmetry of the integrand to restrict the range of integration. The last line states that the above integral is equal to the zeroth-order, modified Bessel function defined as [A1]

$$K_0(z) = \int_0^\infty \exp\{-z*\cosh(u)\}du \tag{2.49}$$

(2.48) yields for the integral I in Eq. (2.42) :

$$I = \frac{Lv}{2\pi Dc_p}\int_{-\infty}^{\infty} dx' \exp\left\{\frac{v}{2D}(\zeta-\zeta')\right\} * K_0\left\{\frac{v}{2D}\sqrt{(x-x')^2+(\zeta-\zeta')^2}\right\} \tag{2.50}$$

This completes the evaluation of the r.h.s. of (2.38) along the interface. On the l.h.s. we substitute the Gibbs-Thompson relation (2.3) without the kinetic term. The final result is

$$\Delta - d_o\kappa = \frac{v}{2\pi D}\int_{-\infty}^{\infty} dx' \exp\left\{\frac{\zeta-\zeta'}{l_D}\right\} K_0\left\{\frac{\sqrt{(x-x')^2+(\zeta-\zeta')^2}}{l_D}\right\} \tag{2.51}$$

where Δ is the dimensionless undercooling, d_0 the capillary length, and l_D the diffusion length all of which have been previously defined (see section 2.2). Cast in this form one central feature of the problem becomes evident: the surface tension term d_0 on the l.h.s. of (2.51) contains the highest derivative in the equation. Surface tension therefore acts as a singular perturbation. An important consequence of this last result is that previous attempts to introduce surface tension as a small perturbation on the Ivantsov solution were mathematically inappropriate.

2.4.3 Analysis of the Steady State Equation

Numerical analysis of the integro-differential equation (2.51) by Kessler, Koplik and Levine [K5,K6] as well as by Meiron [M4] provided the first complete solutions to the full non-linear problem. Their basic approach followed ideas by Vanden Broeck [V1] developed in the study of the Saffman-Taylor problem. Taking advantage of the reflection-symmetry of the parabola along the axis of propagation they derived equations for the interface on one half of the parabola. The main idea is to leave the slope at the tip of the parabola as a free parameter to be determined numerically. Physically acceptable solutions must have that slope equal to zero. i.e., a cusp at the tip is forbidden.

For fixed capillary length d_0=const., equivalent to an isotropic surface tension, the continuum of Ivantsov solutions was destroyed. For any non-vanishingly small capillary length, the cusp at the tip was not zero (see Fig.8). Only when allowing for anisotropy in the surface tension did a discrete set of solutions reemerge. The expression *microscopic solvability* was coined for this behavior: the presence of a microscopic length scale (here d_0) determined the existence of a macroscopic solution to the problem.

Caroli et.al. [C5] studied the one-sided as well as the symmetric model analytically in the limit of large undercoolings and for the case of isotropic surface tension. They derived an expression for the cusp magnitude S at the tip as a function of a solvability parameter σ

$$S \propto \exp\left(-\frac{a}{\sqrt{\sigma}}\right) \qquad (2.52)$$

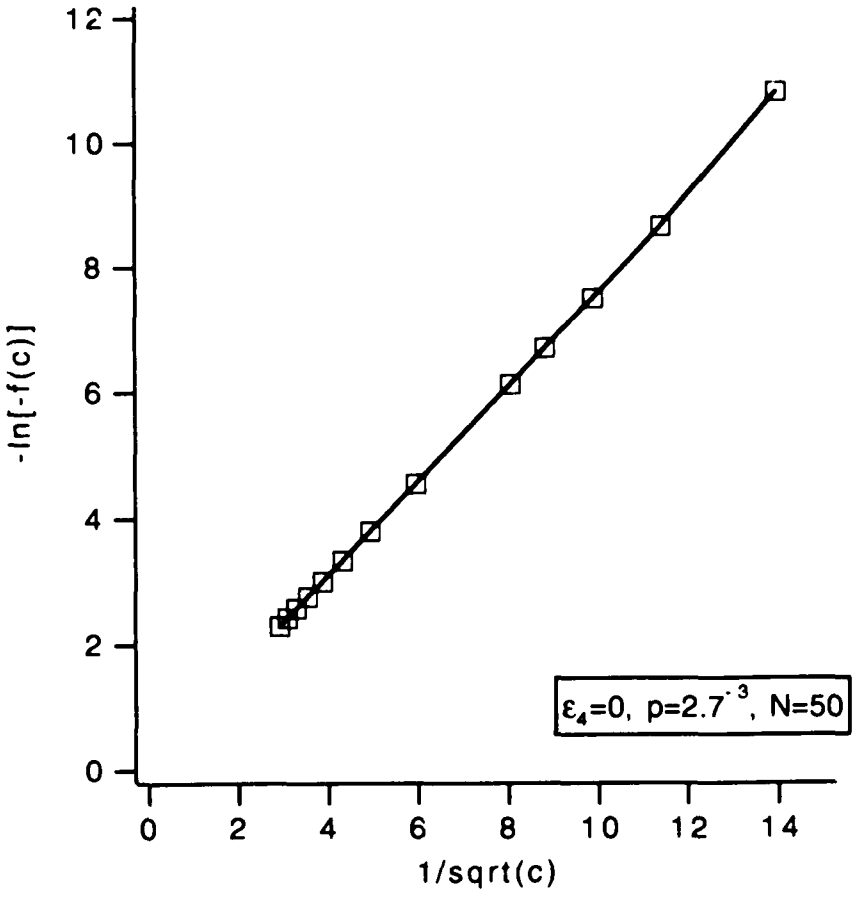

Fig. 8: Plot of the logarithm of the cusp magnitude at the tip of the steady-state solution versus the dimensionless velocity. The results are obtained from numerical calculations in two dimensions for isotropic surface tension (the program to generate these results was generously provided to us by Herbert Levine)

where $a \approx 0.4355$ is a constant and σ is the same parameter introduced by the marginal stability hypothesis in Eq.(2.30). This result was consistent with the numerical results for the symmetric model found by Kessler (see Fig.8). Note the essential singularity of S for $\sigma \rightarrow 0$. Eq (2.52) cannot be expanded in a power series for the limit of vanishing surface tension. This is the mathematical reason why perturbative expansions around zero-surface tension solutions must fail.

Pelce and Pomeau [P3] analyzed the symmetric model in two- and three dimensions for small undercoolings. They derived a scaling law for the dendritic velocity as a function of undercooling which in two dimensions takes the form

$$V = (16/\pi^2 C)\Delta^4 \qquad (2.53)$$

where V is the dimensionless velocity , Δ the dimensionless undercooling and C is an undetermined eigenvalue closely related to σ [B9]. The same type of scaling was derived from marginal stability except for the presence of the undetermined 'nonlinear eigenvalue' C. Ben Amar and Pomeau [B9] found no solutions to this eigenvalue equation for isotropic γ. Anisotropy in the surface tension, however, restores a denumerably infinite set of eigenvalues C.

Ben Amar and Pomeau [B9] and Barbieri et. al. [B10] both assumed an explicit form for the anisotropy of the capillary length in two dimensions

$$d_0(\theta) = d_0 [\, 1 - \alpha \cos(4\theta)] \qquad (2.54)$$

where d_0 is the average capillary length and α is a measure of the surface tension anisotropy (see Eq. (3.28)). In the limit of vanishing peclet number they found an analytical expression describing the discrete set of allowed

solutions. Only the fastest growing of this set appears to be linearly stable, however (this result was also obtained by Kessler and Levine [K7]). In addition they determined how the parameter σ of this stable state varies with the anisotropy strength α for small α

$$\sigma^* \propto \alpha^{7/4} \tag{2.55}$$

where the star indicates the value of σ for the linearly stable state, and the proportionality constant is a number of the order of one.

Caroli et. al. [C7] showed that (2.55) holds for all peclet numbers with $p\alpha^{1/2} \ll 1$ in two dimensions as long as the anisotropy parameter α remains small (≤ 0.01). In particular their result implies that, for small anisotropies, the selection parameter σ^* of the selected state is independent of the undercooling Δ.

Bensimon et al. [B11] and Brener et al. [B12,B13] studied the stability of the allowed set of discrete solutions to (2.51) in the presence of anisotropy. They found that the n-th selected state possesses n unstable tip-splitting modes. Therefore the state with the lowest eigenvalue (highest growth speed), labeled by n=0, is in fact stable.

Barbieri and Langer [B15] derived a selection criterion by linearizing the equations in the deviations of the actual dendrite shape from the Ivantsov solution. They estimated their selection criterion to be valid for values of α all the way up to 0.6. Their result is shown in Fig.9. As we can see σ^* is strongly dependent on the anisotropy parameter α and displays only a weak dependence on the peclet number p (the small α scaling $\sigma^* \propto \alpha^{7/4}$ doesn't hold for the range of α plotted in Fig.9). They also related the values of the selection parameter σ^* derived from the symmetric model to the values of the one-sided model

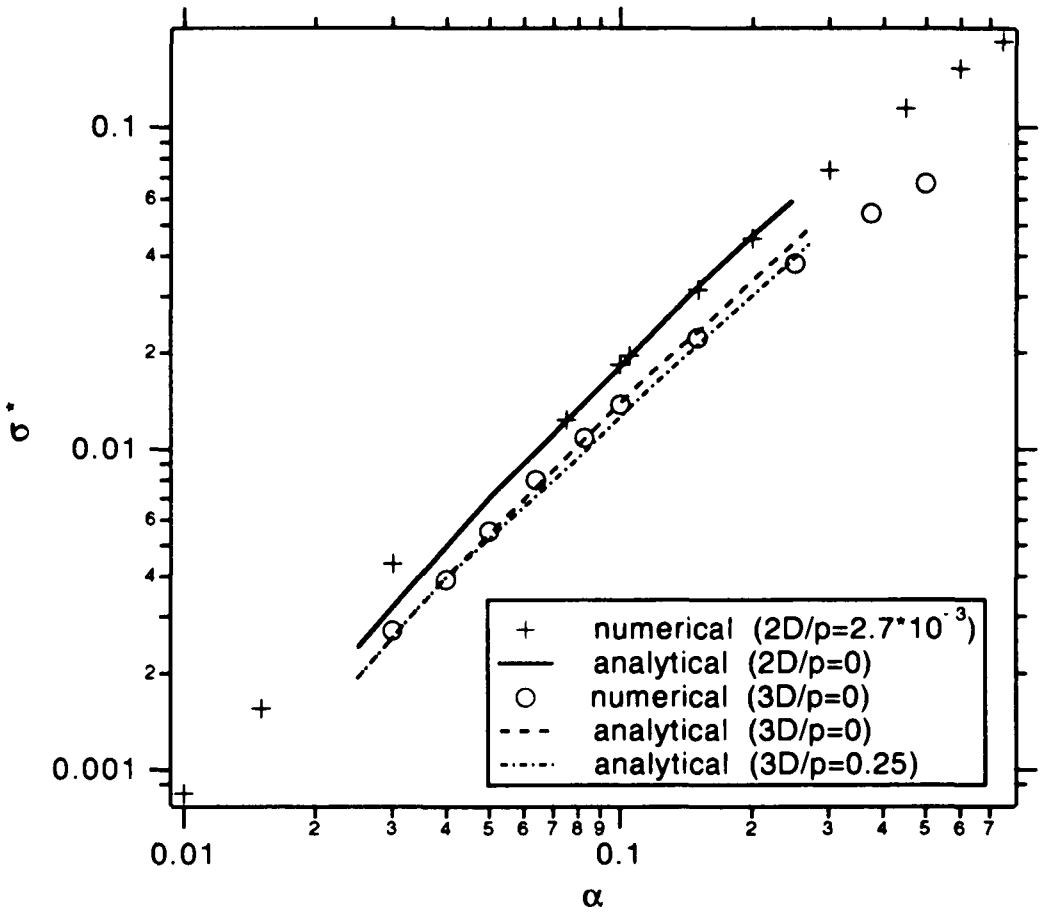

Fig. 9: Selected values of the stability parameter σ^* vs surface tension anisotropy α predicted by microscopic solvability theory. (For fourfold anisotropy, $\alpha = 15\varepsilon_4$; for six-fold anisotropy, $\alpha = 35\varepsilon_6$). The solid lines are the analytic results of Barbieri and Langer [B15] for the symmetric model in two dimensions with p=0 (——), and in three dimensions with p=0 (- - -) or p=0.25 (- · - · - ·). The symbols (+) are the results of a numerical calculation based on the method of Kessler and Levine [K2] for the two-dimensional symmetric model with p=0.0027 and the symbols (O) are the result of a numerical calculation by M. Ben Amar [B22] for 3-d axisymmetric growth.

$$\sigma^*(\mu) = [2/(1+\mu)]\ \sigma^*(\mu=1) \qquad (2.56)$$

where $\mu=D_S c_S/D_l c_l$ in the case of thermal diffusion ($\mu=D_S/D_l$ for chemical diffusion) measures the asymmetry of the solid and the liquid phase and has the value $\mu=1$ in the symmetric model and $\mu=0$ in the one-sided model.

2.4.4 Summary of Results for Selection in Two Dimensions

The main result of these theoretical investigations is the vanishing of the Ivantsov continuum in the absence of anisotropy in the surface tension. When including anisotropy a discrete set of solutions emerges with only the fastest growing one being stable against tip-splitting. The selection of the dendrite problem is thus controlled by the value of the selection parameter $\sigma^*(\alpha,p)$ which is very sensitive to the value of the anisotropy parameter α but only weakly dependent on the peclet number p.

Microscopic solvability provides a completely different approach to the selection problem than marginal stability or the maximum growth speed criterion. Nevertheless, when dealing with the singular character of the surface tension properly, microscopic solvability shows that the selected state is indeed the fastest growing and the only stable state of the system. The selection parameter σ^* is the same combination of constants as in marginal stability. Furthermore, the scaling law dependences of the selected velocity and tip radius on the undercooling have the same functional form as the ones derived from marginal stability, if one neglects the weak p-dependence of σ^* [P3,L1]. This makes the anisotropy dependence of σ^* the most significant test of microscopic solvability predictions when comparing with experimental results.

2.4.5 Extensions of the Theory

Pelce and Pomeau [P3], Caroli et. al [C6,C7], Kessler et al. [K6] and Barbieri et al. [B10] all find the same type of selection mechanism in three dimensional growth. Specifically, there is no solution to the selection problem with isotropic surface tension. A major technical problem is to account for anisotropy in three dimensions which has not yet been fully accomplished. The most common approximation studied is axisymmetric surface tension:varying only in the plane of the polar angle as given in Eq. (2.54). Including this axisymmetric anisotropy term again leads to the appearance of a discrete set of Ivantsov-like solutions with only the fastest one being linearly stable. The selected state is determined by the value of the parameter σ^*. Barbieri and Langer [B 15] used the same approximation as in their two-dimensional analysis to derive $\sigma^*(\alpha,p)$ over a wide range of α-values. Ben Amar obtained σ^* from numerical calculations on the 3-dimensional extension to Eq. (2.51) [B22]. Both of these results are included in Fig.9 .The similarity between the two- and three-dimensional results is striking. Kessler and Levine [K8] went beyond the axisymmetric case by including azimuthal dependence of the surface tension as a perturbation. Their result suggest that the velocity selection at the tip is dominated by the axisymmetric terms of the surface tension anisotropy.

Dendritic growth experiments are often performed in capillaries. Kessler et al. [K9] and Brener et al. [B14] studied the theoretical problem of selection of two-dimensional growth in a channel of finite width Λ. This geometry allows two branches of solutions, one Saffman-Taylor like [K9,B14], the other dendritic [B9]. The latter is labeled dendritic since its

$v(\Delta)$ dependence approaches the one for free dendrites in the limit $\Lambda \rightarrow \infty$. Solutions exist only starting from a minimum undercooling Δ_m

$$\Delta_m \propto (\Lambda\alpha^{7/4})^{-1/4} \qquad \text{for } \Lambda\alpha^{7/4} \gg 1 \qquad (2.57)$$

Brener et al. [B12,B13] showed that there is sharp selection with respect to the growth direction of dendrites as well. Dendrites will only grow in the direction of minimal capillary length of the underlying seed crystal. For capillary length as given in Eq. (2.54) those directions are $\theta=0,\pi/2,\pi,3\pi/2$. These are the angles of maximum surface tension, as we will explain in chapter 3.1.

Already in the boundary layer model Ben-Jacob et. al. [B6] observed that an anisotropic kinetic term would lead to a selection mechanism very similar to the one for anisotropic surface tension. Lemieux et al. [L9] extended the analysis to the full problem. Neglecting surface tension and only including an isotropic kinetic term in the equations they found a continuous family of solutions without cusps, but only for $\beta v/p \ll 1$, where β is the kinetic coefficient in (2.3), v is the dendritic growth speed and p the peclet number. The presence of a singular perturbation term therefore does not necessarily destroy the continuum of solutions. Numerically only the regime $\beta v/p \geq 1$ is accessible to them and they find no solutions at any value of v. When including both terms in (2.3) with anisotropy of the kinetic term in the form

$$\beta(\theta)=\beta_0 [\, 1-\beta_4 \cos(4\theta)] \qquad (2.58)$$

and using anisotropic surface tension as in Eq. (2.54) the selected velocity depends on both α and β_4 (for p=1). Brener et al. [B14] derived a scaling law for the selected dendritic velocity when only subjected to anisotropy of the kinetic term

$$v \propto \beta_4^{\,5/4} \qquad (2.59)$$

which holds for sufficiently small β_4 and $p\beta_4 \ll 1$.

All the theories discussed here describe smooth needle crystals neglecting the presence of sidebranches. Saito et al. [S5] developed a numerical algorithm for two-dimensional growth in the one-sided model that allowed sidebranches to develop (driven by numerical noise). Their analysis used the material parameters of SCN. They conclude that the selection mechanism is not altered by the sidebranching process. Their results are, however, based on numerical evidence at only two values of the peclet number (p=0.25 and 0.5).

3. Anisotropic Surface Tension and Equilibrium Crystal Shape

3.1. Gibbs-Thompson Relation for Isotropic Surface Tension

The Gibbs-Thompson Relation determines the change in melting temperature of a crystal due to surface tension. The following derivation closely follows Woodruff [W1].

For a solid to be in equilibrium with its melt at constant temperature and pressure the Gibbs free energies of the two phases have to be equal. Gibbs phase rule shows that this can only happen at a single temperature. If we neglect surface tension, the free energies of the two phases are determined by their bulk values G_s and G_l and the coexistence temperature is just the melting point T_m. For values $T>T_m$ we have $G_s>G_l$ and the crystal melts while for $T<T_m$ the solid represents the only stable phase (see Fig.10). At the melting temperature T_m the discontinuity in the slopes of G_s and G_l is related to the entropy change of the phase transformation

$$\left(\frac{\partial G_s}{\partial T}\right)_p - \left(\frac{\partial G_l}{\partial T}\right)_p = S_l - S_s = \frac{\Delta Q}{T_m} = \frac{L}{T_m} \qquad (3.1)$$

Now consider an undercooled volume of melt at temperature $T<T_m$. We introduce a small crystal of volume V into the system, this time taking surface tension effects into account (see Fig. 11). The change in the Gibbs free energy ΔG of the whole system due to the presence of the crystal consists of two contributions:

$$\Delta G_V = (Gs-Gl)\ V = VL(T-T_m)/T_m \qquad (3.2a)$$

and

$$\Delta G_A = \gamma A \qquad (3.2b)$$

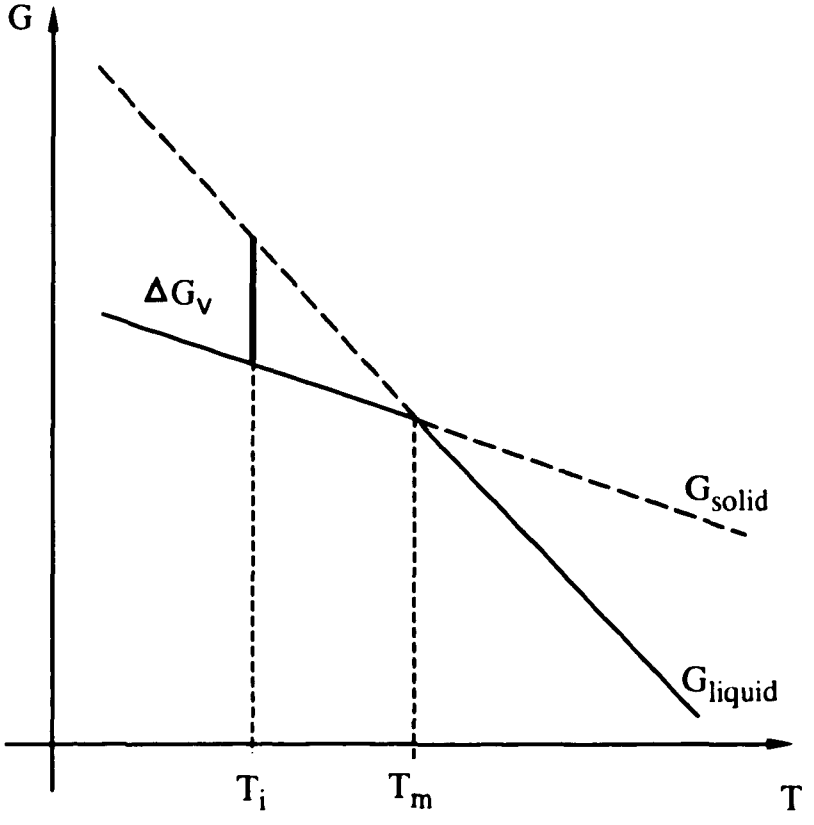

Fig. 10: Gibbs free energy of the crystal (G_{solid}) and liquid (G_{liquid}) bulk phases as function of temperature. For temperatures close to the melting point Tm we can use a linear approximation to G_{solid} and G_{liquid}. ΔG_v is the difference in bulk free energy between the solid and liquid phase at the temperature $T_i < T_m$.

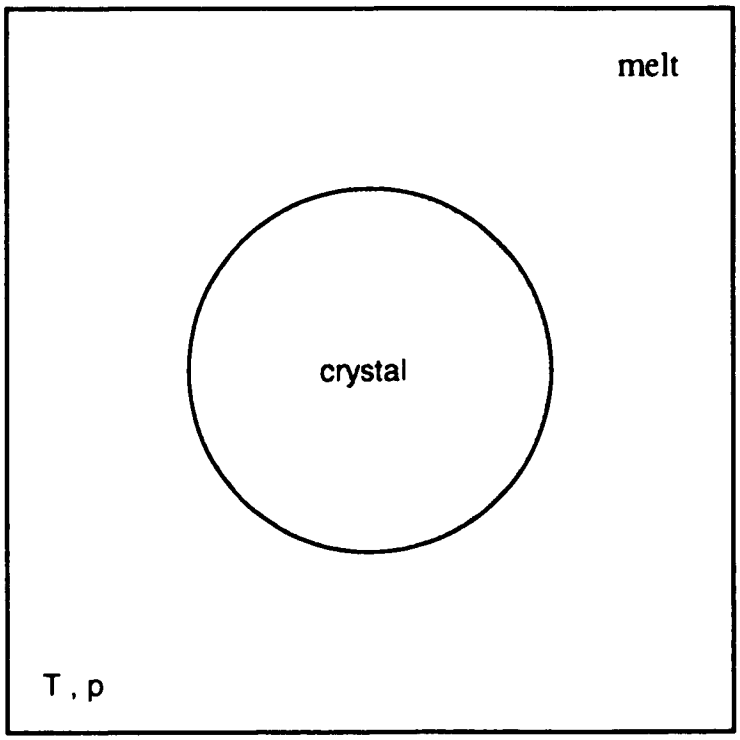

Fig. 11: Crystal surrounded by its melt at fixed temperature T and fixed external pressure p.

The first term accounts for the decrease in bulk free energy when introducing the crystal at $T<T_m$ (see Fig. 10). The second term is the free energy increase due to the interfacial energy between the crystal and its melt. The total change in free energy is

3 dim. $\Delta G(R) = (4\pi R^3/3)\, L(T-T_m)/T_m + \gamma\, (4\pi R^2).$ (3.3a)

2 dim. $\Delta G(R) = (\pi R^2)\, L(T-T_m)/T_m + \gamma\, (2\pi R).$ (3.3b)

Eq. (3.3a) is plotted in Fig.12 together with the separate surface and volume contributions (Eq. 3.2). Without the surface tension term ΔG_A, $\Delta G(R)$ would be negative for all $T<T_m$ and the system could always lower its free energy by solidifying the whole volume. With surface tension included a nucleus must be at least of size $R=R^*$, where R^* is the radius at the maximum of ΔG, for solidification to proceed beyond the "nucleation barrier". Using Eq. (3.3) we can easily determine the radius R^*, called the *critical radius*. Inverting that relation we get an expression relating the undercooling $\Delta T=T_m-T_i$ of the melt to R^*:

3 dim. $\Delta T = 2T_m\gamma / LR^* = T_m\gamma\kappa / L$ (3.4a)

2.dim. $\Delta T = T_m\gamma / LR^* = T_m\gamma\kappa / L$ (3.4b)

where κ is the curvature of the sphere ($2/R^*$) and the circle ($1/R^*$) respectively. Eq. (3.4) is the *Gibbs-Thompson relation* expressing the change in equilibrium temperature for a curved interface under the influence of surface tension. It describes a thermodynamically unstable state. Any small fluctuation away from R^* will make the crystal either grow or shrink since $\Delta G(R=R^*)$ is a maximum (see Fig.12).

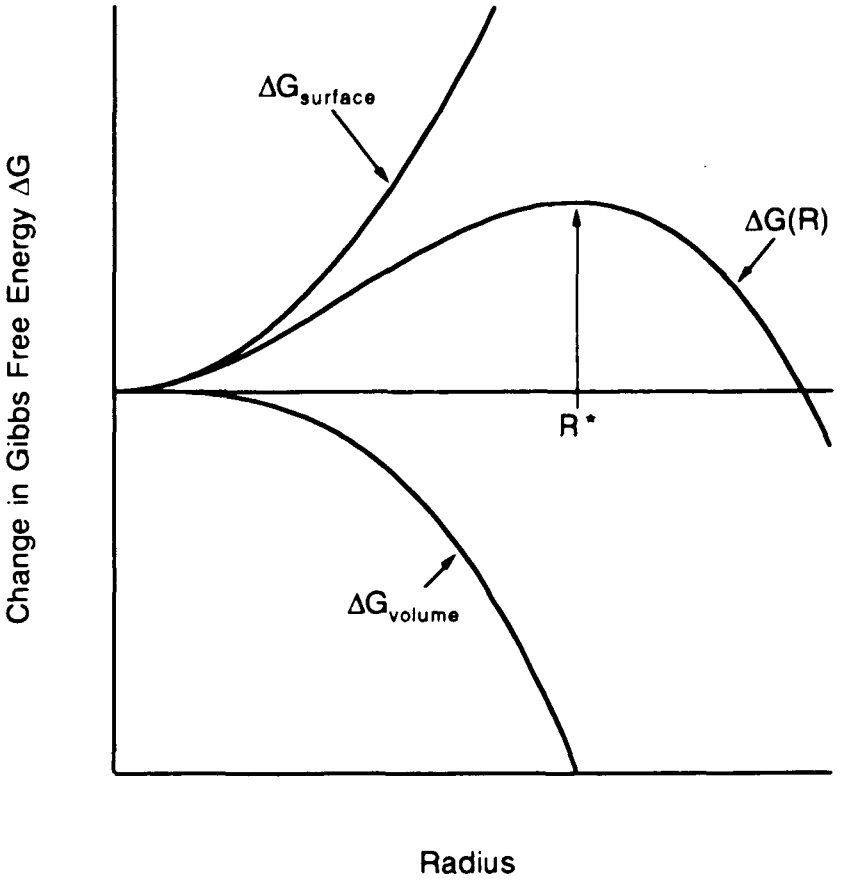

Fig. 12: Gibbs free energy of a spherical crystal with surface tension as function of crystal radius R at a fixed temperature $T_i<T_m$. It is the sum of the surface and volume contribution shown here as well. Note the maximum in G at the critical radius R*.

3.2. Crystal Shape and Surface Tension

In the previous section we derived the relation between the undercooling of a spherical crystal and its radius R (Eq. 3.4). In this section we want to find the shape of a crystal which minimizes its free energy under the constraint of constant volume (for ref. see [V2] or [M5]). We will limit the discussion to two dimensions.

The total surface free energy E_γ of a crystal surrounded by its melt is

$$E_\gamma = \oint \gamma(\hat{n})\, ds \tag{3.5}$$

where $\gamma(\hat{n})$ is the crystal-melt surface tension, $\hat{n}$ is the unit normal to the interface pointing into the melt and ds is the element of arc length. We introduce a Cartesian coordinate system fixed at the center of the crystal (see Fig. 13) and rewrite (3.5) only for the upper half of the crystal

$$E_\gamma = \int_A^B \gamma(\hat{n})\, ds = \int_A^B \gamma(y')\sqrt{1+y'^2}\, dx \tag{3.6}$$

where the prime denotes a derivative with respect to x. In two dimensions we can represent the dependence of γ on the normal vector $\hat{n}$ by $\gamma(y')$. The constraint of fixed volume is simply

$$\int_A^B y\, dx = \text{constant} \tag{3.7}$$

We impose this constraint by introducing a Langragian multiplier λ and minimizing the quantity

$$I(y,y') \equiv \int_A^B \left(\gamma(y')\sqrt{1+y'^2} - \lambda y\right) dx. \tag{3.8}$$

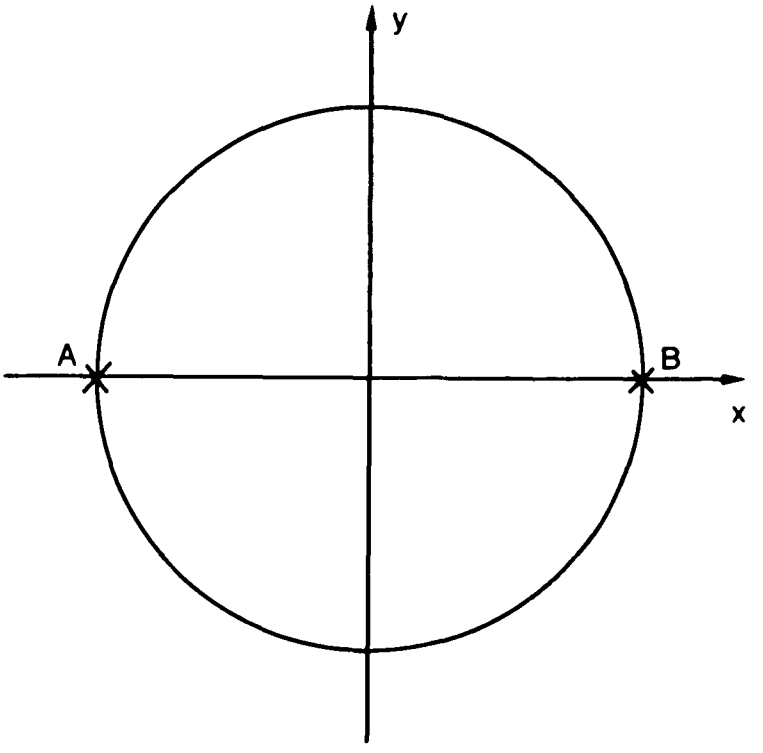

Fig. 13: Two-dimensional crystal with coordinate system in its symmetry center.

Minimization of I(y,y') requires

$$0 = \frac{\delta I}{\delta y} = \int_A^B \left(\frac{\partial \Gamma}{\partial y} \delta y + \frac{\partial \Gamma}{\partial y'} \delta y' \right) dx \tag{3.9}$$

$$= \delta y \frac{\partial \Gamma}{\partial y'}\bigg|_A^B + \int_A^B dx \delta y \left(\frac{\partial \Gamma}{\partial y} - \frac{d}{dx} \frac{\partial \Gamma}{\partial y'} \right)$$

where the second line follows from integration by parts and the quantity Γ is defined as

$$\Gamma(y, y') \equiv \gamma(y') \sqrt{1 + y'^2} - \lambda y \tag{3.10}$$

This yields the two equations:

$$\frac{\partial \Gamma}{\partial y} - \frac{d}{dx} \frac{\partial \Gamma}{\partial y'} = 0 \tag{3.11}$$

and

$$\delta y \frac{\partial \Gamma}{\partial y'}\bigg|_A^B = 0 \tag{3.12}$$

Eq. (3.12) is always true as long as we look at a closed figure and add up the contributions from the upper and the lower half. Eq. (3.11) is the standard form of the Euler-Lagrange Equation.

3.2.1. Isotropic Surface Tension

For isotropic surface tension γ= const. and we can evaluate the second term on the l.h.s. of (3.11) to

$$\frac{d}{dx}\left[\frac{d\Gamma}{dy'}\right] = \gamma \frac{d}{dx}\left[\frac{d}{dy'}\sqrt{(1 + y'^2)}\right] = \gamma \left(\frac{y''}{\left(1 + y'^2\right)^{3/2}} \right) = \gamma \kappa \tag{3.13}$$

where κ is the curvature of the interface y(x). Eq. (3.11) becomes:

$$\lambda = \gamma \kappa \quad . \tag{3.14}$$

Eq. (3.14) shows that the curvature of the crystal equilibrium shape is constant. The obvious solution is a circle in two dimensions or a sphere in three dimensions. This confirms our implicit assumption about the equilibrium shape made in the derivation of Eq. (3.3). Using Eq. (3.4) and Eq. (3.14) we can evaluate the Langrangian multiplier as

$$\lambda = L\Delta T/T_m \tag{3.15}$$

3.2.2. Anisotropic Surface Tension

If the surface tension depends on crystalline orientation, we get:

$$\frac{d}{dx}\left[\frac{d\Gamma}{dy'}\right] = \frac{d}{dx}\left[\frac{d\gamma}{dy'}\sqrt{1+y'^2} + \gamma\frac{y'}{\sqrt{1+y'^2}}\right] \tag{3.16}$$

Notice that neither γ nor y' are explicit functions of x. We can therefore express the total derivative in (3.11) as:

$$\frac{d}{dx} = \frac{\partial}{\partial x} + \frac{\partial y'}{\partial x}\frac{\partial}{\partial y'} \overset{\Gamma \neq \Gamma(x)}{=} y''\frac{\partial}{\partial y'} \tag{3.17}$$

The r.h.s. of (3.16) is now

$$\frac{d}{dx}\left[\frac{d\Gamma}{dy'}\right] = -\kappa\left[\gamma - \left(1+y'^2\right)\left(2y'\frac{d\gamma}{dy'} + \left(1+y'^2\right)\frac{d^2\gamma}{dy'^2}\right)\right] \tag{3.18}$$

The first term on the right hand side of (3.18) is the same as in Eq. (3.14). The second term can be rewritten as

$$\gamma_{\theta\theta} = \left(1+y'^2\right)\left[2y'\frac{d\gamma}{dy'} + \left(1+y'^2\right)\frac{d^2\gamma}{dy'^2}\right] \tag{3.19}$$

where $\gamma_{\theta\theta}$ is the second derivative of the surface tension with respect to the angle θ between the normal to the interface and the x-axis (see Appendix

A). Combining (3.15), (3.18) and (3.19) we obtain the *generalized Gibbs-Thompson Equation* in two dimensions

$$T_i = T_m [\ 1 - (\gamma+\gamma_{\theta\theta})\kappa / L\ ] \qquad (3.20)$$

3.2.3 Solution of the Two-Dimensional Gibbs-Thompson Equation

Eq. (3.20) is a second order differential equation. We can rewrite it as a set of two first order ODE's by using $\kappa \equiv d\theta/ds$ and $dy = ds\cos\theta$ and $-dx = ds\sin\theta$ [V2]

$$\frac{dx}{d\theta} = -\frac{T_m}{T_m - T_i}\ \frac{\gamma+\gamma_{\theta\theta}}{L}\sin\theta \qquad (3.21a)$$

$$\frac{dy}{d\theta} = \frac{T_m}{T_m - T_i}\ \frac{\gamma+\gamma_{\theta\theta}}{L}\cos\theta \qquad (3.21b)$$

At uniform melt temperature T_i Eqs. (3.21) can be integrated [V2]:

$$x = \frac{T_m}{(T_m - T_i)L}\left(\gamma\cos\theta - \gamma_\theta\sin\theta\right) \qquad (3.22a)$$

$$y = \frac{T_m}{(T_m - T_i)L}\left(\gamma\sin\theta + \gamma_\theta\cos\theta\right) \qquad (3.22b)$$

For a weakly anisotropic material with m-fold rotational symmetry an approximate expression for the surface tension $\gamma(\theta)$ is [V2] :

$$\gamma(\theta) = \gamma_o\,[1+\varepsilon_m\cos(m\theta)] \qquad (3.23)$$

Substituting (3.23) into (3.22) for m=4 and taking different values of ε_4 we get the shapes shown in Fig.14. As ε_4 increases, increasingly prominent bulges appear along the four axes, reducing the fraction of interface with

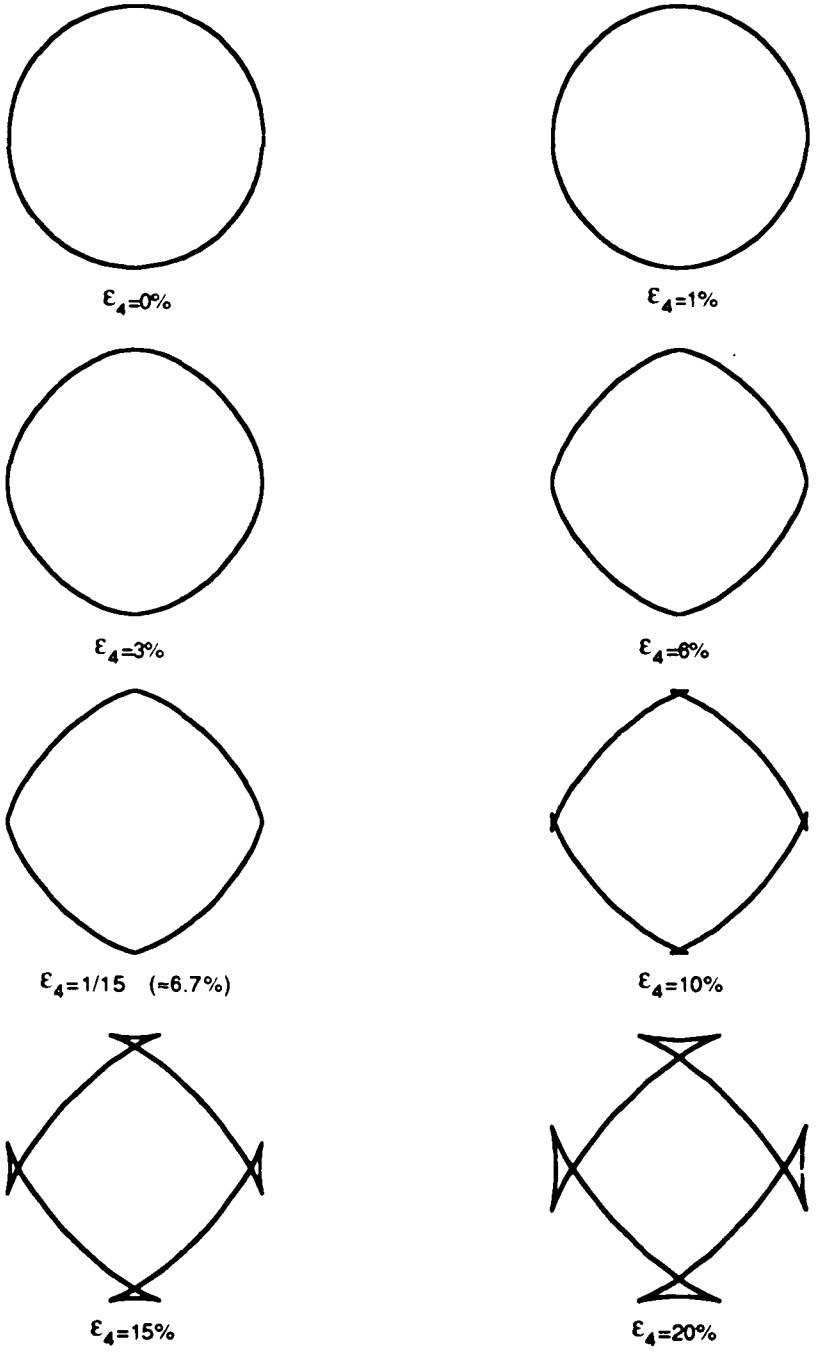

Fig. 14: Equilibrium shapes of a two-dimensional crystal with four-fold symmetric surface tension. The crystals are shown for increasing values of the surface tension anisotropy ε_4. Note the appearance of ears for $\varepsilon_4 > 1/15$. The true equilibrium shape is the one without the ears.

large values of $\gamma(\theta)$. For values of $\varepsilon_4 \geq 1/15$ ears develop in the solutions and the true equilibrium shape is the one we get by discarding those ears [V2]. The resulting figures for $\varepsilon_4 \geq 1/15$ have cusps at their four corners.

3.2.4. The Wulff Construction and Cusps in the Interface Shape

Another way to determine the equilibrium shape of a crystal is a geometrical method due to G.Wulff [W2]. His construction starts with a polar plot of the surface tension $\gamma(\theta)$. The length of a radius vector at each angle θ is given by the absolute value of $\gamma(\theta)$. Fig.15 shows such a figure for $\gamma(\theta)$ given in Eq. (3.23). We draw a plane perpendicular to each radius vector at its end point on the curve $\gamma(\theta)$. Wulff's Theorem states that the equilibrium shape of a crystal is the inner envelope of all the perpendicular planes of its corresponding $\gamma(\theta)$-plot(see Fig.15).

Herring [H3] proved that this construction is equivalent to the shape obtained as a solution of the generalized Gibbs-Thompson Equation (3.20). He also explained the presence of cusps in the equilibrium shape using the Wulff construction [H4]. Cusps appear when a range of interface orientations is missing from the equilibrium crystal shape. Across a cusp the orientation of the interface normal θ_1 on one side of the cusp discontinuously jumps to a new value θ_2 on the other side of the cusp. Look at the polar plot of $\gamma(\theta)$ close to one of the orientations where cusps appear, let's say at $\theta=0$ (see Fig. 16). We add a circle with its center halfway between the origin and $\gamma(\theta=0)$ and of radius $R=\gamma(0)/2$. Now assume that the radius of curvature of the γ-plot at this point is smaller than this circle. Part of the γ-plot then lies inside the circle. We draw a radius vector from the origin to any point on $\gamma(\theta)$ inside the circle, as indicated by point A. The normal

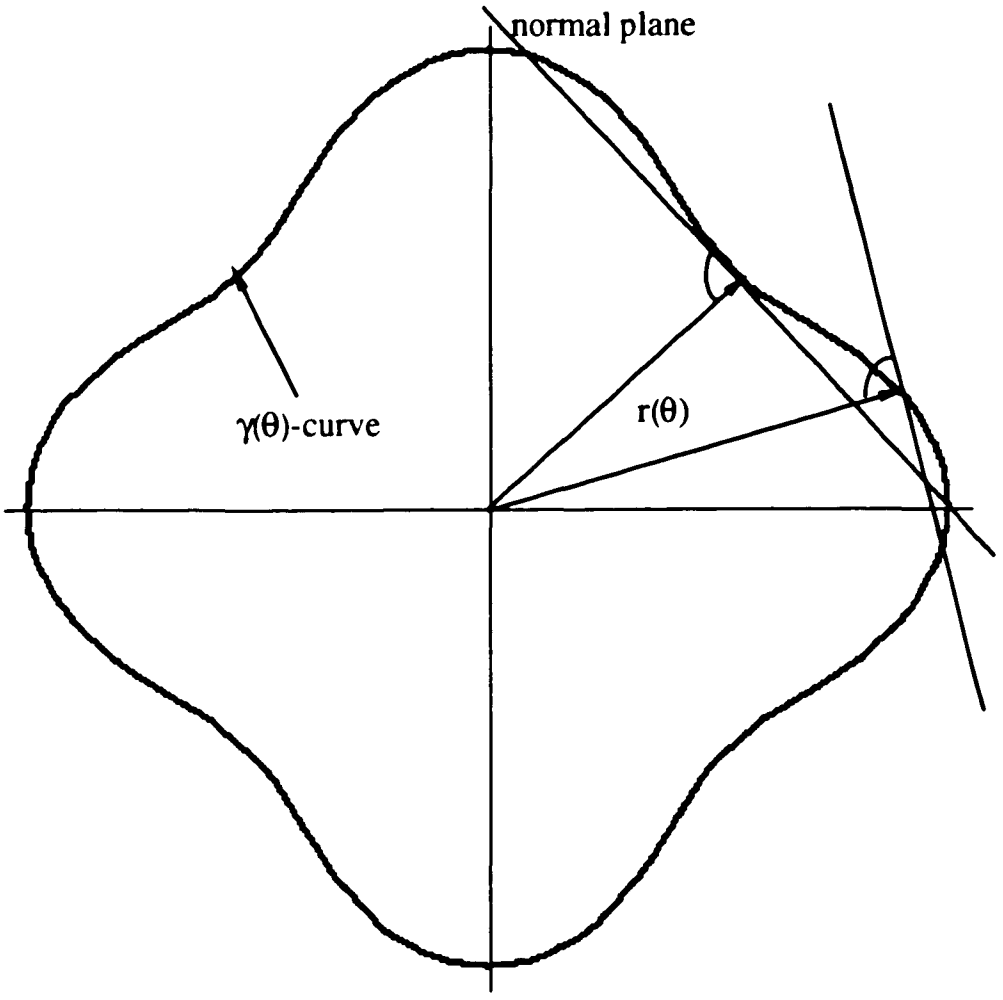

Fig. 15: Polar plot of the surface tension in Eq. (3.23) for m=4 and ε_4 = 0.15. Two radius vectors $r(\theta)$ from the origin to the $\gamma(\theta)$ curve are drawn in together with normal lines at tips of the respective vector. According to Wulffs theorem, the equilibrium shape is the inner envelope of all normal planes.

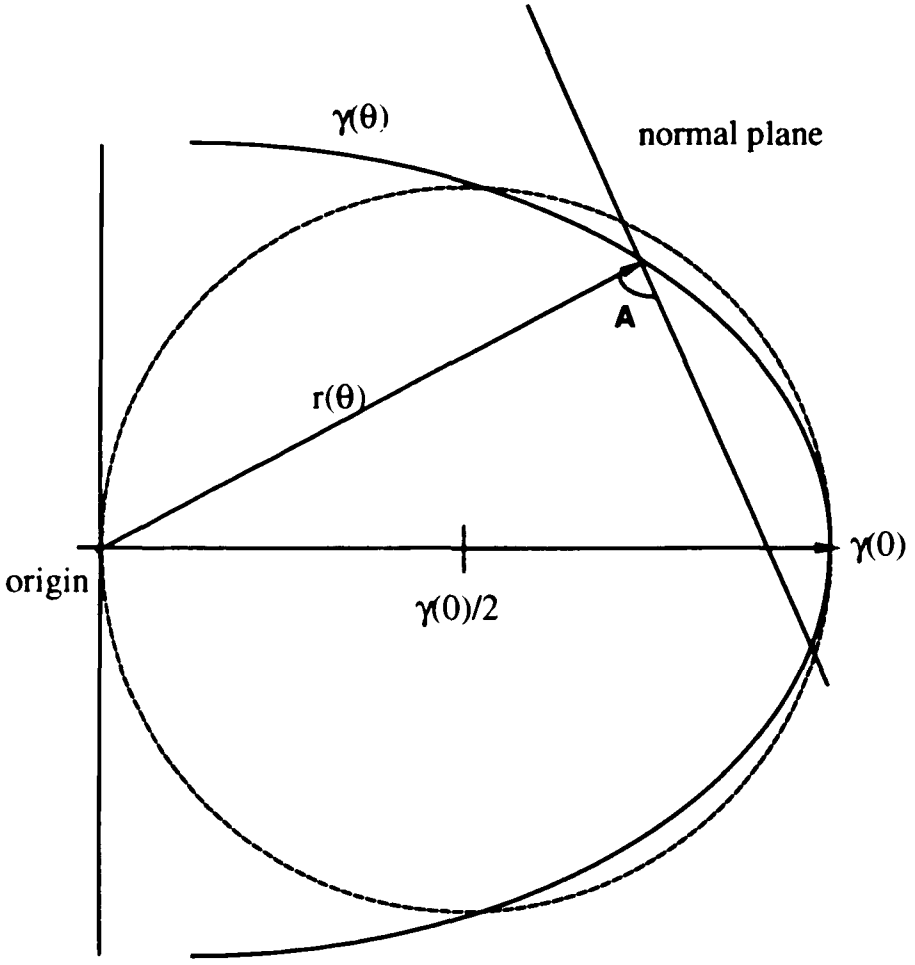

Fig. 16: Detail of the polar plot of $\gamma(\theta)$ in the direction $\theta=0$. The dotted circle has its center at $\gamma(0)/2$ and is of radius $\gamma(0)/2$. The radius vector $r(\theta)$ touches a part of $\gamma(\theta)$ that lies inside the dotted circle. Its normal crosses the $r(\theta=0)$-vector and cuts this orientation out of the equilibrium shape.

to this radius vector will always intersects the radius vector $\gamma(\theta=0)$. The corresponding normal of $\gamma(\theta=0)$ is therefore not part of the inner envelope of all normals to the $\gamma(\theta)$-plot and the orientation $\theta=0$ is excluded from the resulting crystal equilibrium shape. This yields a local criterion for the appearance of cusps: the radius of curvature of the γ-plot at $\theta=0$ has to be larger than $\gamma(\theta=0)/2$ or

$$\kappa(\theta=0) \geq 2/\gamma(0) \tag{3.24}$$

The curvature κ in polar coordinates is

$$\kappa = \frac{\gamma^2 + 2\gamma_\theta^2 - \gamma\gamma_{\theta\theta}}{(\gamma^2 + \gamma_\theta)^{3/2}} \tag{3.25}$$

Applied to (3.23) we can rewrite (3.24) as

$$\gamma + \gamma_{\theta\theta} \leq 0 \tag{3.26}$$

or expressed in terms of the surface tension anisotropy, the condition for the appearance of cusps in the equilibrium shape is

$$\varepsilon_m \geq 1/(m^2-1) \tag{3.27}$$

which, for m=4, recovers the condition $\varepsilon_4 > 1/15$ found numerically in the preceding section.The theory of microscopic solvability discussed in chapter 2 excluded crystals with cusps in the equilibrium shapes. It is therefore convenient to introduce a rescaled measure of the anisotropy strength

$$\alpha_m \equiv (m^2-1)\varepsilon_m \tag{3.28}$$

For $\alpha_m \geq 1$ cusps appear in the equilibrium shape, independent of the crystal symmetry m.

3.2.5. Approximate Crystal Shape for Small Anisotropies

Combining the Gibbs-Thompson relation (3.20) with the surface tension anisotropy (3.23) an approximate solution for the interface shape $R(\phi)$ can be found (R,ϕ are the polar coordinates of the interface):

$$R(\phi) = R_0 [\ 1 + s_m \cos(m\phi)\ ] \tag{3.29}$$

where R_0 and $s_m << 1$ are free parameters. s_m measures the *shape anisotropy* of the crystal. For small s_m, $\phi \approx \theta$ and to first order in s_m

$$\kappa(\theta) \approx (1/R_0) [\ 1 + (m^2-1)\, s_m \cos(m\phi)\ ] \tag{3.30}$$

Together with (2.23), the generalized Gibbs-Thompson relation yields

$$R_0 = R^* \tag{3.31a}$$

$$s_m = \varepsilon_m \tag{3.31b}$$

where R^* is the critical radius of nucleation. To this approximation the surface shape anisotropy s_m is identical with the anisotropy in γ. In order to compare the exact and approximate solution we generated polar plots $R(\phi)$ of equation (3.29) for m=4 and varying values of ε_4. These plots were Fourier analyzed as

$$R(\phi) = \Sigma\, R_0 [\ 1 + s_j \cos(j\phi)\ ] \tag{3.32}$$

for $j \leq 10$. The result for the four-fold shape anisotropy s_4, divided by the predicted ε_4 from (3.31b) is shown in Fig.17. Up to the threshold for cusps ($\varepsilon_4 = 1/15$) the maximum disagreement between s_4 and ε_4 is less than 10%. For values of ε_4 <3%, with which we will be most concerned, the agreement with s_4 is well below our experimental limit of resolution. The only other Fourier component with significant amplitude is $\cos(8\phi)$. Its amplitude reaches almost 20% of the value for ε_4 at the limit $\varepsilon_4 = 1/15$(the ratio s_8/ε_4 is also shown in Fig.17).

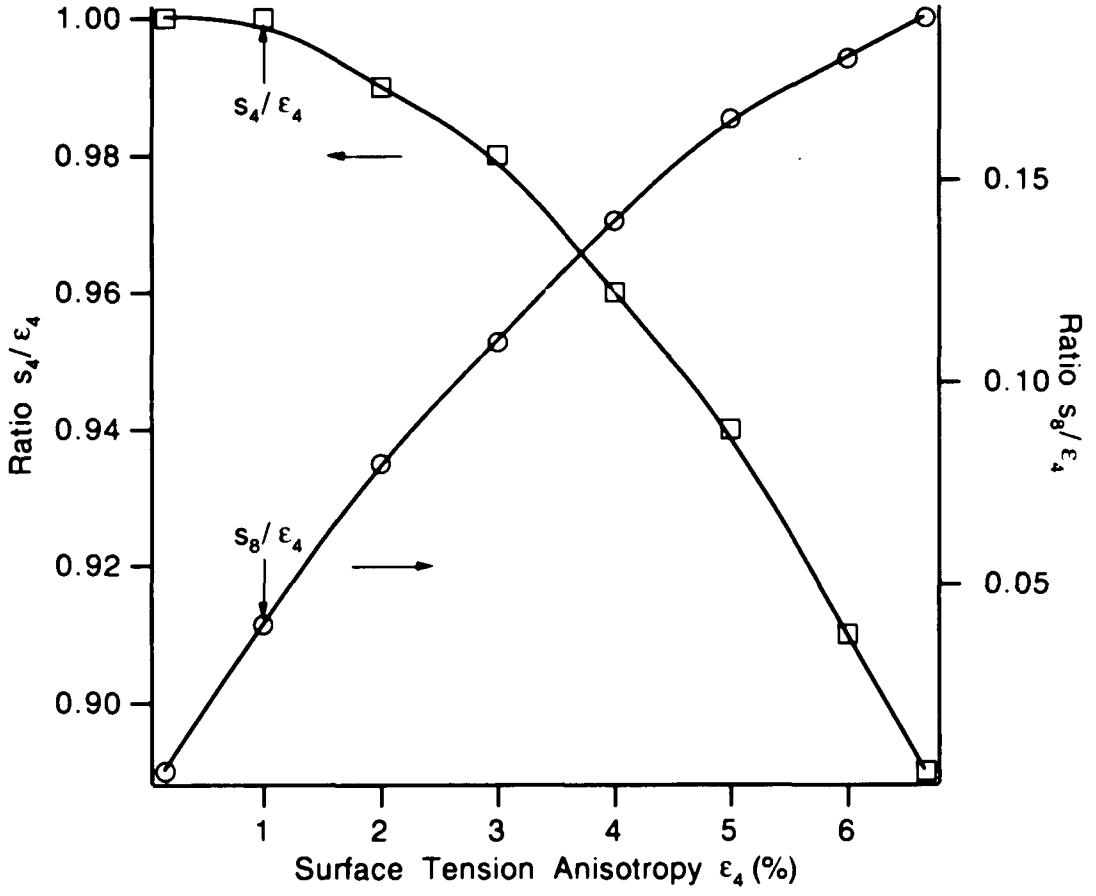

Fig. 17: Fourier amplitudes s_4 and s_8 of the numerical solutions of Eqs. (5) using the surface tension form of Eq. (3). Both s_4 and s_8 are normalized to ε_4 and plotted against ε_4. Note that for $\varepsilon_4 < 0.03$, s_4 and ε_4 agree to better than 2%. (The solid lines are guides to the eye).

3.3. Crystal Shape Under the Influence of a Radial Temperature Gradient

In real experiments, the presence of temperature gradients tends to suppress the shape anisotropy of a crystal. Consider a crystal located in the center of a radially symmetric linear temperature gradient G. In polar coordinates (r, o) T(r) has the form

$$T(r) = T_O + Gr \tag{3.33}$$

Since at equilibrium the interface temperature T_i of Eq. (3.20) must equal the local T(r), we have

$$T_O + Gr = T_m [\, 1 - (\gamma + \gamma_{\theta\theta})\kappa/L] \tag{3.34}$$

3.3.1. Approximate Solution

We can try to find an approximate solution of the form (3.29). Combining Eqs. (3.23), (3.30), and (3.34) for m=4, and collecting terms in ascending orders in s_4, we find

$$T_O+GR_O = T_m(1 - \gamma_O/LR_O) \tag{3.35a}$$

$$-(G/T_m)\, s_4\, R_O = (15\gamma_O/LR_O)(s_4 - \varepsilon_4) \tag{3.35b}$$

Eq. (3.35a) determines the average radius R_o. For G=0 we get back Eq. (3.31a). With the gradient included, however, Eq. (3.35a) is a quadratic equation in R_o which may have zero, one, or two solutions. In Fig.18 we have plotted the two sides of Eq. (3.35a) separately for the case with two solutions. The smaller solution R_u is unstable since a small increase in R will bring the crystal surface to a position where the local

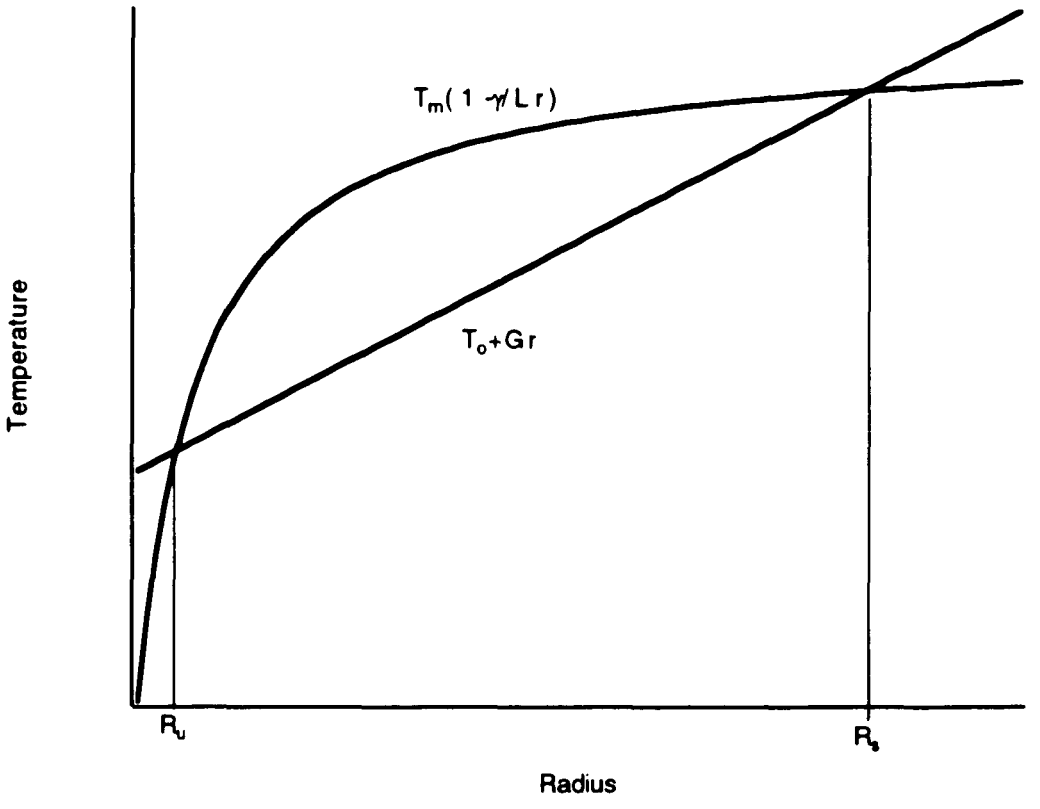

Fig. 18: Plots of the two sides of equation (3.35a) indicating two solutions at $r=R_u$ and $r=R_S$. Note the different stabilities of the two solutions.

temperature T_o+GR is below the surface melting temperature, and the crystal will grow. Similarly, a decrease in R will cause the crystal to melt. This solution, therefore, corresponds to the usual unstable solution in the uniform undercooling case. Conversely, the second solution at R_s is absolutely stable.

Eq. (3.35b) shows that the temperature gradient suppresses the shape anisotropy relative to the uniform undercooling case where $s_4 = \varepsilon_4$. This result is physically reasonable since the bulges will now extend into a warmer region of the melt and will therefore be reduced relative to the uniform undercooling case. It is useful to rewrite Eq. (3.35b) in the form

$$s_4/\varepsilon_4 = [\, 1 + G/(15G_c)]^{-1} \qquad (3.36)$$

where $G_c = \gamma_o T_m/LR_o^2$ has the dimensions of a temperature gradient. In Fig. 19(A) we plot s_4/ε_4 vs. G for crystals with radii between 50 μm and 1000 μm, all with anisotropy of ε_4= 0.005. These data were obtained from numerical solutions to the exact equations, to be discussed in the following section. The shape anisotropy is more strongly suppressed for the larger crystals, as expected, since their bulges extend farther into the higher temperature region. If we scale the gradient G by G_c, Eq (3.36) predicts a universal plot for s_4/ε_4 as shown by the solid line in Fig 19(B). This figure also shows that the shape anisotropy is not significantly different from ε_4 until the gradient G is well above G_c.

The physical significance of the critical gradient G_c can be found from the Gibbs-Thompson equation (3.20) for isotropic surface tension where the interface temperature T_i and equilibrium radius R_o are related by $T_i=T_m$ [1-γ/Lr] . The derivative of T_i with respect to r, evaluated at $r=R_o$, is

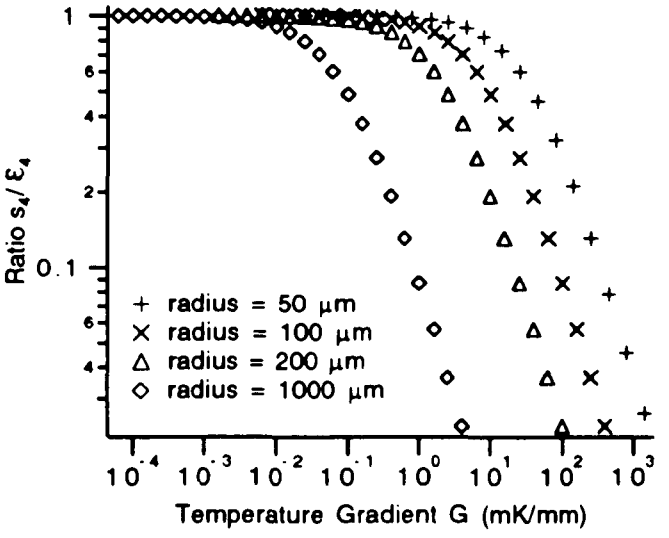

Fig. 19(A): Influence of a temperature gradient G on the shape anisotropy for crystals of different size. The material parameters used to generate these plots where those of SCN and the anisotropy was chosen to be ε_4=0.5%.

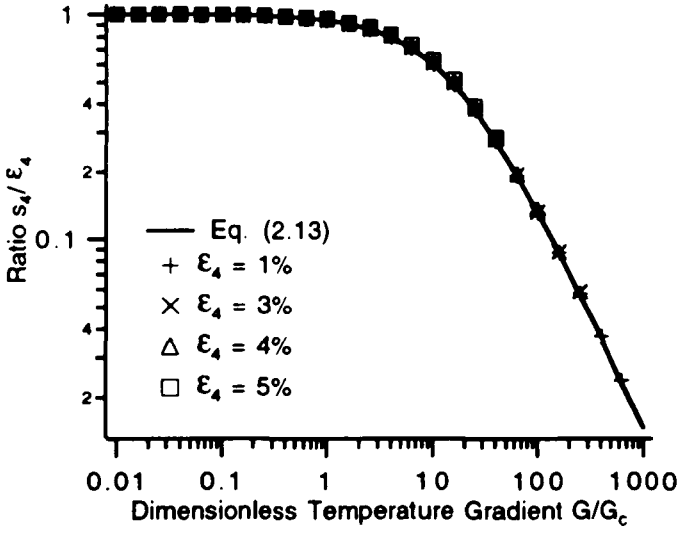

Fig 19(B): Data from Fig 19(A), and for three additional values of ε_4, plotted against the dimensionless gradient G/G_c. The solid line is the scaling prediction of Eq. (3.36).

$$(dT_i/dr)_{R_0} = \gamma T_m / L R_0^2 \qquad (3.37)$$

Eq. (3.37) shows that G_c is just the slope of the melting point curve at the radius R_0. As can be seen from Fig.18, $G < G_c$ implies an unstable solution while $G > G_c$ implies a stable one. Note, however, that even for unstable solutions with $G < G_c$,the presence of a gradient will reduce the instability, increasing the time it takes for a crystal with $R=R_u$ to grow or shrink appreciably.

3.3.2. Numerical Solution

To determine the range over which the scaling behavior in (3.36) is valid, we solved the problem numerically, following ideas by Voorhees et al. [V2]. We transform Eq. (3.34) into two first order equations analogous to (3.21)

$$\frac{dx}{d\theta} = -\frac{T_m}{T_m - T_o - Gr} \frac{\gamma + \gamma_{\theta\theta}}{L} \sin\theta \qquad (3.38a)$$

$$\frac{dy}{d\theta} = \frac{T_m}{T_m - T_o - Gr} \frac{\gamma + \gamma_{\theta\theta}}{L} \cos\theta \qquad (3.38b)$$

These two first order, parametric ODE's for the interface coordinates (x,y) are coupled through the presence of the temperature field T(r). Due to the symmetry of the surface tension $\gamma(\theta)$, we only need to solve (3.38) in the parameter range $\theta \in [0, \pi/4]$. The boundary conditions we impose are

$$y = 0 \quad \text{for} \quad \theta = 0 \qquad (3.39a)$$

$$x = y \quad \text{for} \quad \theta = \pi/4 . \qquad (3.39b)$$

This is a two-point boundary value problem and we use a relaxation method as outlined in ref. [P2] to solve it. Details of the algorithm are

discussed in Appendix B. The resulting interface shapes are equivalent to the shape of a crystal at uniform undercooling but reduced surface tension anisotropy ε_4 (see Fig.20). To compare the numerical results with the scaling relation in Eq. (3.36) we generated a set of interface shapes for fixed average radius and ε_4 but varying values of the temperature gradient G. Then we modified the value of the average crystal radius keeping the surface tension anisotropy ε_4 unchanged, or vice versa, and repeated the calculations. The values of the shape anisotropy s_4 of these numerically generated interfaces in comparison to Eq. (3.36) are plotted in Fig.19(B). Over the range of surface tension anisotropies $\varepsilon_4<1/15$ the agreement with the scaling relation Eq. (3.36) is excellent.

3.4. Crystal Shape in Three Dimensions

In the previous two sections we discussed the equilibrium shape and stability properties of a two-dimensional crystal at uniform undercooling as well as in the presence of a linear, radially symmetric temperature field. Experimentally we observe two-dimensional projections of a three-dimensional crystal. To extend the analysis to this situation we start with the Gibbs-Thompson relation in three dimensions [M5]

$$\frac{T_m - T_i}{T_m} = \frac{1}{L}\left[\left(\gamma + \gamma_{\theta_1\theta_1}\right)\kappa_1 + \left(\gamma + \gamma_{\theta_2\theta_2}\right)\kappa_2\right] \qquad (3.40)$$

where θ_1,θ_2 are the angles along the principal axis of the surface and κ_1,κ_2 are its corresponding principal curvatures.The equivalent to our four fold symmetric surface tension in (3.23) is the cubic-symmetric function [K10]

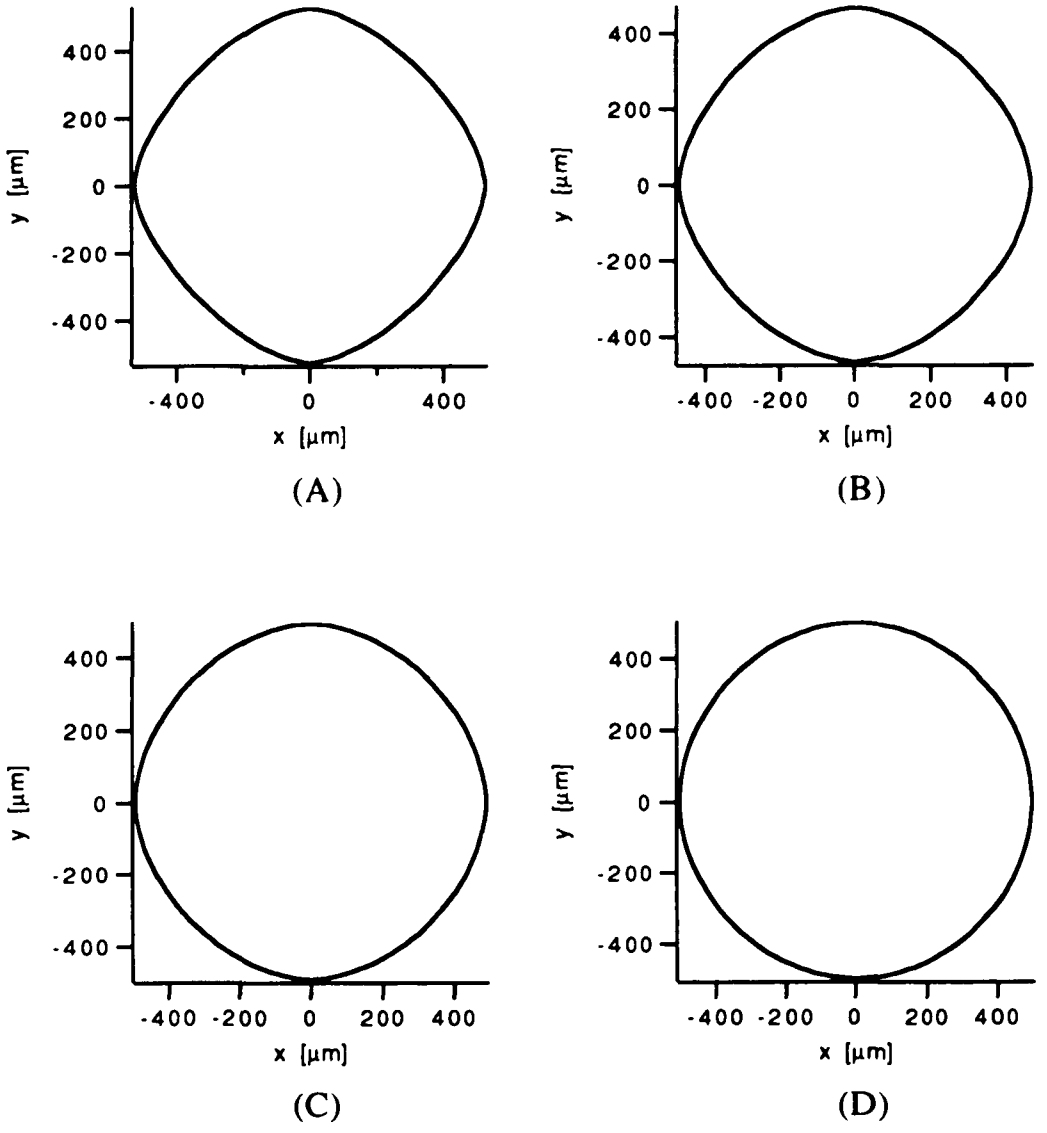

Fig. 20: Shape of two-dimensional crystals with anisotropic surface tension in a radial temperature gradient of increasing size. The surface tension anisotropy was set to ε_4=5%, all other material parameters used to generate this figure are those of SCN. The gradients imposed were:
(A) 0 mK/mm (B) 2 mK/mm (C) 5 mK/mm and (D) 20 mK/mm

$$\gamma(\theta,\phi) = \bar{\gamma}\left\{1 + \varepsilon_4\left[4\left(\sin^4 4\theta\left[\cos^4 4\phi + \sin^4 4\phi\right] + \cos^4 4\theta\right) - 3\right]\right\} \quad (3.41)$$

where $\theta \in [0,\pi]$ and $\phi \in [0,2\pi]$ are the usual angles in spherical coordinates. Fig.21 shows three plots of this function viewed from different directions. We have slightly altered the form of $\gamma(\theta,\phi)$, as given in ref. [K10], so that (3.41) goes over into (3.23) in the x-y plane ($\theta = \pi/2$), the x-z plane ($\phi = 0$), or the y-z plane ($\phi = \pi/2$). The shape of the corresponding three dimensional crystal at uniform undercooling was derived by Cahn and Hoffman [C8] and can be expressed in Cartesian coordinates by [V1]

$$x = \frac{2T_m}{L(T_m - T_i)}\left[\gamma \sin\theta\cos\phi + \gamma_\theta \cos\theta\cos\phi - \gamma_\phi \sin\phi/\sin\theta\right] \quad (3.42a)$$

$$y = \frac{2T_m}{L(T_m - T_i)}\left[\gamma \sin\theta\sin\phi + \gamma_\theta \cos\theta\sin\phi - \gamma_\phi \cos\phi/\sin\theta\right] \quad (3.42b)$$

$$z = \frac{2T_m}{L(T_m - T_i)}\left[\gamma \cos\theta - \gamma_\theta \sin\theta\right] \quad (3.42c)$$

For small ε_4, the equilibrium shape of the 3-dim. crystal is again equivalent to $\gamma(\theta,\phi)$ as given in (3.41). When looking at $\gamma(\theta,\phi)$ from the [1,1,1] direction it is clear that the crystal will show three- and six-fold components (see Fig.21B & 21C). Experimentally we have to make sure that the crystal is properly oriented. Under those conditions, the values we extract for ε_4 using a 2-dim. model to analyze the projections of a 3-dim. crystal produces the correct value for the surface tension anisotropy of the 3-dim. crystal.

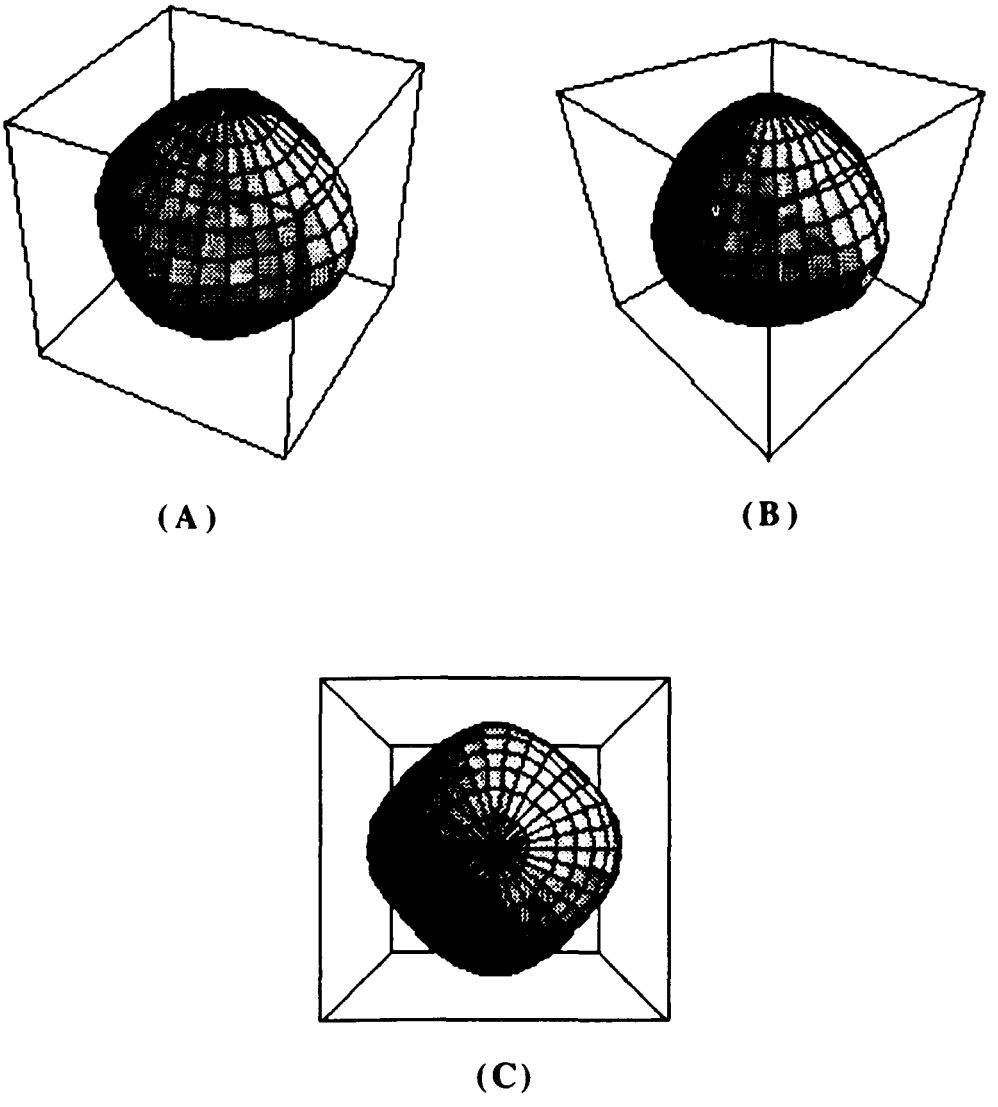

Fig. 21: Three views of the three-dimensional anisotropic surface tension function $\gamma(\theta,\phi)$ of Eq. (3.41) for ε_4 =0.05. In (B), the normal is along a [1,1,1] axis, while in (C) it is along a [1,0,0] axis.

4. Review of Dendritic Growth Experiments and Anisotropy Measurements of Transparent Materials

4.1. Introduction

Interest in dendritic growth phenomena originates from its importance in metal casting, since the solidification microstructure will determine the quality of the finished cast. "...Even after heavy working,...a solidification structure and its associated defects are difficult to eliminate once they are created" [K11]. However, experiments on the morphology of metals are difficult to perform and evaluate, since metals have generally high melting points and are opaque. Standard techniques of investigation are to examine cross sections of solidified specimens or to decant the melt from the container quickly during solidification. Direct observation of the propagating growth morphologies during solidification are rare [G6]. This limits the use of metals in experimental investigations of dendritic growth. Reviews of experiments in metal systems are provided e.g. by Jackson et. al [J3], Chalmers [C9], Glicksman [G3] or de Cheveigne [D2].

In 1958 Jackson published his theory on the transition from faceted to microscopically rough crystal-melt interfaces [J4,J5]. He found that this transition depended on the parameter $\alpha \equiv L\xi/RT_m$, where L is the molar latent heat, ξ is the the ratio of the number of nearest-neighbor atoms in the bulk and at the interface, R is the gas constant and T_m is the equilibrium melting temperature of the material. For values of $\alpha \geq 2$ the equilibrium shape of the crystal-melt interface is atomically smooth and the crystal is faceted while for $\alpha < 2$ the interface will be rough. The microscopically rough interfaces of metals allow them to form the smooth

dendritic growth structures observed in nature. Using the α-factor of materials as guidance Jackson investigated a whole series of transparent plastic crystals, all with microscopically rough interfaces, and found them to form dendrites during solidification of their melts [J6]. This opened the field of dendritic growth to convenient in-situ observations under the microscope [H5].

In the following section we will review experiments on free dendritic growth into undercooled melts or supersaturated solutions of transparent materials followed by a discussion of surface tension anisotropy measurements. In section 2 we discussed the theory of steady-state dendritic growth into pure undercooled melts. For binary mixtures diffusion in the solid is negligible while for pure systems, thermal conduction in the solid phase is usually comparable to the conduction in the liquid phase. The corresponding theoretical models are the one-sided and the symmetric model. Equation (2.56), derived by Barbieri and Langer [B15], relates the values of the selection parameter σ^* for these two models. When using appropriately rescaled quantities for supersaturated solutions, the theoretical discussion of section 2 becomes applicable to both systems. In table 1 we summarize the definitions of the comparable quantities for pure and binary systems. During the discussion of the experiments it should be obvious from the context which definition of, for example, the capillary length is appropriate.

Relevant physical constants of the pure substances reviewed in the following section are listed in table 2. A summary of selection parameters σ^*_{exp} and surface tension anisotropies ε_m is given in table 3.

4.2. Free Dendritic Growth

4.2.1. Plastic Crystals

a. Succinonitrile

Glicksman et al. performed extensive experiments on high purity specimen of *succinonitrile* ($NC(CH_2)_2CN$, abbreviated as SCN), prepared by multi-stage zone-refining [R1]. Their apparatus consists of a spherical glass flask of about 3-4 cm dia. with the tip of a capillary tube at its center [G2,H2]. The flask is filled with the high-purity material while hermetically sealed from the environment and then submerged into a temperature controlled water bath. Dendrites can be launched into the melt through the small capillary tube. Experiments were performed at undercoolings ΔT between 0.1°C and 10°C ($\Delta \in [0.0043,0.43]$). Only within the range 0.1°C to 2.0°C could they observe clearly developed single dendrites. Beyond this range, several dendrites emerged simultaneously from the capillary and produced a compact growth figure with an almost spherical envelope. For undercoolings $\Delta T \leq 0.75$°C convection started to increase the experimental growth speeds. Within the range of useful undercoolings ($\Delta T \in [0.75,2.0°K]$) they measured the growth speed v of dendrites for several different values of ΔT. Repeating the experiments at the same undercoolings, they photographed the dendritic tip. The tip radius ρ was extracted from these photographs by fitting parabolas of known curvature to the tip region. Two important results emerged. First of all, as noted above in section 2.3.1., the experimentally observed growth speeds were not in accord with the maximum growth speed hypothesis [G2]. Furthermore, the selection parameter σ^*_{exp}, i.e. the value of σ (see Eq.

(2.30)) using the experimentally observed values of ρ and v, was constant and had the value $\sigma^*=0.0192$ [H2]. From the observed growth speeds at high undercoolings they obtained an estimate of the kinetic coefficient $\beta^{-1} \geq 20$cm/sK [G2].

The study was extended to binary mixtures of SCN with acetone and argon, respectively [C9,G4]. These experiments were performed at undercoolings of $\Delta T=0.1$°C to 1°C and varying concentrations of the binary component. For a fixed undercooling of the melt, the dendritic growth velocity first increased with impurity concentration, reached a maximum and then decreased again when increasing the impurity content further. The maximum in the SCN-acetone system occurred at about 0.1 mol% acetone concentration for an undercooling of 0.5°C. Lipton et al. [L9,L10] as well as Karma and Langer [K12] explained this phenomenon within the framework of marginal stability. They claimed that the competition between two effects is the origin of the velocity maximum. On one hand the slow chemical diffusivity would reduce growth rates overall. On the other hand, the selection parameter σ^* for this thermo-chemical system is increased leading to an increase in the selected speed. I'm not aware of a comparable explanation using the ideas of microscopic solvability theory. This observation is important when evaluating experiments of free dendritic growth in binary systems. These are usually carried out at small impurity concentrations and therefore are highly susceptible to the above competition between thermal and chemical effects.

Honjo et al. [H7] roughened the surface of a glass cell containing SCN to emulate varying degrees of anisotropy in the system. A phase diagram of cell anisotopy vs. undercooling identifies five different

morphologies: parabolic dendritic growth, tip-oscillating dendrites, symmetric tip-splitting, asymmetric tip-splitting and DLA-like patterns.

Chou and Cummins [H1] observed an array of SCN dendrites propagating into the melt. They measured a primary spacing between the parabolic tips of ≈350 μm at a growth speed of v≈0.45 μm and tip radius of ≈16μm.

b. Pivalic Acid

Free dendritic growth of *pivalic acid* ($C_5H_{10}O_2$) was studied in pure systems [S6,R2] in the same set-up used by Glicksman for pure SCN [G2]. The melt was undercooled from ΔT=0.04°C to 0.86°C. In contrast to SCN, the value of σ^* varied from ~0.042 at ΔT=0.04°C to ~0.020 at ΔT=0.86°C [R2]. Given Glicksman's comments about the onset of convection in SCN [H2], it is not clear how to interpret this result.

Dougherty [D3] grew pivalic acid dendrites with 1% by weight of ethanol added as impurity. As sample cells he used capillaries of cross section 10x1mm inside a regulated temperature stage. He used digital image processing methods, originally developed for his NH_4Br experiments [D4], to determine the tip radius with high accuracy. His values of σ^* show considerable scatter as a function of growth speed v with an overall tendency to decrease for increasing v. The value he quotes for σ^* is 0.05±0.02.

c. Cyclohexanol and Camphene

Other free dendritic growth experiments in plastic crystals include measurements in *cyclohexanol* [S6] and *camphene* [R3] again performed in Glicksman's laboratory. The range of undercoolings for cyclohexanol was

0.1°C to 0.86°C and for camphene was 0.28°C to 2.02°C. Both materials show $v\rho^2$ to be constant.The value found for σ^* in cyclohexanol is 0.027. Since the surface tension γ is unknown for camphene, the value of σ^* in camphene could not be determined. Rubinstein [R3] uses the marginal stability hypothesis to deduce γ, but this seems inadmissible for our purpose.

4.2.2. Ionic Crystals in Aqueous Solutions

Honjo and Sawada [H6] prepared aqueous solutions of *ammonium bromide* (NH_4Br) with a saturation temperature of 67.5°C. Their growth tubes were capillaries of 0.5mm diameter. Supercooling temperatures varied from 0.5°C to about 10°C. Within these parameters $v\rho^2$ remains constant and using their v vs. ΔT and ρ vs. ΔT relationships we can estimate $\sigma^*=0.072\pm0.037$.

Dougherty and Gollub [D4] performed the first experiments specifically intended to test microscopic solvability theory. All relevant material parameters needed (capillary length d_0, chem. diffusion constant D and surface tension anisotropy ε_4) were carefully measured (see table 2 and table 3). The solution contained 51% NH_4Br and had a saturation temperature of 56°C. The capillaries had a cross section of 1x1 mm^2. From simultaneous radius and velocity measurement, using digital image analysis, they found $\sigma^*=0.081\pm0.02$.

Maurer et al. [M6] observed NH_4Br dendrites in round glass cells with radii between 30mm and 50mm and heights between 0.15mm and 1mm. Saturation temperatures of their solutions are 30°C and 42°C and undercoolings from 0.5°C up to 3°C are used. At small undercoolings

dendrites form with facets at their tip. With increasing undercooling the extent of the facets gradually diminishes until the dendrites go over to the usual parabolic growth shapes. This shape transition is accompanied by a change in dynamical behavior as well. For faceted crystals the product $v\rho^2$ is constant but smaller by a factor of two than in the smooth tip regime. In the transitional region of undercoolings, the value of $v\rho^2$ smoothly raises from the lower to the upper plateau values. The plateau value of the 'regular dendrites' yields the same result for σ^* as observed by Dougherty.

In an extension of their work Maurer et al. [M9] grew ammonium bromide dendrites into a supersaturated gel. The experimental set-up is the same as in their previous experiment. There are three important differences compared to the aqueous solution growth. The noise in the $v\rho^2$ data is significantly reduced and for the same supersaturation that Dougherty used, their $\sigma^*=0.120\pm0.025$. Furthermore, $v\rho^2$ is not constant for different supersaturations.

Ammonium Chloride (NH_4Cl) solutions were studied by Chan et al. [C10], Honjo et al. [H8,H9,O2] and Raz et al. [R4]. Chan grew dendrites over a wide range of supersaturations at a fixed temperature of T=25°C. Most noticeably, they found a transition in the selected growth direction. Starting at low supersaturations with dendrites growing along the [100]-direction, the dendrites switched to growth along the [110]-direction at higher supersaturations and finally started to grow along the [111]-direction. The latter transition went hand in hand with a steep increase in growth velocity. These observations might correspond with recent consideration of a morphological transition from 'surface tension dendrites' to 'kinetic dendrites' [L11,B16].

Honjo et al. worked with an aqueous ammonium bromide solution of 42.6 wt% and a saturation temperature of 35.0°C [H8]. The growth cells were only 5μm thick which makes their system close to two-dimensional. Similar to their results in ammonium bromide they find regular, tip-oscillating and tip-splitting dendrites. In the 'regular dendritic' regime the product $v\rho$ is apparently constant rather than $v\rho^2$. For low supersaturations the parabolic tip turns increasingly spherical and the tip-oscillating behavior sets in. At high supersaturations the tip-splitting mode appears. The dendritic tip growing into the [100]-direction splits into two tips aligned along the [110]-direction. Finally the tip recovers and the whole process repeats itself again. Further investigations [H9,O2] deal with DLA growth patterns when roughening the cell surface. The fractal dimensions of these DLA-patterns is $d_f = 1.671 \pm 0.002$.

Raz et al. [R4] imaged the concentration field in front of a growing ammonium chloride dendrite with an interference microscope. The method exploits the dependence of the refractive index on solute concentration. The shapes of the dendrites they observed don't fit a parabola well. The concentration fields also don't match a simple diffusive solute distribution but show that finite undercoolings persist all the way up to the crystal interface. They suggest that their dendrites are faceted similar to the experiments of Maurer in ammonium bromide [M6] and that their concentration fields are strongly influenced by kinetic effects. Furthermore they detect periodic tip oscillations of the dendrite coupled to the emergence of sidebranches. This behavior is markedly different than the observations of sidebranching activity in NH_4Br by Dougherty et al. [D5].

4.2.3. Dendritic Growth of Noble Gases

Dendrites in pure ^{4}He were investigated by Franck and Jung [F1] at pressures between 260 and 6500 bar, corresponding to a range of melting temperatures between 5.4 K and 46.0 K. Below 1120 bar or below melting temperatures of 15.0 K, ^{4}He has hcp structure, while above this range the structure is fcc. The undercooling changed from about 0.1 K to 2 K relative to the equilibrium melting temperature T_m. The impurity content was below 1ppm. Observations were made in optical high-pressure cells and recorded with a video camera. The velocity-radius data show a large scatter but within the fcc-phase of ^{4}He $v\rho^2 = 2.5 \times 10^{-8}$ cm^3/sec is constant. The corresponding value of $\sigma^*=0.0013$ is based on several estimates of crucial material parameters, which include the thermal diffusivities of the solid and liquid phases, surface tension, specific heat, and latent heat. Unfortunately, the authors had experimental difficulties getting quantitative results in the hcp-phase, but they do report drastic changes in the crystal morphology and dendritic shape across the fcc-hcp transition.

Bilgram et al. [B17-20] observed dendrites in krypton and xenon at very small undercoolings ($0.005 < \Delta T < 0.3$ K) in a vessel of about 4.5 cm linear dimension. From simultaneously measured tip radius and growth velocity data they derive the following scaling laws:

krypton: $v = (6.33 \pm 0.12) \times 10^{-4}\ \Delta^{1.729 \pm 0.007}$

$\rho = (1.16 \pm 0.04) \times 10^{3}\ \Delta^{-0.683 \pm 0.010}$

xenon: $v = (7.87 \pm 0.92) \times 10^{-4}\ \Delta^{1.745 \pm 0.017}$

$\rho = (0.93 \pm 0.09) \times 10^{3}\ \Delta^{-0.685 \pm 0.014}$

This leads to a σ^* vs. Δ-relationship that slightly decreases with undercooling. It is conceivable that this trend is due to finite size effects.

For their range of growth speeds of $5x10^{-6} < v < 5x10^{-3}$ cm/sec and the quoted value of $D_T \approx 7\ x10^{-4}$ cm^2/sec the corresponding diffusion length is $0.28 < l_D < 280$ cm. Again the value of σ^* is based on several estimates of material parameters, but we obtain from their results $\sigma^*=0.017\pm0.009$ in krypton and $\sigma^*=0.022\pm0.012$ in xenon.

4.2.4. Dendrites in Water

Water has been investigated by many authors [F2,H10,K13,K14, L12,M7,M8,P5,T2,T3,W3]. Two of the most important experiments are those of Fujioka [F2] and K.Koo et al. [K13]. Fujioka observed ice dendrites for $0.2 < \Delta T < 0.5$°C in a three-dimensional growth cell. His data showed $v\rho^2$ to be constant and gave $\sigma^*=0.025$.

Koo et al. [K13] extended the undercooling range to $0.035 < \Delta T < 1.0$°C in a three dimensional growth chamber very close in design to Glicksman's. The water purity was estimated to be 99.999%. For undercoolings $\Delta T \leq 0.35$°C the tips of the dendrites underwent a tip-splitting instability. $\sigma^* \approx 0.075$ can be estimated from their Fig. 13. Unfortunately, the authors do not give fits to their v vs. Δ or ρ vs. Δ curves and do not mention the value for the surface tension γ they assume to obtain σ^*.

4.2.5. Liquid Crystals

S. Arora et al. [A2] investigated *4-n-buthyl-N-[4-(p-cyanophenyl)-benzylidene]anilene* in ≈7μm thin cells . This liquid crystal has isotropic-nematic, nematic-smectic1, and smectic1-smectic2 phase transitions at 274,

80 and 75°C respectively. The growth patterns are observed at the nematic-smectic transition. Three different morphologies are observed: radial dense branching, planar dense branching and dendritic patterns. The transition was most likely controlled by diffusion of impurities.

Dendrites of *hexaoctyloxytriphenylene* (HET) were grown by P. Oswald et al. [O3, O4] at the transition between hexagonal and isotropic phases at T=84.4°C. The phase diagram as well as the surface tension and its anisotropy were experimentally determined. Dendritic morphologies were seen for supersaturations $0.2< \Delta < 0.6$. Below $\Delta=0.2$ a petal-shape regime existed while above $\Delta=0.6$ dense branching morphologies developed [O4]. Measurements of the dendritic growth speed and radius of curvature were performed for $\Delta=0.3$. At this supersaturation the observed value of $\sigma^* = 0.038$.

4.3. Previous Measurements of Surface Tension Anisotropy

The importance of surface tension anisotropy ε_m in microscopic solvability theory has been discussed extensively in chapter 2. But there are only five materials for which this parameter has been determined experimentally: succinonitrile (SCN) , pivalic acid (PVA), hexaoctyloxy-triphenylene (HET), ammonium bromide and ice. These measurements are all based on the observation of the equilibrium shape of either a melt-inclusion in the solid [G4,G6,H2,R2] or of a crystal surrounded by its melt [D3,D4,O3]. A summary of the results is given in table 3. The theoretical aspects of this problem were laid out in chapter 3.

Glicksman was the first to report a value for the surface tension anisotropy of SCN derived from observations of melt inclusions

[G4,G6,H2]. These inclusions are about 0.3 mm in diameter, separated by about 0.6mm from a neighboring droplet (as seen in ref. [H2], Fig 4.). The anisotropy of the material is determined by assuming the approximate solution for the crystal shape given in Eq. (3.29) and (3.31).The surface tension anisotropy ε_4 can be expressed as

$$\varepsilon_4 = (R_{max}-R_{min}) / (R_{max}+R_{min}) \qquad (4.1)$$

where $R_{max}= R(\phi=0) = R^*(1+\varepsilon_4)$ and $R_{min}=R(\phi=45^\circ)=R^*(1-\varepsilon_4)$. Measuring the maximum and minimum radius of the photographic image of a droplet, Glicksman reported a value of ε_4 =1% [H2], later revised to 0.5% [G5,S6]. The same method was applied to PVA and ε_4 =5% was given as the result [R2]. There are several objections to the use of liquid inclusions inside the melt to obtain equilibrium shapes. First, for a pure material and $T_i<T_m$ only crystals inside the melt are allowed, but not vice versa, since the sign of the curvature term in the Gibbs-Thompson relation for isotropic surface tension (Eq. 3.4) changes for a liquid inclusion inside a solid. The right hand side becomes negative, requiring $T_i>T_m$. But the solid phase is not stable above T_m. Pure liquid inclusions are therefore not a state of equilibrium. This argument changes if we allow for impurities in the melt. They will accumulate inside the droplet and can lead to a sufficient suppression of the melting temperature to make the inclusion the thermodynamically stable state at $T<T_m$. A further problem with the use of liquid inclusions is the interactions between neighboring droplets. If the photographs of SCN (ref. [H2], Fig 4) and camphene droplets (ref. [R3], Fig. 7) are typical, then it seems difficult to obtain droplets which are separated by more than twice their diameter. The presence of grain boundaries complicates the problem even more. Which process dominates the equilibration of the system? Coarsening of the crystal grains in the solid

or the assumed equilibration of the liquid inclusion? These considerations suggest that results for surface tension anisotropies obtained from shape observations of droplets inside the solid should be regarded with some caution. There are some recent observations of liquid inclusions in ice [K13], camphene [R3], and cyclohexanol [S6], for which the same criticism applies. The value for the six-fold anisotropy in ice in the basal plane was given as ε_6=0.002±0.001 [K13], for camphene the two-fold anisotropy was measured as ε_2 = 0.03 [R3] and for cyclohexanol no values are quoted.

The anisotropy of NH_4Br was measured by Dougherty and Gollub [D4] as part of their effort to test microscopic solvability. The experimental set-up was described above. Single crystals of about 50μm diameter in equilibrium with their supersaturated solution were observed. They allowed the crystals to equilibrate for about 1.5 hours. To enhance the resolution of the video images, Dougherty interpolated the interface coordinates from the intensity profile across the crystal-melt boundary and achieved sub-pixel resolution of about 0.2 pixels. Fourier-analyzing the radial interface profiles so obtained, the value of the shape anisotropy extracted from these data is ε_4= 0.016±0.004. For PVA [D3] Dougherty changed the method slightly by including a video feed-back to his temperature control in order to maintain the crystal at constant radius for extended periods of time (up to several days). The measurements yielded ε_4 = 0.006±0.002.

Oswald [O3] looked at a single domain of the hexagonal phase in equilibrium with the isotropic phase of HET. The diameter of the domain was ≈150μm and he allowed it to equilibrate for a day, keeping the temperature constant. Photographing the equilibrated crystal and using microdensitometry on the negative he achieved a resolution of about

0.1μm. The six-fold anisotropy of HET was found to be $\varepsilon_6 = 0.026 \pm 0.012$. This value is 35 times smaller than that cited by Oswald in his paper and corresponds to his Eq. (5) revised to read $R(\theta) = R_0 [1 - \varepsilon_6 \cos(6\theta)]$ (see chapter 3.2.5. for an explanation).

5. Anisotropy Measurements: Procedures and Results

5.1. Principle of the Experiments

Our essential procedure is to establish a single small, properly-oriented crystal in equilibrium with its surrounding melt. We record the shape of the crystal-melt interface by video- microscopy with a CCD video camera, and generate digital images of it with a computer-based video board. The digital images are further processed to obtain an accurate set of polar interface coordinates (r_i, ϕ_i). Fourier-analysis of these data allows us to extract the value of the surface tension anisotropy ε_4 for that crystal. In the following we review the experimental procedures and methods of analyzing the data in detail.

5.2. Experimental Apparatus

5.2.1. Sample Preparation and Characterization

The experiments are performed with three different types of samples: pure SCN, pure PVA and a binary sample of PVA and 1% ethanol by weight. The starting materials for our sample preparation, SCN (Fluka, 99%) and PVA (Aldrich Chemicals, 99%) are vacuum distilled four times, with the first 10 and last 30% of each round rejected. A mechanical pump provides a vacuum of about 150 mtorr, resulting in a boiling temperature for the two materials of 110 and 60°C, respectively, at which the distillation is carried out. The only difference in the preparation of the two materials is due to the strong tendency of PVA to sublimate. We therefore

chill the flask containing PVA before pumping all the glassware down to vacuum pressure. After closing the connection to the vacuum pump we proceed with the distillation as in the case of SCN. The distillation flasks have Teflon stopcocks and can be sealed vacuum tight after receiving the distilled material. This way we can switch flasks and store the purified materials without risk of contamination due to air exposure.

The remains of the starting material after the first distillation tend to be of a deep brown color and are obviously contaminated. All further distillations leave perfectly transparent material. The four times distilled material is finally transferred into a multi-neck flask. This allows us to fill our material under vacuum into clean glass capillaries and torch seal them to prevent any future contamination.

The capillaries are purchased from Vitro Dynamics (Rockaway,N.J.) They are roughly 30 cm long and have a cross-section of 200 x 4000 μm. We clean them by funnelling a 'liqui-nox' lab cleaning solution through them, followed by Chromerge and finally rinsing them extensively with distilled water. A flow vacuum helps to suck the fluids through the narrow capillaries. After preliminary drying by blowing dry nitrogen gas through them, the capillaries are put into a long glass tube. The tube is evacuated, warmed with heating tapes to about 200°C and left over night. The capillaries are then removed from the glass tube and torch sealed. To put them into the multi-neck flask, one end is fed through a small rubber seal with a cut just big enough to receive the capillary while the other end is broken and put into the open neck of the flask. The rubber seal is slightly lubricated with silicon vacuum grease so that we can move the capillary up and down in the flask, while still providing a tight vacuum seal.

The multi-neck flask is hooked up to the vacuum pump and a helium gas cylinder. We evacuate it and distill the pure material into it. The capillary is dipped into the still molten material and, after disconnecting the vacuum pump, the flask is slowly filled with helium to push the molten material up the capillary. We pull the capillary out of the liquid and, after the melt in the flask has solidified, the flask is put back under vacuum again. Warming up the open end of the capillary with a heat gun we remove all material close to the opening, for about 5-7 cm . We pull the emptied portion of the capillary halfway out of the flask. With a miniature torch we vacuum seal the contents of the capillary which is usually further cut down into two or three samples of 5 cm length .

The sample preparation for the binary PVA/ethanol mixture is slightly different. After purifying the PVA, we distill it into a 25 ml buret with Teflon stopcocks on both ends, add a small amount of 200 proof ethanol from a previously sealed bottle to the buret, and mix both materials thoroughly with the help of a miniature magnetic stir bar. The buret is then placed on top of the multi-neck flask and emptied into it. The capillaries are filled under a helium atmosphere. Once inside the capillary the mixture has to be chilled with ice to avoid evaporation of all the material when using the heat gun to empty the open end of the capillary.

We find that the SCN samples, prepared as described above, have a melting point that is within 5 mK of the melting temperature of a SCN-triple point cell developed by M. E. Glicksman and purchased from NIST. Using the depression of the melting point for an ideal solution

$$T_m(0) - T_m(X) = (R_g T_m^2/L)\, X \qquad (5.1)$$

where R_g is the gas constant and X is the mol fraction of impurity, we estimate the purity to be better than 99.995%. We also filled 50 x 1000 μm cross-section capillaries with the purified SCN and put those into a directional solidification set-up described elsewhere [Q1]. Even for a temperature gradient of 2°K and growth speeds of about 70 μm/sec we are unable to drive the solid-liquid interface into instability. Using constitutional undercooling concepts, the relation between the impurity concentration c_∞ of the sample and the velocity at which the sample goes unstable is [K15]

$$c_\infty = \frac{D_c}{V}\frac{G}{m_l}\frac{k}{1-k} \qquad (5.2)$$

where D_c is the value of the chemical diffusion constant of the secondary component in SCN, m_l is the liquidus slope and k is the value of the segregation coefficient. As gradient and velocity we use the values mentioned above, we take a typical value of $D_c = 10^{-5}$ cm^2/s for the chemical diffusion constant and estimate the liquidus slope from the relation (5.1) for the melting point depression of an ideal solution. The k-value for most materials is well below 0.25 and we used k=0.5. Eq. (5.2) then yields a limit to the impurity content of about 10^{-3}%, consistent with the previous result.

For the PVA samples we determine the melting point with a thermocouple to be T_m = 35.9°C, which agrees within experimental accuracy with the melting temperature of T_m = 35.935°C reported by Glicksman (see table 2). Finally the melting temperature of the binary PVA/ethanol mixture was T_m = 30.3°C. The corresponding impurity concentration, according to Eq. (5.1), is about 0.8%. It is consistent with

the experimental accuracy and implicit theoretical simplification (e.g. linear liquidus curve, ideal solution) assumed in deriving Eq (5.1). These hermetically sealed samples show no signs of aging.

5.2.2. Thermostat and Temperature Control

The thermostat is designed to fit onto the round opening of our Nikon Diaphot microscope and was build in the CCNY science division machine shop. A cross section is shown in Fig. 22. It consists of four parts: A bakelite ring, thermally isolating the thermostat from the microscope stage, an outer aluminum shell and an inner copper shell, supported by another bakelite ring separating the inner from the outer shell. Thermal insulation foam is attached to the surfaces of the outer shell, and the outer and inner shells are separated by a thin layer of Styrofoam. Both shells have a flat cylindrical shape with a round opening of 20mm diameter in the center. The openings in the outer shell are covered by glass windows. The outer windows of the inner shell are glass windows coated with a conductive, optically transparent indium-tin oxide coating (Glass-Tech Industries, Morgan Hill, CA). The two innermost windows are sapphire windows from Meller Optics, Inc (Providence, RI). The sample capillary is positioned inside the inner shell, between two 1.6mm thick glass plates, surrounded by paraffin oil for heat transfer and optical index matching.

Temperature control of the outer shell is provided by a YSI-72 proportional controller (YSI Inc., Yellow Springs, OH). The inner shell is regulated by a Tronac PTC-41 controller (Tronac Inc, Orem, UT). As heating element we use annular strip heaters with aluminum backing from Minco (Minneapolis, MN). These heaters have a resistance of $R \approx 78\Omega$ for

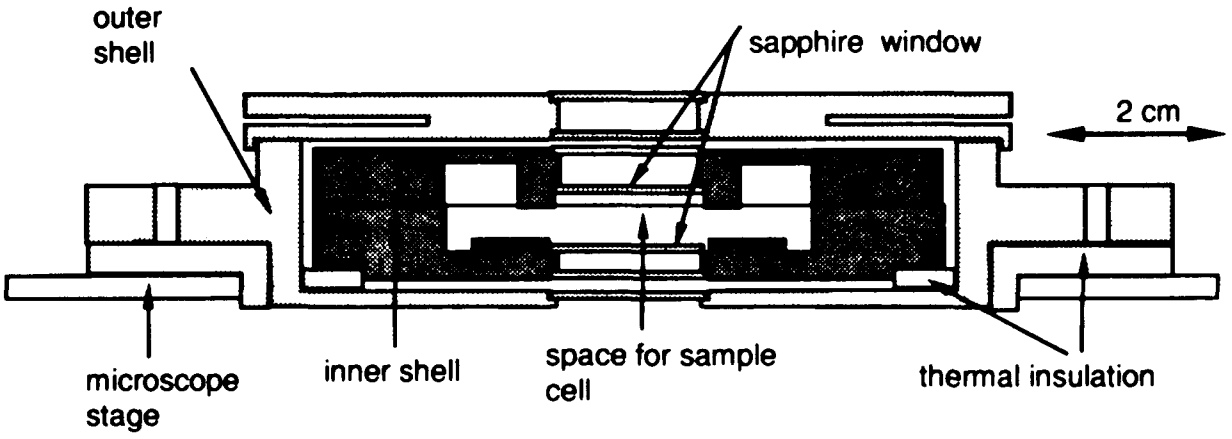

Fig 22: Cross section through the thermostated sample holder

the outer shell and R≈ 58Ω for the inner shell. The inner shell also has a small strip heater (R≈165Ω) attached to its perimeter. All heaters are glued to the outer surface of each shell with a thermally conductive epoxy, Tra-Bond BC-2151 from Tra-Con (Medford,Mass). As feedback thermistors for the temperature controllers we use custom-made electrically isolated thermistors from Thermometrics (Edison, NJ). Their resistance is chosen to match the control range of the respective controller. In addition we installed a reading thermistor in the inner shell to monitor the temperature. With this configuration we control the temperature of the outer shell to within ±5mK. The inner shell reaches a temperature stability of about ±0.5mK for several hours when keeping the outer shell temperature about 5-10°C below the inner shell temperature.

In order to reduce temperature gradients within the sample space we chose the above mentioned sequence of observation windows. They, nevertheless, produce a small heat loss at the center of the thermostat and led to a radially symmetric variation of the temperature throughout the thermostat. We measured the radial temperature dependence by positioning a thermistor in different parts of the sample space of the inner shell. A typical temperature profile is shown in Fig 23. The crystals can be trapped in the trough of this temperature profile. The estimated gradient at the boundary of a crystal of 100 μm radius is of the order of 10^{-4} mK/μm. We could heat the coated glass windows to reduce the gradient further, but this resulted in rolling of the crystal seed during the experiment and made the observations less reliable.

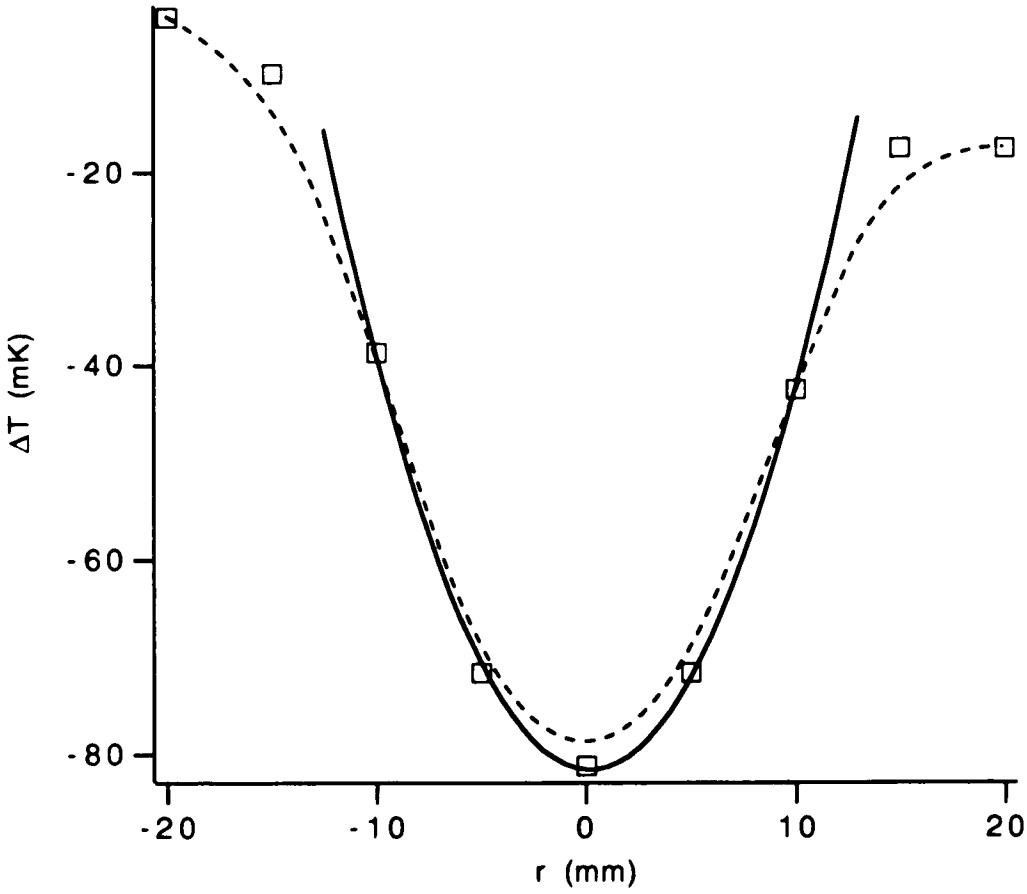

Fig. 23: Radial temperature profile of the sample space in the inner shell of the sample thermostat. The r-origin is the center of the observation window and its edges are at r= ±10mm. The squares are the measured temperature deviations relative to the uniform temperature inside the copper shell of the thermostat. The solid line is a parabolic fit to the five center points and yields: $T(r) = -81.5\ mK + 0.409(mK/mm^2) \times (r - 0.189)^2$ where r is in mm.

5.2.3. Microscope and Imaging System

A schematic overview of the whole experimental set-up is given in Fig. 24. The microscope we used is a Nikon Diaphot with inverted optics. It has a 35mm camera port and a video camera port. We typically use it with a 10x long working distance objective and a 2.5x projection lens in the video port. The images are recorded with a Dage MTI-72 CCD camera (Dage-MTI, Michigan City, IN). The video images are digitized with a 640 x 480 pixel Data Translation QuickCapture video digitizing board (Data Translation, Marlboro, MA) inside a Mac II computer. We also record the images on a Mitsubishi U31 commercial VCR for later analysis.

We calibrated our camera and image system by capturing images of circular reticules with varying diameters (500, 1000 and 1500μm dia.). Extracting the reticle interface coordinates with the same procedure as described in section 5.2.5, the resulting polar plots of the reticle interfaces show a clear two-fold variation (see Fig. 25(A)). This is independent of the orientation of the camera or the reticle. It is obviously due to a difference in the x- and y-scales of the combined camera-video digitizing system. Fitting the interface coordinates with a least squares fit to a function of the form $r(\phi) = a + b \cos(2\phi)$ we can calibrate the x- and y-coordinates of the camera. With our 10x objective and 2.5x projector combination we determined scale factors of 0.59±0.01 μm/pixel in the x-direction and of 0.62±0.01 μm/pixel in the y-direction. After correcting for this difference we obtain almost perfectly round images of our reticle, independent of the orientation of the reticle or the camera (see Fig. 25(B)). We do not find any noticeable geometric distortions throughout the viewfield.

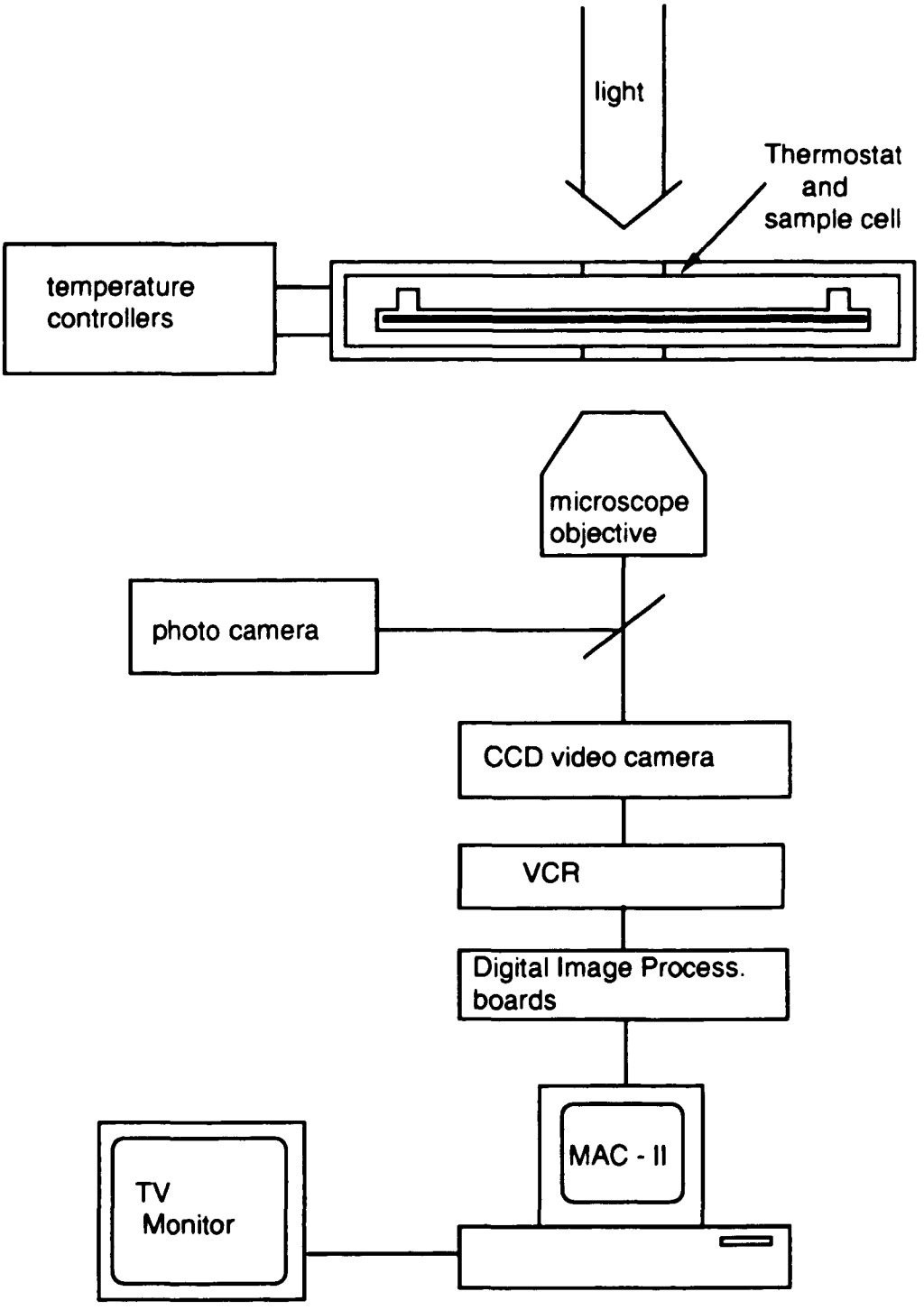

Fig. 24: Schematic overview of the experimental set-up.

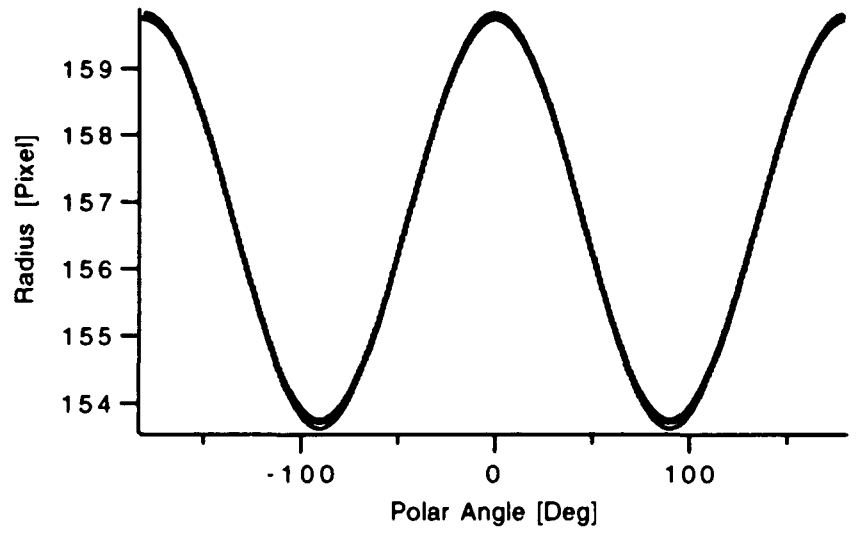

Fig. 25 (A): Extracted polar interface coordinates of 1000μm dia. reticle using 4x objective and 1x projector. Note the clear twofold distortion.The solid line is a least square fit with the function $r(\phi) = a + b \cos(2\phi)$ through the data.

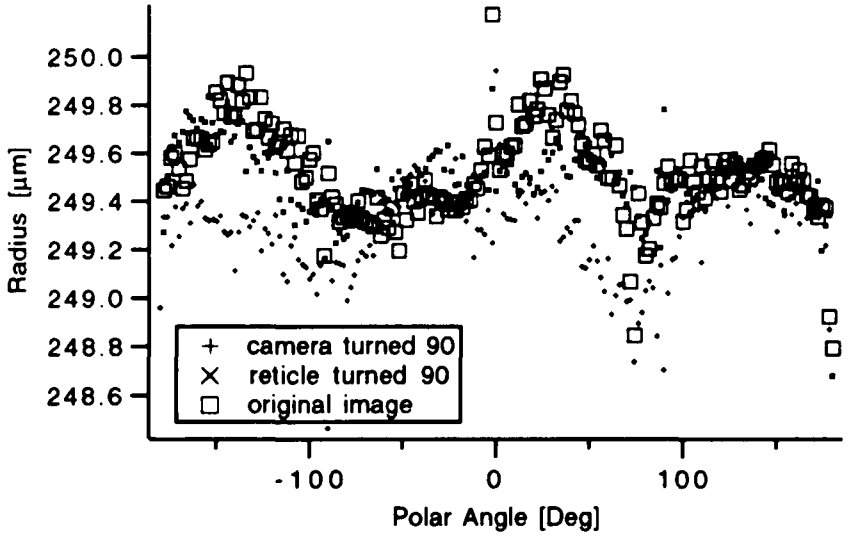

Fig. 25 (B) Extracted polar coordinates of 500μm dia. reticle using 4x objective and 1x projector. Now the image is corrected for the different pixel height in the x- and y-direction.

5.2.4. Experimental Procedure

Warming up previously frozen samples in order to establish a seed, we frequently obtain odd crystal shapes which sometimes never reach the expected equilibrium shape (see Fig. 26). We interpret this as a sign of multiple grain structures inside the crystal seed. In a typical experimental run, we therefore first thenheat the outer shell of the thermostat to a temperature 5°-10° K below the melting temperature of the sample (in the case of PVA/ethanol the outer shell is not heated). The inner shell is then heated until the whole sample is completely molten. We then cool the sample until it starts to solidify by spontaneous nucleation of crystallites, producing numerous small single-crystalline grains which have no time to form multiple grain structures.

When the sample is warmed back up close to its melting temperature, the grains close to the center of the observation window melt last, due to the temperature dip in the center of the thermostat. We are usually able to capture a single crystal grain in the center of the capillary. At this point we quickly undercool it. For PVA, the orientation of the dendritic arms that shoot out from the initially round seed allows us to assess the orientation of the crystal (see Fig. 27). We are not able to accurately determine the orientation of our SCN seeds with this procedure since after rapid cooling they usually exhibited a dense-branching morphology rather than clearly developed dendritic arms (see Fig. 28).

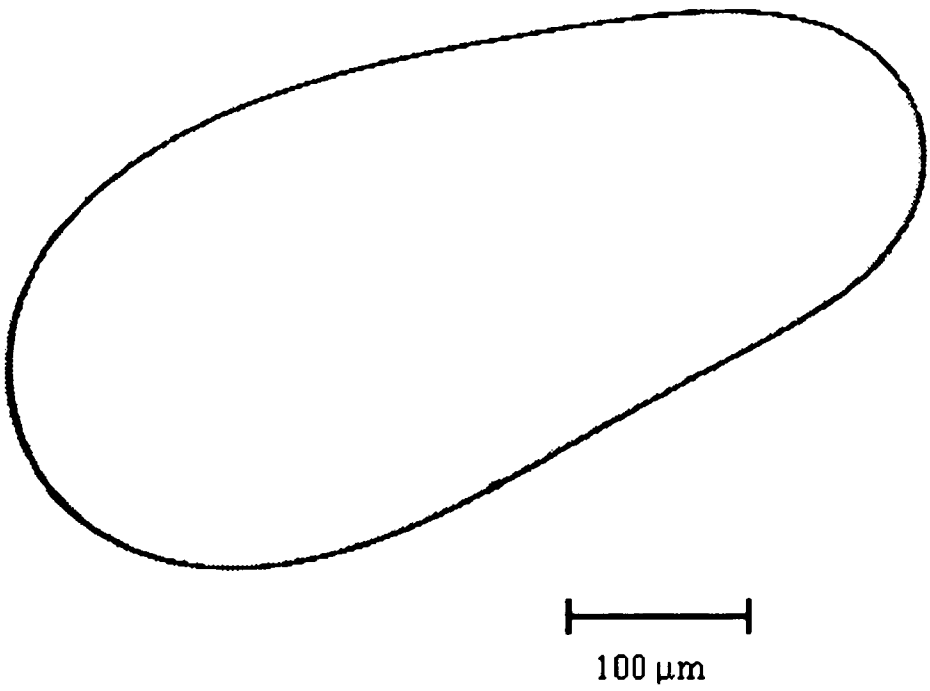

Fig. 26: Typical odd crystal shape obtained when starting from a previously frozen sample.

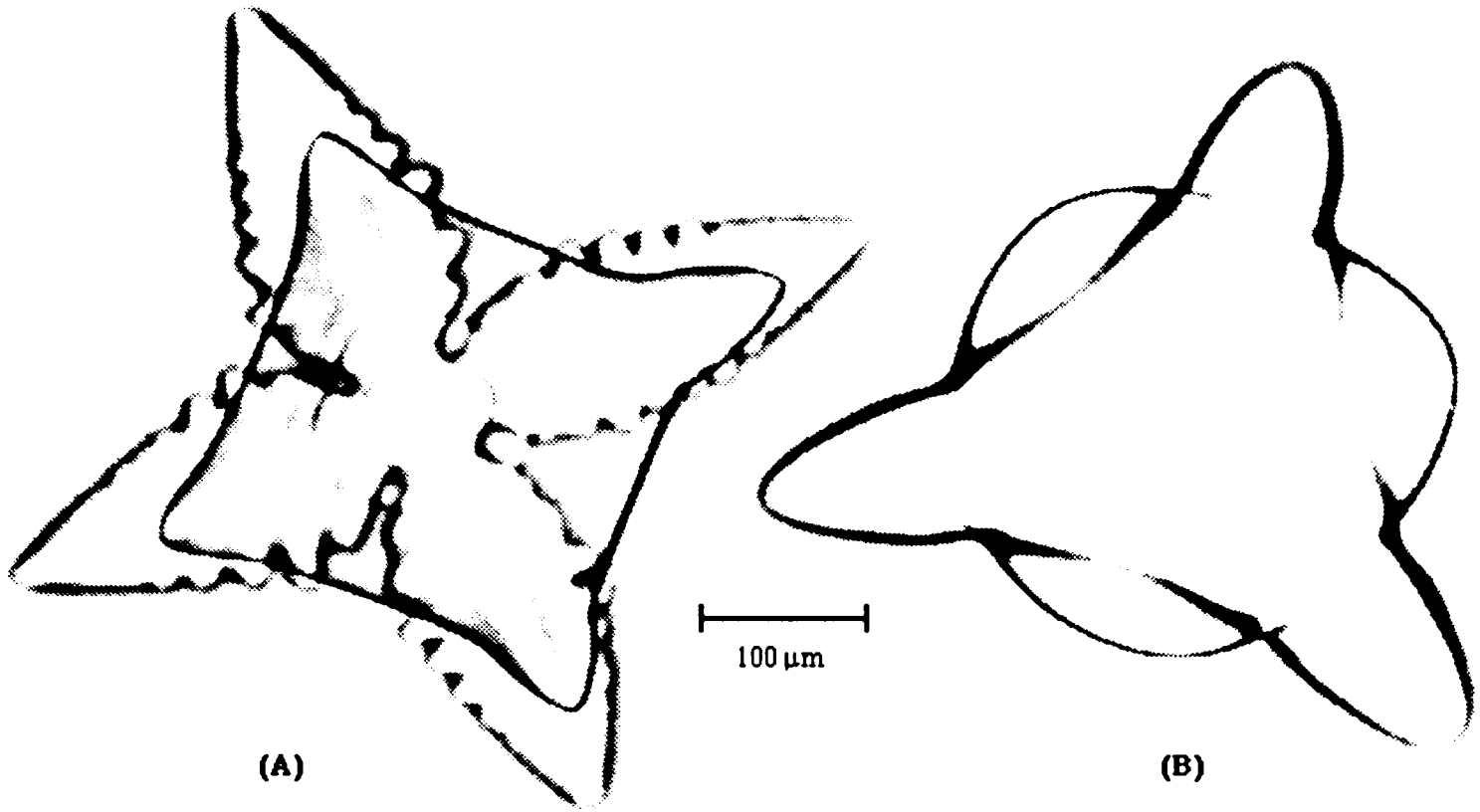

Fig. 27: Images of PVA crystals following a sudden temperature decrease. The fourfold symmetry of (A) indicates a crystal oriented with its [1,0,0] - axis normal to the image plane, while the three-fold symmetry in (B) indicates that the [1,1,1] axis is normal to the image.

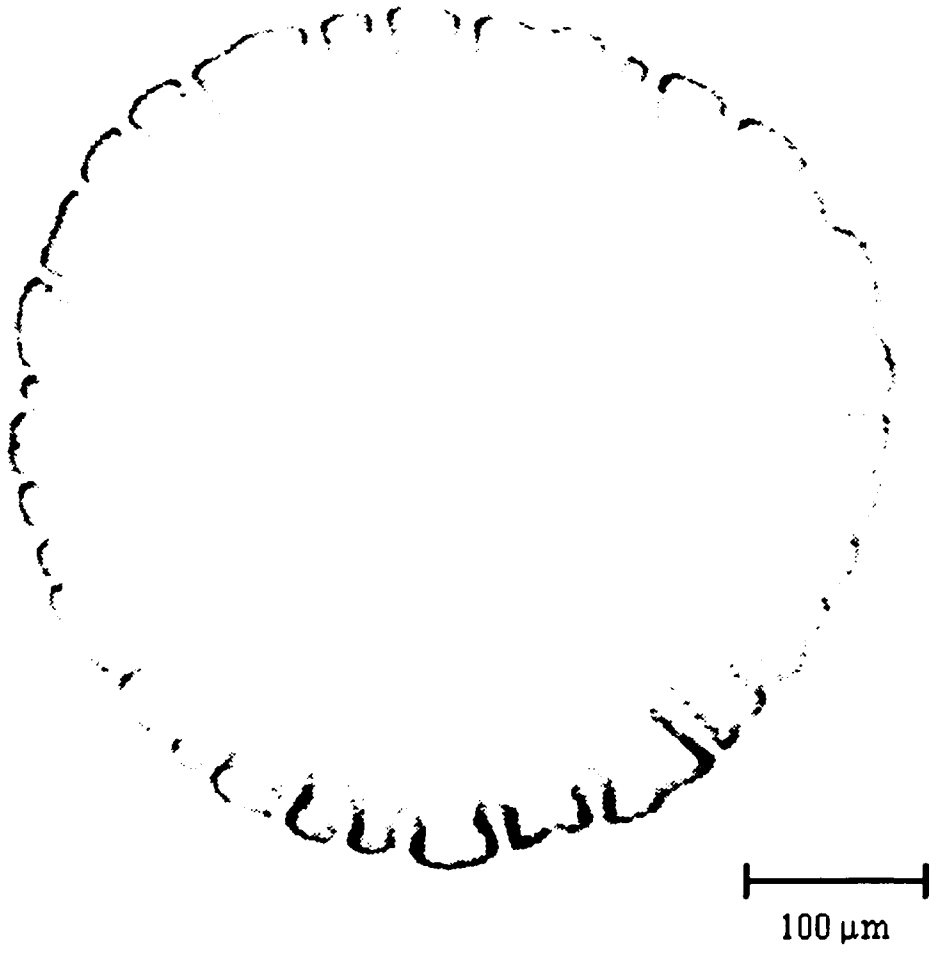

Fig. 28: Dense-branching morphology observed when undercooling SCN-seeds due to confinement-effect (see chapter 2.4.5). The seed orientation could not be determined from these images.

After checking the orientation we shrink the seed back to a radius of about 80 - 100 μm. At this size a small portion of the crystal is still attached to the bottom of the glass capillary. This seems to fix the crystal orientation inside the capillary. Crystals with larger radii have equilibration times which are too long. Crystals smaller than 50μm in diameter seem to detach from the glass and the orientation at the beginning and at the end of the experiment differ. Once the crystal is at the appropriate size for observation, it still tends to either grow or shrink slowly at fixed temperature. This is due to the fact that the critical gradient G_c needed to stabilize a 100 μm crystal is about one to two orders of magnitude larger than the largest gradients we can achieve in our sample thermostat (see Fig.29). We allow the crystal to slowly grow(shrink) until its size becomes too large(small) for observation, at which point we raise(lower) the temperature of the inner thermostat to reverse the direction. Using this method we can observe a crystal for several hours. We generally find that after at most 1 hour (for the binary system: 3 hours) the results of our shape measurements (for radii < 150μm) remain constant, independent of the size of the crystal, the growth speed, or the direction of growth. Images of SCN, PVA and PVA/ethanol crystal grains obtained this way are shown in Fig. 30.

5.2.5. Digital Image Analysis

The video images can be observed on the tv-monitor or the computer screen. Three different image analysis programs on our Macintosh computer capture and analyze video images: *QuickCapture*, a software package from Data Translation provided with their video board, *Enhance*

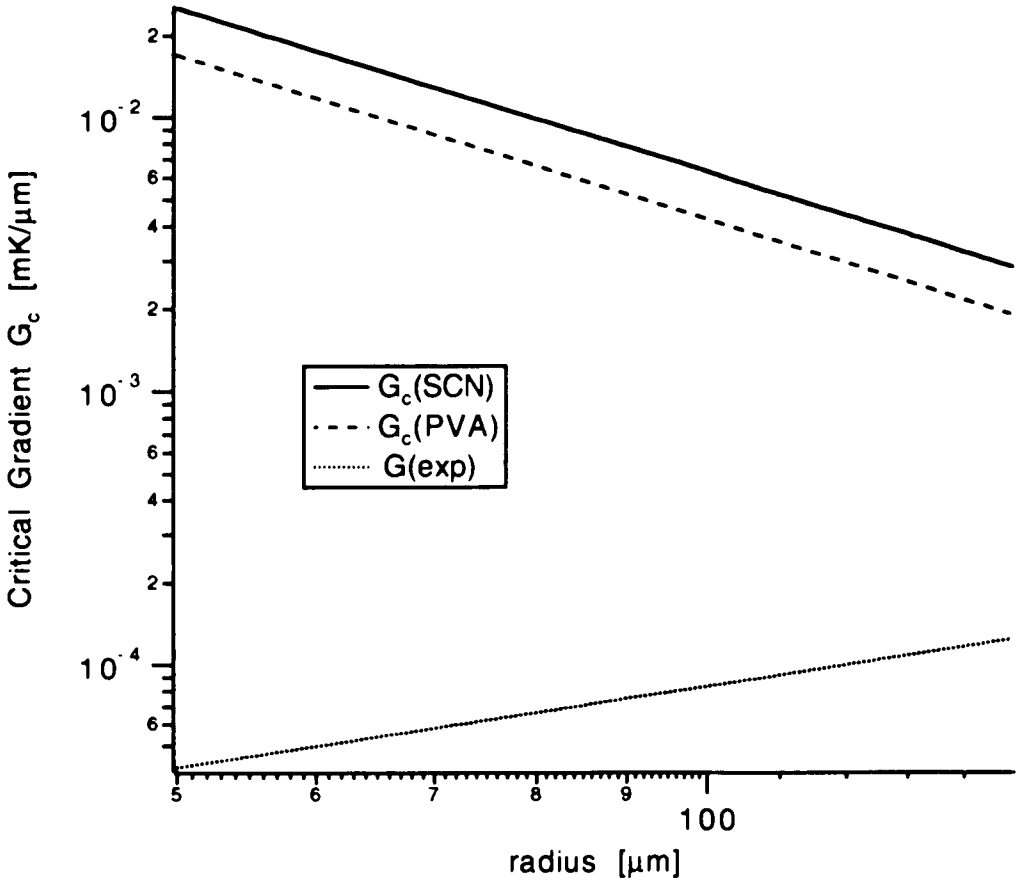

Fig. 29: Values of the critical temperature Gradient G_c for PVA and SCN compared with the measured temperature gradient (see Fig. 23) in our sample thermostat. The range of radii covers the experimentally observed crystal sizes.

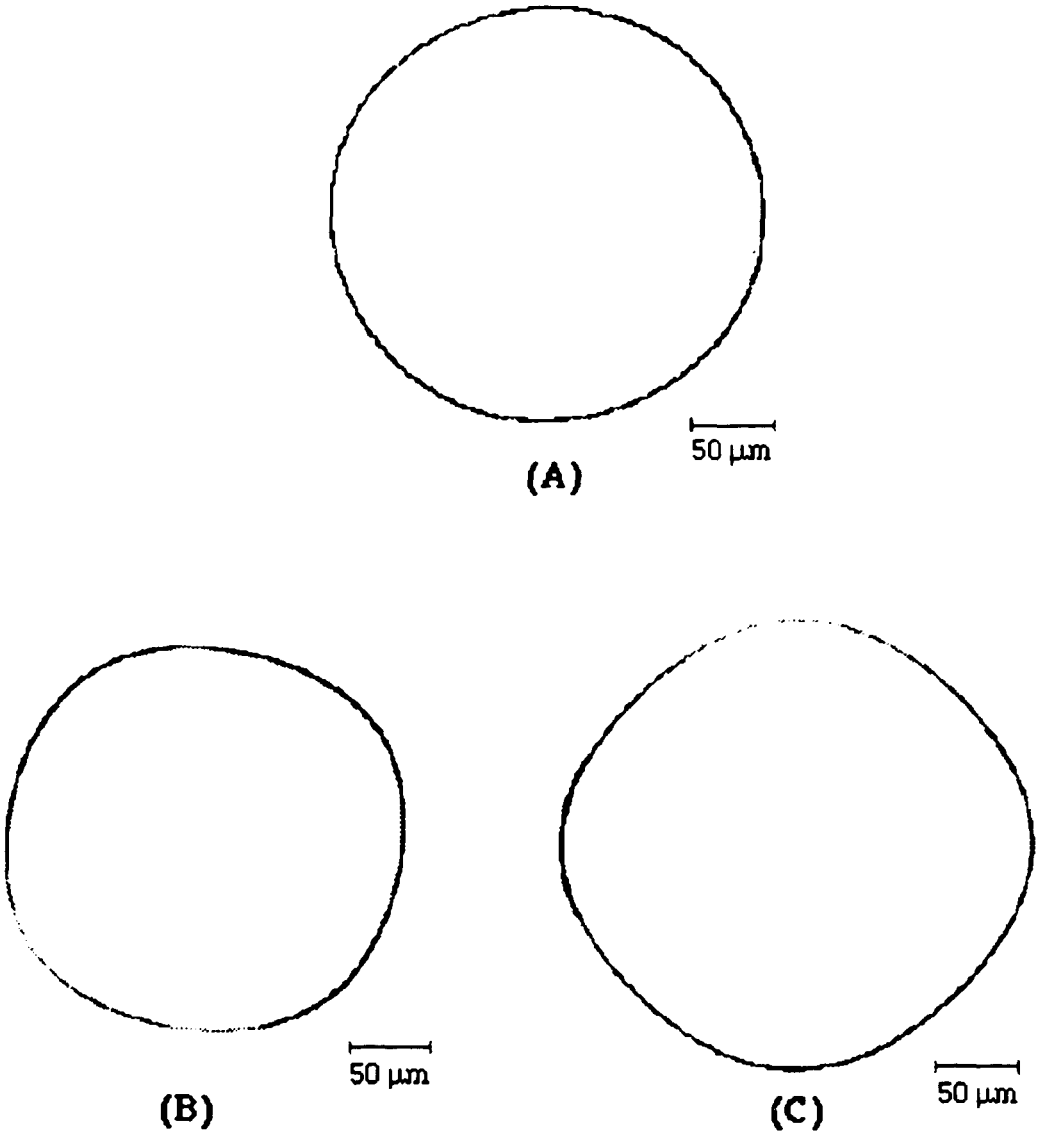

Fig. 30: Video images of crystals of (A) SCN (B) PVA and (C) PVA/ ethanol after thresholding the digitized images as described in the text. The larger asymmetry of PVA is visible in the images.

from Microfrontier and *Image*, a public domain program developed by the NIH. The latter two provide edge detection algorithms but the resulting interface coordinates are not accurate enough for our purposes.

The captured images consist of a rectangular array of 640 x 480 pixels, each pixel having an intensity resolution of 256 gray scales. The outline of the crystal interface appears as a thin dark line, 3 to 5 pixels wide, against a uniform lighter background. Figure 31 shows a 'landscape' view of the image intensity for a typical image. A radial intensity scan across such an interface is shown in Fig. 32 and we see that the profile is approximately parabolic. We adjust the light intensity of the microscope and the camera gain during the run so that we always obtain the above intensity profile across the interface.

We want to extract a set of polar coordinates (r_i, o_i) of the crystal -melt interface from these images. To do so we first need to find the center of the crystal and then determine the radial distance r_i of the interface for a given orientation o_i. As a first step we threshold the images: all pixels with intensity values close to the white background are disregarded and the preliminary center of the crystal is chosen to be the "center of mass" of all pixels above the threshold. From this preliminary center the interface is divided into angular slices of 2°-3° width. The intensity profile I(r) of all pixels within a given angular slice is fitted to a parabola (see Fig. 32). The distance of the maximum of this intensity parabola from the center is taken as the radial coordinate of the interface. Our choice of the maximum in intensity as the 'true' location of the interface is somewhat arbitrary. Since the width of a typical interface is much smaller than the mean radius of the corresponding crystal, a different choice would not alter our results significantly. We use the "center of mass" of these first-pass interface

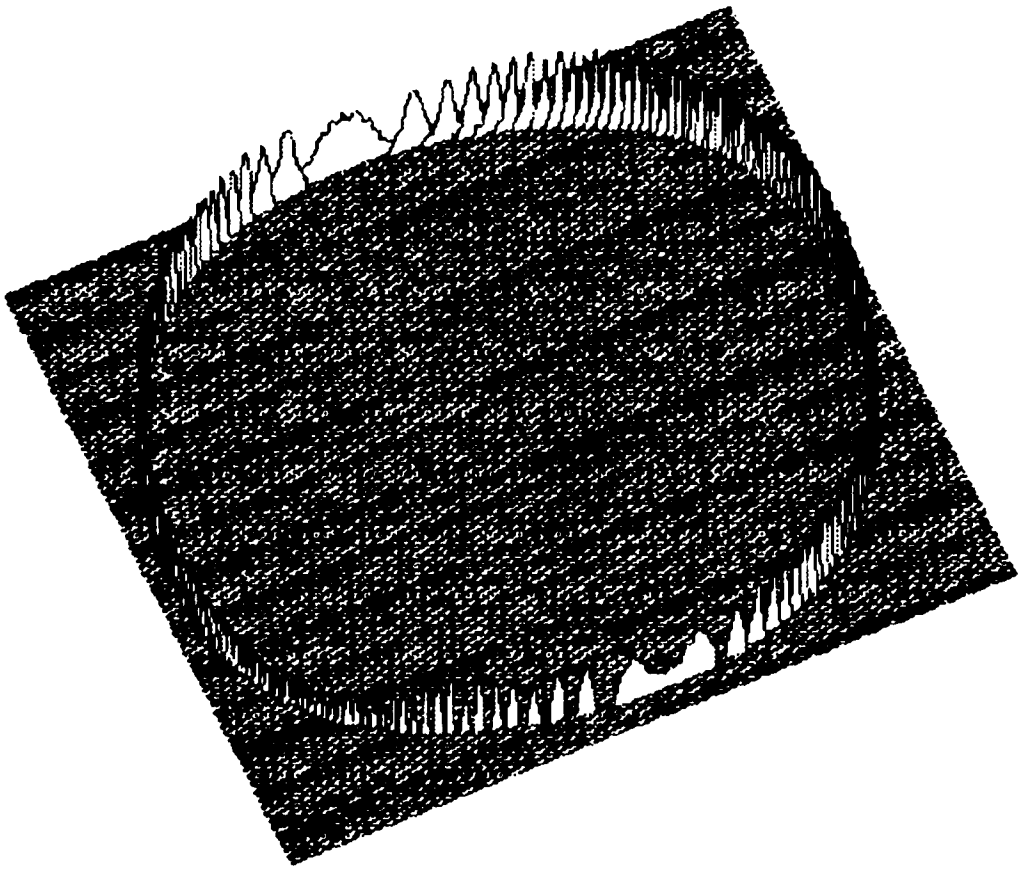

Fig. 31: Landscape view of the intensity profile of a typical image displayed in Fig.30. The crystal interface is clearly visible as the ridge of the intensity peaks.

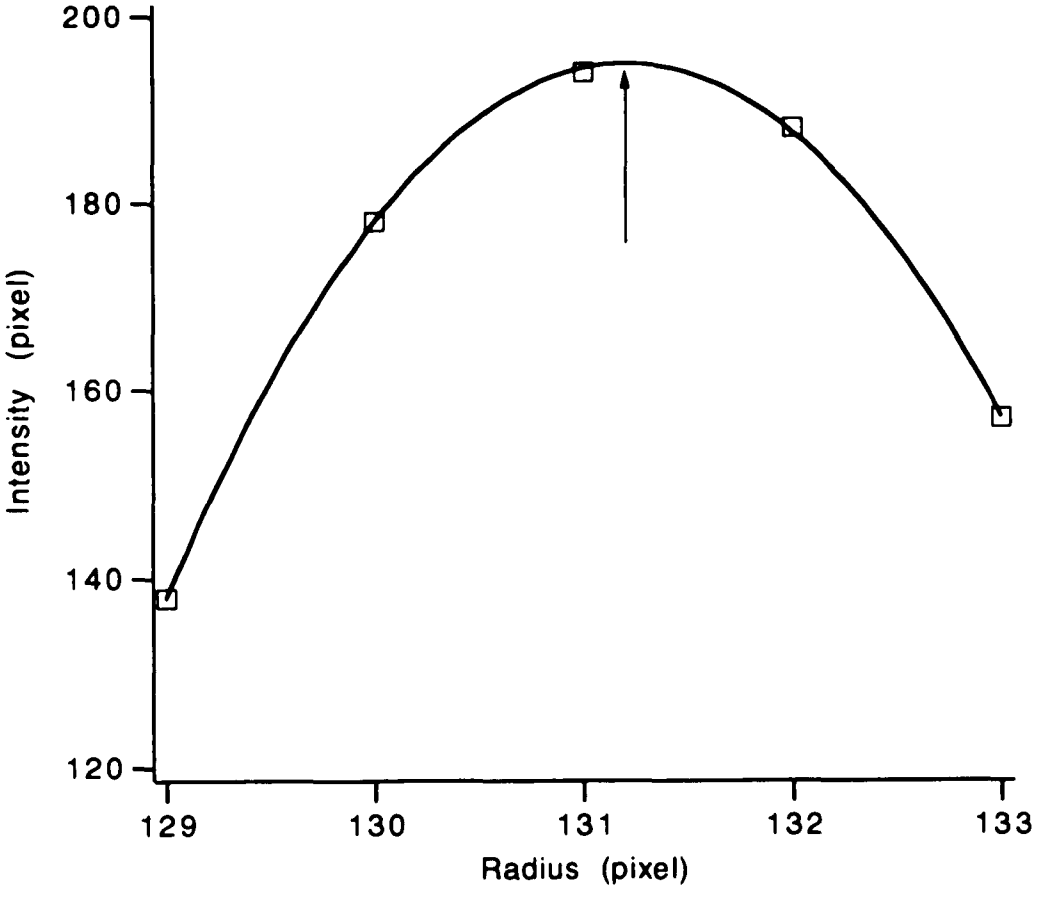

Fig. 32: Intensity profile across the image of a SCN crystal interface obtained as described in the text. The solid line is the fitted parabola, and the arrow shows the interpolated position of the center of the interface.

coordinates $[r_i(1),o_i(1)]$ to determine a more accurate location for the center. After running through this loop three times the corrections to the interface coordinates become negligible. In appendix C we discuss details of the programs written in MPW-C used to perform this task on our MacII computer. The resulting polar coordinates of the interface can be determined with an accuracy of about 0.2 pixels. This is about the same resolution Dougherty and Gollub [D4] achieved using similar interpolation techniques. The parabolic intensity profile together with our analysis procedure reduces the noisiness of the interface data in comparison to Dougherty and Gollub's data.

Typical plots of the extracted polar coordinates for the three materials are shown in Fig. 33. Note the clear fourfold shape anisotropy, but also the presence of a weaker twofold Fourier component, similar to observations of Dougherty and Gollub. [D3,D4].

5.3. Experimental Results

5.3.1. Fourier Analysis

Because of the twofold component of the experimental data (see Fig. 34) we Fourier analyze our data instead of fitting them directly to the shape of a crystal with purely four-fold surface tension anisotropy as given in Eq.(3.22). This allows us to look for higher order terms in the surface tension anisotropy as well. In the fit, we use the first eight Fourier modes of the discrete cosine transform

$$r_i(o_i) = a_o + \Sigma\, a_j \cos(n\phi_i + \delta_j) \qquad (5.3)$$

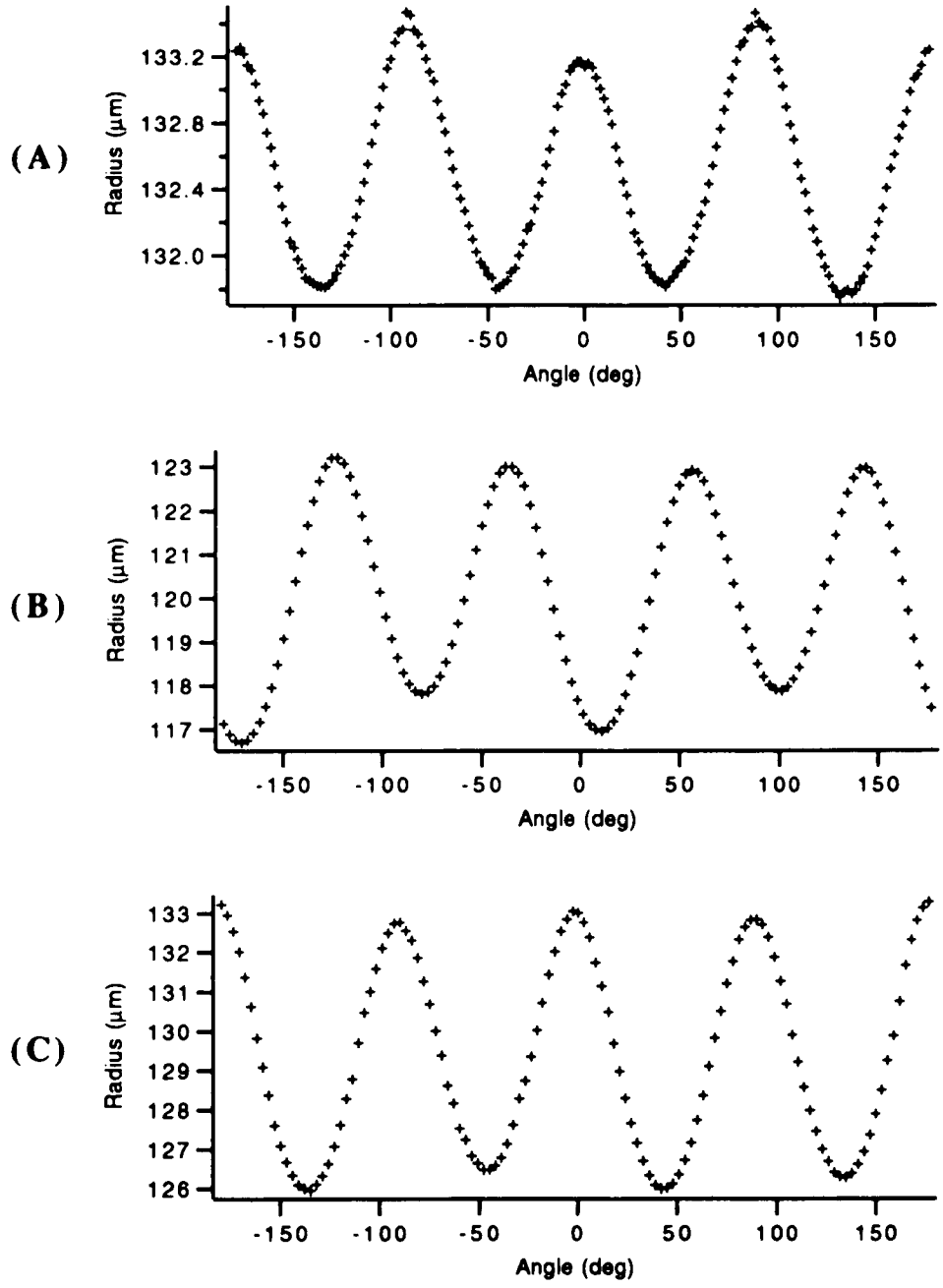

Fig. 33: Polar plot of the extracted interface coordinates for the (A) SCN (B) PVA and (C) PVA/ethanol crystal shown in Fig. 30.

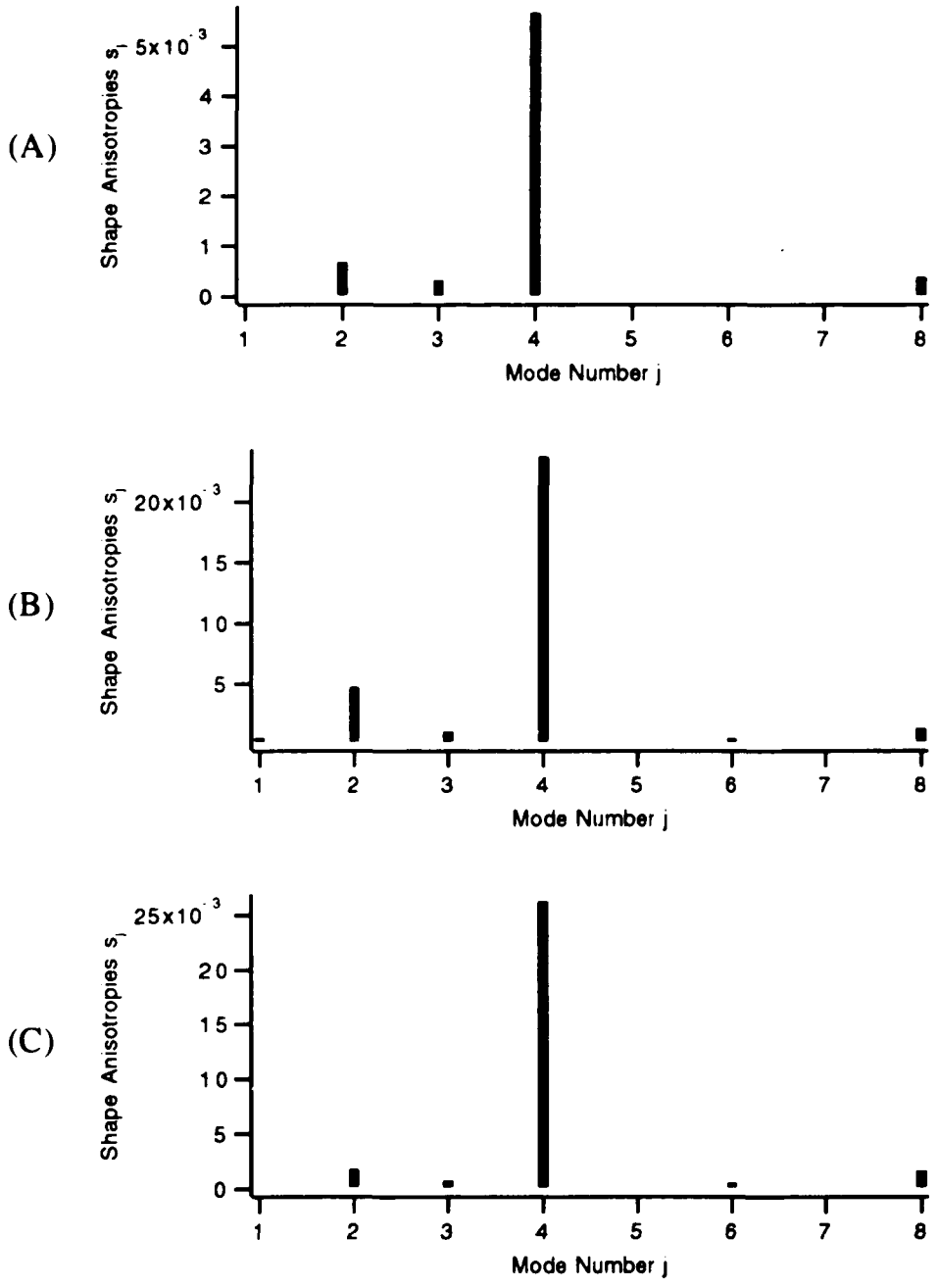

Fig. 34: Shape anisotropy coefficients s_j for the (A) SCN (B) PVA and (C) PVA/ethanol interfaces of Fig. 33

where the $r_i(o_i)$, i=1,..N are the discrete interface coordinates, a_j is the amplitude of the j-th mode and δ_j is the corresponding phase angle. The Fourier amplitudes a_j and the shape anisotropies s_j introduced in Eq. (3.29) are related by $s_j = a_j/a_o$, for $j \geq 1$. The shape anisotropies derived from Fourier-analyzing the three interfaces of Fig. 33 are shown in Fig. 34. Only the j=2,3,4,6 and j=8 shape anisotropies have measurable amplitudes after the crystal has reached equilibrium. All observed modes are consistent with the shape of a three-dimensional crystal with cubic symmetric surface tension when seen from different orientations.

At the beginning of each experiment the j=2 mode is dominant but it decays to values well below the j=4 amplitude. After this initial equilibration period the j=2 mode tends to fluctuate strongly around its mean.The four-fold component, in contrast, stays remarkably stable (see Fig.35). Besides the j=2 and j=4 modes only the j=8 mode shows sizeable values. As discussed in chapter 3.2.5., an eight-fold shape anisotropy component develops even for a crystal with purely four-fold surface tension anisotropy. Its presence can therefore not automatically be interpreted as sign of an underlying eight-fold surface tension anisotropy. Since for both materials the size of the eight-fold mode is at the limit of our experimental resolution we can only obtain an upper limit on any intrinsic eight-fold component of the surface tension anisotropy. We do so by subtracting from the experimentally observed value of s_8 the contribution due to the anharmonicity in equilibrium shape shown in Fig. 17.

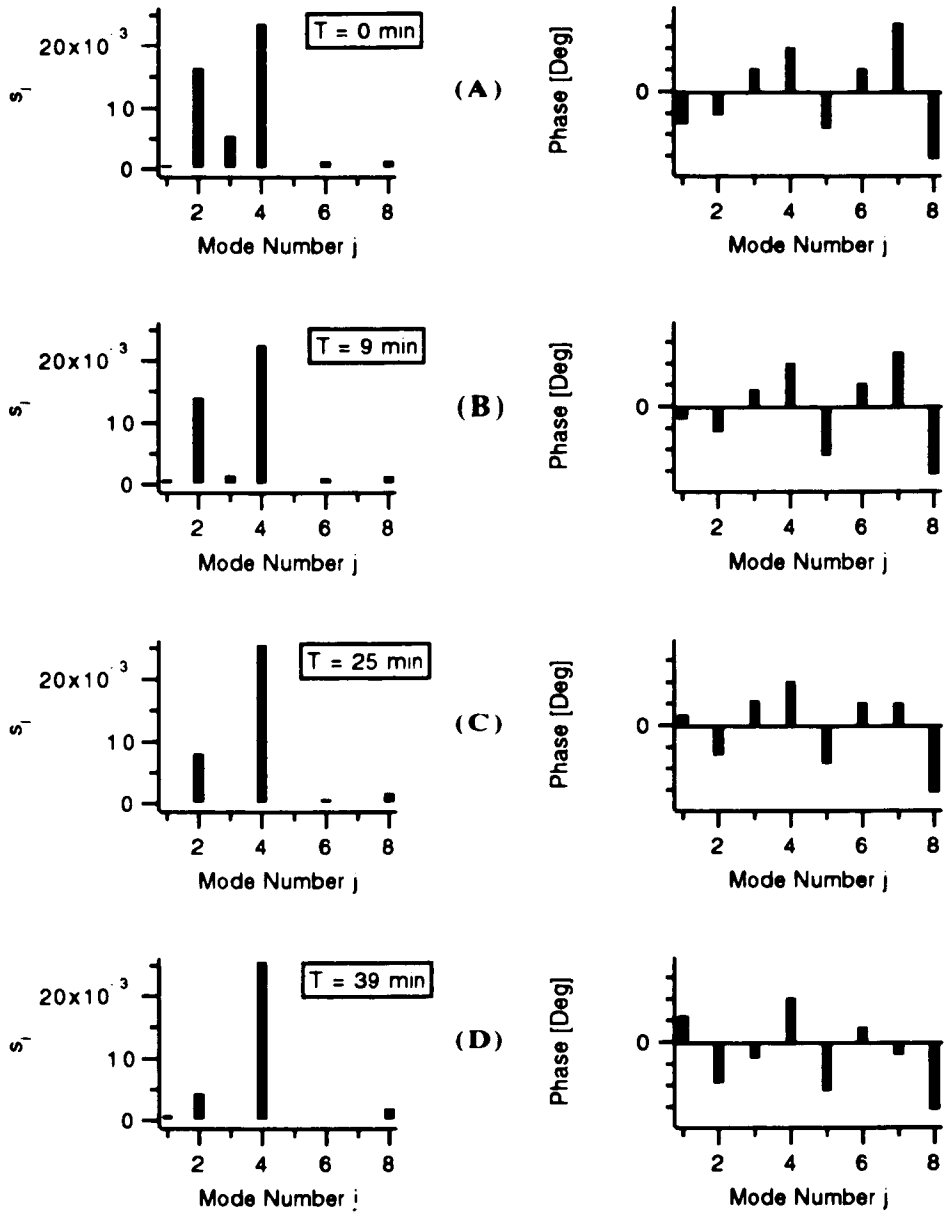

Fig. 35: Amplitude and phase of the shape anisotropies s_j of a PVA crystal during the early stages of equilibration. The spectra shown are for images taken (A) 0 (B) 9 (C) 25 and (D) 39 minutes after the seed was first established. Note the clear decay of the twofold component with time.Furthermore notice the steadiness of the four-fold and eight-fold phases while all others change noticeably.

5.3.2. Effects of Crystal Orientation

The measured shape anisotropies s_4 vary noticeably from run to run. In table 4 we've summarized results from several successful runs on all three systems. As mentioned above, we try to check the orientation of our seeds by making them go unstable and observing the orientation of the resulting dendritic branches as shown in Fig. 27. For seeds oriented close to the [100]-direction the value of the four-fold component in PVA is considerably larger than for seeds oriented along [111]. The value of s_4 changes with orientation from 2.4 to 1.4%. This ratio is roughly equal to $1/\sqrt{3}$ and therefore consistent with changes due to orientation. We therefore select the largest observed value of s_4 even in SCN where we could not determine the orientation. These values are listed in Table 4 as well. The size of the error bars on our final results accounts for the uncertainty in orientation. The results of a single run give much tighter error limits, typically less than 0.05% .

When looking at Fig. 21.b and 21.c, we can see that the observed Fourier amplitudes of a given projection should be related to the orientation of the seed with respect to the observer. In particular, the j=2,3, and j=6 mode should help to determine the orientation. In our experiments, however, these modes are not stable enough (particularly j=2) and too small (particularly j=3 and j=6) to derive the seed orientation.

5.3.3. Effect of the Temperature Gradient

In chapter 3.3 we discussed the effect of a radially symmetric temperature gradient on the observed crystal shape anisotropy and derived

the scaling relationship Eq. (3.36). Using the material parameters for SCN and PVA listed in table 2 we obtain for the critical gradient (Eq. 3.37)

SCN: $G_c = 63 / R^2$ [mK/μm] (5.4.a)

PVA: $G_c = 42 / R^2$ [mK/μm] (5.4.b)

where the crystal radius R is in units of μm. The parabolic fit through the temperature profile shown in Fig. 23 yields for the temperature gradient in our set-up in the range of $0< R< 5mm$

$$G(r) = 8.18 \times 10^{-7} R \quad [mK/\mu m] \qquad (5.5)$$

where R is in units of μm. Both functions are plotted in Fig. 29 for the experimentally interesting range of radii. Clearly, the temperature gradient in our set-up is at least an order of magnitude smaller than G_c. Under these circumstances, the values of the shape anisotropy s_4 are identical to the surface tension anisotropy ε_4.

5.3.4. Influence of Experimental Constraints on the Results

The diameter of our seed crystals is comparable to the height of our sample capillary (200μm). As already mentioned, this helps to keep the orientation of the crystal constant throughout the duration of the experiment. To assure ourselves that the presence of the capillary walls do not alter the crystal shape we change the diameter of our crystal from above to well below the height of the capillary. Particularly for small radii, the crystal usually detaches from the glass surfaces completely and floats freely in the melt. We observe no noticeable change in the shape anisotropy due to the crystal radius.

Another consideration is the time period over which the crystal is allowed to reach its equilibrium shape. For pure melts we find that after an

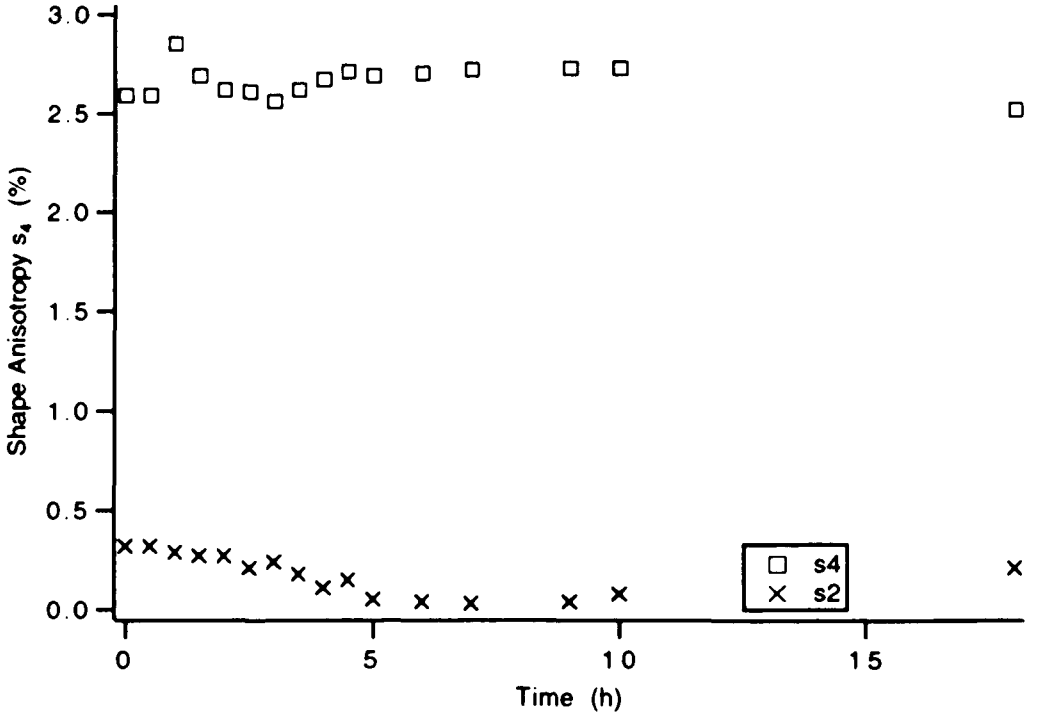

Fig. 36: Time-dependence of the j=2 and j=4 shape anisotropies during an experimental run with the PVA/ethanol mixture.

initial period of about one hour the crystals reach a shape whose Fourier modes do not change anymore over the course of several hours. In the case of the binary PVA/1% ethanol sample the equilibration period was closer to 3 hours. We have observed some PVA/Eth. crystals for several days but noticed no further change in shape anisotropy with time. A plot of the time dependence of such a crystal over a time period of 18 hours is shown in Fig. 36.

Finally, our crystals are slowly growing or shrinking during the course of the experiment (several μm/hour). For this range of speeds no dependence of the shape anisotropy on magnitude or direction of growth speed was detectable.

6. Discussion and Conclusion

6.1. Summary of the Results

In table 4 we summarize the values found for the surface tension anisotropies of the three systems studied. As we can see, the crystals clearly show four-fold surface tension anisotropy as expected from their symmetry. Eight-fold components, allowed by crystal symmetry, are much smaller and difficult to measure. Estimates of their magnitude are provided as well. Even small eight-fold components can have big effects on the predicted values of σ^*_{th}, since their amplitude is multiplied by a factor $8^2-1=63$ in the Gibbs-Thompson relation entering the steady-state equation (2.51). This multiplication factor of the n=8 mode is roughly four times larger than the factor $4^2-1 = 15$ for the n=4 mode. The value of the eight-fold symmetry in SCN might therefore be significant.

6.2. Pure versus Binary Samples

Studying pure PVA and a binary mixture of PVA/ 1% ethanol was meant to test the influence of sample purity on surface tension anisotropy. We chose the same systems used by Glicksman and Dougherty (see table 3) in order to make contact with their results. Our measurements showed no detectable difference in the surface tension anisotropy between the two samples. This is not too surprising since PVA has a microscopically rough crystal-melt interface which can more easily accommodate impurities than a smooth, faceted crystal surface [D3]. The value for the surface tension anisotropy ε_4 of 2.5±0.2% for pure PVA and 2.6%±0.2 for PVA/1%

ethanol, however, is about two times smaller than the value found by Glicksman and Singh [G5] and is about four times larger than Dougherty's value [D3]. There are several possible explanations for the observed differences. We already discussed the problems of using liquid inclusions to measure equilibrium shapes, as used by Glicksman in PVA. Beyond this, the continued presence of the two-fold shape distortion can affect the results when using Eq. (4.1) to measure ε_4. Sample purity might also play a role since Glicksman does use material of yet higher purity. In his experiments, however, droplets can only form in regions of increased impurity content. Our residual impurity content seems therefore an unlikely explanation for the difference in results. The discrepancy with Dougherty's result is surprising since we used very similar methods to his. The most likely reason for the disagreement is the presence of larger temperature gradients in his set-up. Another difference between the experiments is the image lighting. His observed step-function intensity profile across the crystal melt interface is a sign of a narrow band-width and steep gain setting on his camera (see e.g. Fig.1 in ref. [D3]). Tracking the edge of this intensity profile could make the interface appear more isotropic. Orientation effects are another candidate. Neither we nor Dougherty have a direct measure of the orientation of the crystals. Checking the orientation of dendritic arms emerging from the crystal before and after each run (see section 5.3.2.) we found the orientation of the crystal to be stable as long as the seed was large enough to be pinned by the glass surface. Dougherty checked the orientation similarly by melting a previously grown dendrite. However, his crystals are inside a much larger cell so that the orientation could have changed during the run.

6.3. Comparison with Microscopic Solvability Theory

The main objective of this study was to quantitatively test microscopic solvability theory. In chapter 2.4.4. we stressed the central role the dependence of σ^* on the anisotropy parameter α plays as a test of MST. We are now in a position to make this comparison. In table 5 we have listed the experimentally obtained values σ^*_{exp} together with the theoretical predictions of MST. In order to compare values of σ^*_{th} deduced from measurements of the surface tension anisotropy (via the theoretical results displayed in Fig. 9) with σ^*_{exp} several factors must be considered.

(1) The relation between σ^*_{th} and α depends somewhat on the peclet number p as illustrated by the results of Barbieri and Langer [B15] for p=0 and p=0.25 in Fig. 9. We have therefore included the range of the Peclet number for each determination of σ^*_{exp} in table 5. Since for all the measurements $p << 0.25$, we used the numerical results obtained for small p to find σ^*_{th}.

(2). The theoretical results shown in Fig. 9 are for the symmetric model in which the asymmetry parameter $\mu = D_S C_S / D_l C_l = 1$. We have to use Barbieri and Langer's Eq. (2.56) to obtain the values of σ^*_{th} applicable to the specific system. Since, in the case of chemical diffusion, experimental values of D_S are generally not available, we have followed the conventional procedure of letting $\mu=0$ for binary mixtures or solutions (one-sided model) where chemical diffusion dominates. For pure materials (symmetric model) where growth is controlled by thermal diffusion, we used $\mu=1$ whenever experimental values of μ were unavailable.

Table 5 clearly illustrates that the values of σ^*_{th} deduced from anisotropy measurements and σ^*_{exp} determined from observations of dendritic growth differ significantly for both SCN and PVA, by a factor of approximately 2 and in opposite directions. These discrepancies seem well beyond experimental errors, although the reported values of σ^*_{exp} for SCN and PVA include no error estimates. In Fig. 37 the experimental results are graphically displayed versus their theoretical predictions following a suggestion of J. Gollub. The deviations from the theoretical predictions of MST are well beyond reported experimental errors. We note that only for the solution growth of HET do σ^*_{exp} and σ^*_{th} appear to agree. For NH_4Br, the results of Doughtery [D3] agree with MST but Maurer et. al. [M9] report much larger values for σ^*_{exp}. (The ice result cannot be considered significant in view of the preliminary nature of the measurement of ε_6 [K13]).

We are therefore led to the essential question of whether or not these discrepancies can be reconciled with the basic approach of MST. One possible answer is the uncertainty in experimental data and material parameters. As we can see, the disagreement between ours and Dougherty's values for ε_4 puts the result for PVA/Ethanol on different sides of the theoretical curve, and both times out of its reach.

Assuming that the discrepancies are real and are not produced by experimental artifacts, there remain several possible ways in which the MST predictions might be modified.

First, the three-dimensional predictions shown in Fig. 9 assume axi-symmetric dendrites while real 3-d dendrites exhibit pronounced anisotropy around their axes. Preliminary results indicate, however, that deviations of σ^*_{th} from the axisymmetric values given here are small [K5].

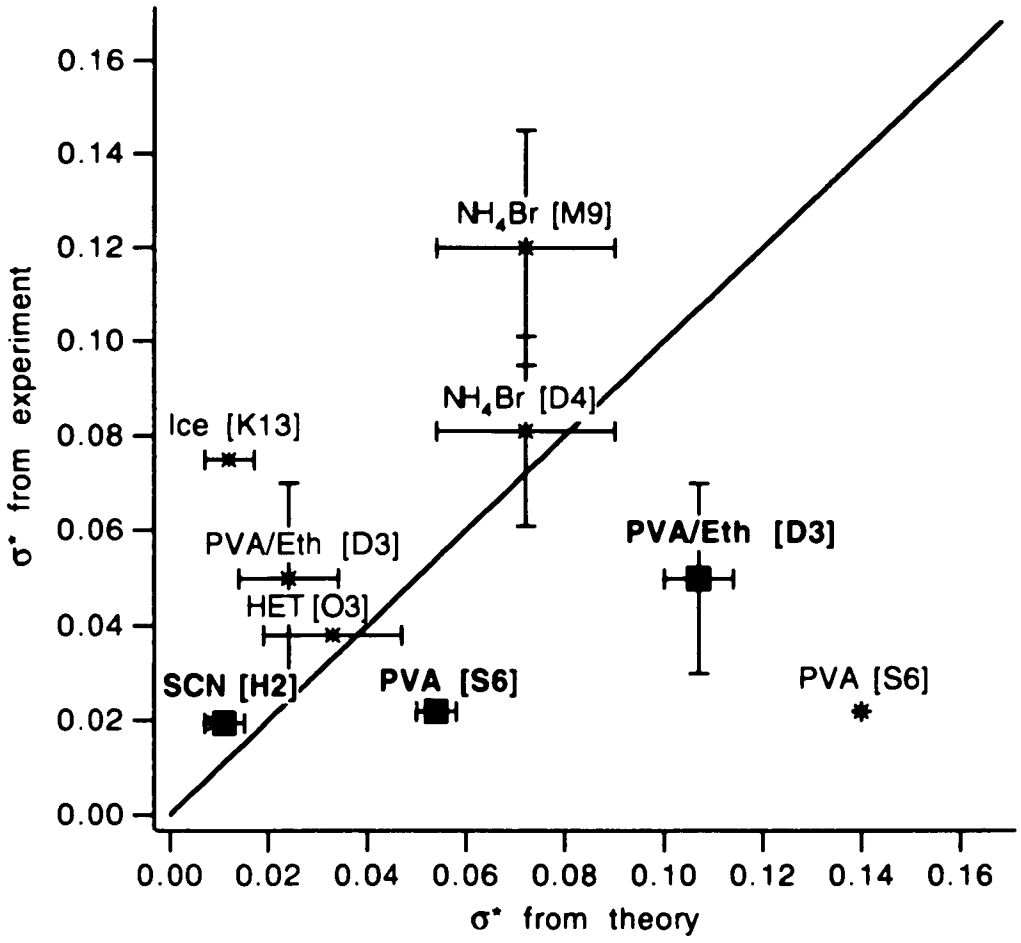

Fig.37: Plot of σ^*_{exp} versus σ^*_{theo}. Values of σ^*_{exp} are based on experimental measurements of v and ρ, while the results of σ^*_{th} are derived from measured surface tension anisotropies. Crosses are data points from previous anisotropy measurements, while black squares are predictions based on our anisotropy values. Whenever available, error bars for both σ^*_{exp} and σ^*_{th} are included. Errors in σ^*_{exp} are due to the uncertainty in v and ρ, while the errors in σ^*_{th} are based on the errors in surface tension anisotropy. References on the data points refer to the value of σ^*_{exp}. References to the anisotropy- and σ^*_{th} values can be found in table 5. The straight line, indicating perfect agreement with MST, is given as a guide to the eye.

Still, for ice dendrites the deviations from axisymmetric shape are so pronounced [K13] that our predictions seem inappropriate.

Second, since the dendritic growth experiments summarized in Table 5 were all performed (necessarily) with nonzero growth velocities, the values of σ^*_{exp} they produce must take kinetic effects into account which should be included in the comparison. But again, the deviations are expected to be small for the range of peclet numbers used in experiments.

Third, we note that the analysis underlying the MST predictions of Fig. 9 assumes a single nearly parabolic needle crystal without sidebranches, other neighboring dendrites, or boundaries. The morphological transition for growth in a restricitve channel geometry as predicted by Brener and Kessler (see chapter 2.4.5), and observed by Oswald et al [O4] can modify the results significantly.

Finally, H. Levine and E. Brener have noted that MST predictions based on the usual approximation for the surface tension in Eq. (2.51) may be significantly modified by the presence of higher harmonics. For our determinations of s_4 and s_8 for SCN and PVA we have estimated ε_8 and $\alpha_8=63\varepsilon_8$ as: $\alpha_8= +0.016\pm0.002$ for SCN and $\alpha_8= -0.057\pm0.013$ for PVA. By including both α_4 and α_8 in a 2-d numerical MST computation (program of M. Ben Amar), Brener found that σ^*_{th} for SCN is increased by ~50%, with a much smaller correction for PVA [B23].

Given the serious disagreement of theory and experiment, however, we also have to consider the possibility that an essential ingredient of the selection mechanism is still unaccounted for by microscopic solvability. It would certainly not be the first time that the selection problem took an unexpected new turn. Further theoretical and experimental studies are

therefore necessary to eliminate the uncertainty prevailing at the present stage.

Appendix A

Derivation of Relation (3.19) in Section 3.2.2.

In Eq. (3.19) of chapter 3.2.2. we asserted that

$$\gamma_{\theta\theta} = \left(1 + y'^2\right)\left[2y'\frac{d\gamma}{dy'} + \left(1 + y'^2\right)\frac{d^2\gamma}{dy'^2}\right] \qquad (A.1)$$

where $\gamma_{\theta\theta}$ is the second derivative of the surface tension with respect to the angle θ between the normal to the interface and the x-axis. To derive relation (A.1) look at Fig. A1 below which shows a part of the interface.

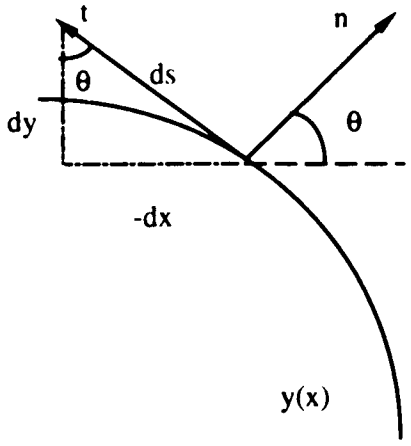

figure A.1 : relation between y' and normal angle θ

We can see that the normal angle θ is related to the derivative y' :

$$y' = \cot\theta \quad \Leftrightarrow \quad \theta = \operatorname{arccot} y' \qquad (A.2)$$

Now we apply the chain rule to relate the derivatives with respect to y' to those with respect to θ:

$$\frac{\partial}{\partial\theta} = \frac{\partial y'}{\partial\theta}\frac{\partial}{\partial y'} \qquad (A.3)$$

$$\frac{\partial^2}{\partial\theta^2} = \frac{\partial}{\partial\theta}\left(\frac{\partial y'}{\partial\theta}\frac{\partial}{\partial y'}\right) = \frac{\partial^2 y'}{\partial\theta^2}\frac{\partial}{\partial y'} + \left(\frac{\partial y'}{\partial\theta}\right)^2\frac{\partial^2}{\partial y'^2} \qquad (A.4)$$

We can calculate the derivatives of y' with respect to the angle θ by using relation (A.4)

$$\frac{\partial y'}{\partial \theta} = \frac{\partial}{\partial \theta}\cot\theta = -\left[1+\cot^2\theta\right] = -\left[1+y'^2\right] \qquad (A.5)$$

$$\frac{\partial^2 y'}{\partial \theta^2} = 2\cot\theta\left[1+\cot^2\theta\right] = 2y'\left[1+y'^2\right] \qquad (A.6)$$

The right hand side of (A.4) can now be rewritten in terms of y' only :

$$\frac{\partial^2}{\partial \theta^2} = \left(1+y'^2\right)\left[2y'\frac{\partial}{\partial y'} + \left(1+y'^2\right)\frac{\partial^2}{\partial y'^2}\right] \qquad (A.7)$$

This completes the proof of identity (A.1)

Appendix B

Numerical Relaxation Method for Crystal Shape in Temperature Field

B.1 Transforming the ODE's into Finite Difference Equations

The equations governing the shape of a two-dimensional crystal subjected to a radially symmetric, linear temperature field were introduced in section 3.3.2. They are

$$\frac{dx}{d\theta} = -\frac{T_m}{T_m - T_o - Gr} \frac{\gamma + \gamma_{\theta\theta}}{L} \sin\theta \qquad \text{(B.1a)}$$

$$\frac{dy}{d\theta} = \frac{T_m}{T_m - T_o - Gr} \frac{\gamma + \gamma_{\theta\theta}}{L} \cos\theta \qquad \text{(B.1b)}$$

where x,y are the interface coordinates, θ is the angle of the normal to the interface with the x-axis, T_m is the melting temperature and L the latent heat of the substance, $T(r)=T_o + Gr$ is the externally imposed temperature field introduced in Eq. (3.33), and γ is the orientation-dependent surface tension anisotropy. In contrast to the case of uniform undercooling, the r.h.s of (B.1) is a function of the interface coordinates (x,y) through the presence of the temperature field T(r).

We solved these two coupled ODE's numerically by a relaxation method for two-point boundary value problems as described in Press et al [P4]. We need to convert the ODE's of (B.1) into finite difference equations (FDE's). This is not a unique transformation and we choose

$$\frac{x_k - x_{k-1}}{\theta_k - \theta_{k-1}} = -\frac{g(\theta_{k,k-1})}{U(r_{k,k-1})} \sin(\theta_{k,k-1}) \qquad \text{(B.2a)}$$

$$\frac{y_k - y_{k-1}}{\theta_k - \theta_{k-1}} = \frac{g(\theta_{k,k-1})}{U(r_{k,k-1})}\cos(\theta_{k,k-1}) \qquad \text{(B.2b)}$$

with $U(r) = T_m - T_o - G\,r = T_b\,[\,1 - r / R_{max}]$ (B.3)

where $T_b = (T_m - T_o)$ is the undercooling at r=0 and $R_{max} = T_b/G$ is the radial distance at which U(r)=0. Furthermore we introduced

$$g(\theta) = T_m\,(\gamma + \gamma_{\theta\theta})\,/\,L \qquad \text{(B.4)}$$

$$\theta_{k,k-1} = 1/2\,(\theta_k + \theta_{k-1}) \qquad \text{(B.5)}$$

$$r_{k,k-1} = [\,(1/2(x_k+x_{k-1}))^2 + (1/2(y_k+y_{k-1}))^2\,]^{1/2} \qquad \text{(B.6)}$$

The equations (B.2) are a set of algebraic equations coupling the discrete interface points (x_k,y_k) with (x_{k-1},y_{k-1}). To make connection with the notation in ref. [P4], we rewrite the two FDE's (B.2) in the form

$$E_{1,k} \equiv x_k - x_{k-1} + \frac{A(\theta_{k,k-1})}{B(r_{k,k-1})}\sin(\theta_{k,k-1}) = 0 \qquad \text{(B.7a)}$$

$$E_{2,k} \equiv y_k - y_{k-1} - \frac{A(\theta_{k,k-1})}{B(r_{k,k-1})}\cos(\theta_{k,k-1}) = 0 \qquad \text{(B.7b)}$$

where $A(\theta_{k,k-1}) = (\theta_k-\theta_{k-1})\,g(\theta_{k,k-1})$ (B.8)

B.2 Outline of the Relaxation Algorithm

Now we can explain the basic idea of the relaxation algorithm. We start with a guess for the interface shape, represented by M discrete coordinates (x_k,y_k), k=2,...,M. We try to improve on this guessed solution by expanding the $E_{j,k}$'s, j=1,2 of (B.7) around small variations $(\Delta x_k,\Delta y_k)$ of the starting solution so that the $E_{j,k}$'s=0 for the corrected coordinates $(x_k+\Delta x_k,y_k+\Delta y_k)$

$$0= E_{j,k}(x_k+\Delta x_k, y_k+\Delta y_k, x_{k-1}+\Delta x_{k-1}, y_{k-1}+\Delta y_{k-1}) \approx E_{j,k}(x_k, y_k, x_{k-1}, y_{k-1}) +$$

$$\frac{\partial E_{j,k}}{\partial x_{k-1}}\Delta x_{k-1} + \frac{\partial E_{j,k}}{\partial y_{k-1}}\Delta y_{k-1} + \frac{\partial E_{j,k}}{\partial x_k}\Delta x_k + \frac{\partial E_{j,k}}{\partial y_k}\Delta y_k \qquad (B.9)$$

This leads to a set of 2x(M-1) equations for the interface corrections $(\Delta x_k, \Delta y_k)$ in the interior of the parameter range θ_k.

$$S_{j,1}\,\Delta x_{k-1} + S_{j,2}\,\Delta y_{k-1} + S_{j,3}\,\Delta x_k + S_{j,4}\,\Delta y_k = E_{j,k} \qquad (B.10)$$

where $$S_{j,1} = \frac{\partial E_{j,k}}{\partial x_{k-1}},\ S_{j,2} = \frac{\partial E_{j,k}}{\partial y_{k-1}},\ S_{j,3} = \frac{\partial E_{j,k}}{\partial x_k},\ S_{j,4} = \frac{\partial E_{j,k}}{\partial y_k} \qquad (B.11)$$

j=1,2, and k=2,...,M. This set of equations is the heart of the numerical algorithm. They will eventually "relax" our starting guess to the desired solution. To evaluate the partial derivatives appearing in (B.11) we need

$$\partial_{x,y} U^{-1}(r_{k,k-1}) = -\frac{\partial_{x,y} U(r_{k,k-1})}{U^2(r_{k,k-1})} = \frac{T_b \partial_{x,y} r_{k,k-1}}{R_x T_b^2 [1 - r_{k,k-1}/R_{max}]^2} \qquad (B.12)$$

where $\partial_{x,y}$ stands for any of the partial derivatives appearing in Eq.(B.11).

Evaluating $$\partial_x r_{k,k-1} = (x_k + x_{k-1})/4\, r_{k,k-1} \qquad (B.13a)$$

$$\partial_y r_{k,k-1} = (y_k + y_{k-1})/4\, r_{k,k-1} \qquad (B.13b)$$

we obtain $$\partial_x U^{-1}(r_{k,k-1}) = \frac{1}{4}\frac{(x_k + x_{k-1})}{R_{max} T_b r_{k,k-1}[1 - r_{k,k-1}/R_{max}]^2} \qquad (B.14a)$$

and $$\partial_y U^{-1}(r_{k,k-1}) = \frac{1}{4}\frac{(y_k + y_{k-1})}{R_{max} T_b r_{k,k-1}[1 - r_{k,k-1}/R_{max}]^2} \qquad (B.14b)$$

where $\partial_x = \partial_{x_{k-1}}$ or ∂_{x_k} and $\partial_y = \partial_{y_{k-1}}$ or ∂_{y_k}.The resulting expressions for the $S_{j,k}$'s are

$$S_{1,1} = -1 + A(\theta_{k,k-1}) \sin(\theta_{k,k-1})\, \partial_x U^{-1}(r_{k,k-1}) \qquad (B.15a)$$

$$S_{1,2} = A(\theta_{k,k-1}) \sin(\theta_{k,k-1})\, \partial_x U^{-1}(r_{k,k-1}) \qquad (B.15b)$$

$$S_{1,3} = S_{1,1} + 2 \qquad (B.15c)$$

$$S_{1,4} = S_{1,2} \tag{B.15d}$$

and

$$S_{2,1} = -A(\theta_{k,k-1}) \cos(\theta_{k,k-1}) \, \partial_x U^{-1}(r_{k,k-1}) \tag{B.16a}$$

$$S_{2,2} = -1 - A(\theta_{k,k-1}) \cos(\theta_{k,k-1}) \, \partial_x U^{-1}(r_{k,k-1}) \tag{B.16b}$$

$$S_{2,3} = S_{2,1} \tag{B.16c}$$

$$S_{2,4} = S_{2,2} + 2 \tag{B.16d}$$

So far we only have 2x(M-1) equations for the 2xM interface corrections $(\Delta x_k, \Delta y_k)$. The remaining equations are provided by the two boundary conditions

B.3 Boundary Conditions

We are interested in crystals with four-fold symmetric surface tension of the form

$$\gamma(\theta) = \gamma_o [\, 1 + \varepsilon_4 \cos(4\theta) \,] \tag{B.17}$$

Due to the symmetry of $\gamma(\theta)$, we only need to solve (B.1) in the parameter range $\theta \in [0, \pi/4]$. The boundary conditions we impose are

$$y = 0 \qquad \text{for} \qquad \theta = 0 \tag{B.18a}$$

$$x = y \qquad \text{for} \qquad \theta = \pi/4 \tag{B.18b}$$

We have to enforce these boundary conditions at the end points k=1 and k=M . For k=1 Eq. (B.18a) yields

$$E_{1,1} = 0 , \qquad E_{2,1} = x_1 \tag{B.19}$$

and therefore

$$S_{1,1} = 0 , \qquad S_{1,2} = 0 \tag{B.20a}$$

$$S_{2,1} = 1 , \qquad S_{2,2} = 0 \tag{B.20b}$$

At k=M Eq. (B.18b) yields

$$E_{1,M+1} = x_M - y_M , \quad E_{2,M+1} = 0 \tag{B.21}$$

which gives $S_{1,1} = 1$ $S_{1,2} = -1$ (B.22a)

$S_{2,1} = 0$, $S_{2,2} = 0$ (B.22b)

Two conditions, (B.20a) and (B.22b), are trivial and will be dropped from the algorithm. This completes our set of 2xM equations.

B.4 Structure of the Computer Programs

Details on how the the relaxation algorithm is implemented numerically are discussed in ref. [P4]. The central part of the algorithm is the subroutine **solvde**. We have to provide a calling routine, which initializes all the necessary arrays and variables, calculates the starting guess for the interface shape, and calls **solvde**. This calling program is named **gradcrys**. **Solvde** also calls a subroutine to evaluate the Ej,k's and Sj,k's of Eq. (B.10). This subroutine has to be named **difeq**. Both problem specific programs, namely **gradcrys** and **difeq**, are presented on the following pages, together with detailed comments.

B.5 Listing of Computer Programs

```
#     program     :     gradcrys.r
#     written by  :     Martin Muschol
#     update      :     23 Feb 91
#     purpose     :     This is the main program of a whole set of
#                 programs to calculate the 'equilibrum shape'
#                 of a two-dimensional crystal with anisotropic
#                 surface tension sitting in a radially symmetric, linear
#                 temperature field of known shape. It is written in
#                 ratfor.
#
#     link to:          - solvde.f, red.f ,pinvs.f, bksub.f
#                             (ODE-solver  routines from Num.
#                             Recipices book)
#                       - difeq.r
#                             ( subroutine to evaluate the functions
#                             needed by the solvde-subroutine)
#     Variables:
#
#     (1)   Input parameters:

#     do          = γ*Tm / L in [ μm K] . Lumped material parameter.
#                 Value used here is for SCN. Fixed in data statement
#     y(1,1)      approximate starting radius of crystal in [μm]
#     eps         surface tension anisotropy ( decimal number)
#     grad        linear temperature gradient ( in [K/cm])
#     itmax       max. number of program iterations
#     nt          number of interface points in the interval θ ∈ [0,π/4]
#                 maximum: 200
#     name(1)     file containing the interface coordinates of the starting
#                 guess
#     name(2)     file containing interface coordinates of the solution
#
#     (2)   Further Variables:

#     y(2,200)    array containing the interface coordinates (xk,yk) with
#                 xk = y(1,k) and yk = y(2,k).
#     k           index of the interface point (xk,yk)
#     ne          number of equations (here=2)
#     s(2,5)      These are the central variables of the algoritm.
#                 s(j,5) j=1,2 and k=2,..,nt are the Ej,k's of Eq. (B.7a),
```

```
#                   while s(j,n) j=1,2,n=1,..,4 and k=2,....,nt are the partial
#                   derivatives introduced in Eq. (B.11)
#     t(201)        array containing the normal angles θk. Note that the
#                   program works with an array of equally spaced points
#                   in this parameter.
#     tmin,tmax     minimum,maximum value of θ. Here tmin = 0,
#                   tmax = π/4.
#     dt            = θk - θk-1. Spacing of normal angle
#     rad           mean radius of starting guess
#     delb          = Tb [K]. Undercooling at the coordinate origin r=0.
#     Rx            = Rmax (in μm). Radius at which the undercooling
#                   vanishes.
#     gc            critical gradient Gc = Tmγ /Lr2
#     conv          convergence criterion. If Σ(Δxk,Δyk)/scalv(j) < conv
#                   the the corrections to the previous interface coordinates
#                   are considered negligible and the program quits.
#     scalv(2)      Scaling factor of the two equations E1,k and E2,k in
#                   the above sum of corrections.
#     slowc         if Σ(Δxk,Δyk)/scalv(j) > slowc then the corrections are
#                   considered too large and the program only adds a
#                   fractions of the (Δxk,Δyk) to the previous interface
#                   coordinates.
#     percent       fraction of initial radius y(1,1). Used to determine conv.
#     angle(200), radius(200)          polar coordinates of the solution
#
#     The remaining variables are work arrays and set-up variables of the
#     subroutine solvde: They are: indexv(2), c(2,1,202), ne, nb, nci, ncj,
#     nck, nsi ,nsj. For a detailed description see: W.H. Press et al.,
#     Numerical Recipes, (Cambridge University Press, 1986) p588 f.
#
#*************************************************************#

      double precision   y(2,201),t(201),tmin,tmax,dt,rad,
                         conv,slowc,percent,scalv(2),s(2,5),c(2,1,202),
                         delb,Rx,do,eps,pi,grad
      real               angle(200),radius(200)
      integer            k,nt,indexv(2),itmax,ne,nb,nci,ncj,nck,nsi,nsj
      character*20       name(2)
      parameter    (pi = 3.1415926535898)
      common /input1/ do,eps,delb,Rx       # share with difeq.r subroutine
      common /input2/ tmin,tmax,t          # share with difeq.r
      data do/.0632/                       # = γ*Tm/L [μm K] !!!!!
```

```
      data tmin,scalv,ne,nb/0,2*1,2,1/       # set up some variables

      print *,'Enter the approximate starting radius (in μm)'
      read *,y(1,1)
      print *,'Enter the surface tension anisotropy eps'
      read *,eps

      gc    = do*(1+eps)/y(1,1)**2                  # gc = [K/um]
      print *,'Enter gradient of linear temp. field (K/cm)'
      read *,grad
      grad = grad/10000                             # convert to [K/um]

      Rx    = y(1,1)*(1+gc/grad)                    # determine Rmax
      delb  = do*(1+eps)/y(1,1)+grad*y(1,1)         # determine Tb
      print *,'Rx [um] = ',Rx
      print *,'delb [K] = ',delb

      percent = .001          # Set convergence to 1/1000 of full radius
      conv  = y(1,1)*percent
      slowc       = min(y(1,1)/40,Rx-y(1,1)) # corrections with r>Rmax
      print *,slowc                          # or y(1,1)/40 are reduced
      tmax  = tmin + 45
      print *,'Enter the maximum number of iteration'
      read *,itmax
      print *,'Enter the number of interface points (max = 200)'
      read *,nt
      print *,'Enter filename for initial guess '
      read *,name(1)
      print *,'Enter filename for final result'
      read *,name(2)
      open (1,file = name(1))
      open (2,file = name(2))

      tmax  = tmax*(pi/180)          # determine angles in
      tmin  = tmin*(pi/180)          # radian
      dt    = (tmax-tmin)/float(nt)  # get even spacing in θ
      nt    = nt +1                  # (# of mesh points) =
                                     # (1 + # of spacings)

# provide starting guess for interface (here: anisotropic solution with
# constant undercooling)

      rad   = y(1,1)
```

```
      for (k=1;k<=nt;k=k+1)
      {
            t(k)   = tmin+(k-1)*dt
            gamma      = 1.+eps*cos(4*(t(k)-tmin))
            delgam     = -4*eps*sin(4*(t(k)-tmin))
            y(1,k)     = rad*(gamma*cos(t(k))-delgam*sin(t(k)))
            y(2,k)     = rad*(gamma*sin(t(k))+delgam*cos(t(k)))
            angle(k)   = atan2(y(2,k),y(1,k))*180/pi
            radius(k)  = sqrt(y(1,k)**2+y(2,k)**2)
            write (1,*) angle(k),radius(k)
      }

#     Write the polar coordinates of the initial guess into the file name(1)
#     We use the symmetry of the figures to generate the coordinates in
#     the range θ = (0,2π)

      for (k=1;k<nt;k=k+1)    write (1,*) 90-angle(nt-k),radius(nt-k)
      for (k=1;k<=nt;k=k+1)   write (1,*) 90+angle(k),radius(k)
      for (k=1;k<nt;k=k+1)    write (1,*) 180-angle(nt-k),radius(nt-k)
      for (k=1;k<=nt;k=k+1)   write (1,*) 180+angle(k),radius(k)
      for (k=1;k<nt;k=k+1)    write (1,*) 270-angle(nt-k),radius(nt-k)
      for (k=1;k<=nt;k=k+1)   write (1,*) 270+angle(k),radius(k)
      for (k=1;k<nt;k=k+1)    write (1,*) 360-angle(nt-k),radius(nt-k)


#     Set up the input variables for the subroutine solvde

      nyj    = ne
      nyk    = nt
      nci    = ne
      ncj    = ne-nb+1
      nck    = nt+1
      nsi    = ne
      nsj    = 2*ne+1
      indexv(1) = 2              # = first b.c. involves y(2)
      indexv(2) = 1

#     call the subroutine to obtain interface coordinates

      call solvde(itmax,conv,slowc,scalv,indexv,ne,nb,
                  nt,y,nyj,nyk,c,nci,ncj,nck,s,nsi,nsj)
```

```
#       Convert the interface coordinates of the solution into polar
#       coordinates

        for (k=1;k<=nt;k=k+1)
        {
              angle(k)   = atan2(y(2,k),y(1,k))*180/pi
              radius(k)  = sqrt(y(1,k)**2+y(2,k)**2)
              write (2,*) angle(k),radius(k)
        }

#       Write the polar coordinates of the solution into the file name(2)
#       We use the symmetry of the figures to generate the coordinates in
#       the range θ = (0,2π)

        for (k=1;k<nt;k=k+1)    write (2,*) 90-angle(nt-k),radius(nt-k)
        for (k=1;k<=nt;k=k+1)   write (2,*) 90+angle(k),radius(k)
        for (k=1;k<nt;k=k+1)    write (2,*) 180-angle(nt-k),radius(nt-k)
        for (k=1;k<=nt;k=k+1)   write (2,*) 180+angle(k),radius(k)
        for (k=1;k<nt;k=k+1)    write (2,*) 270-angle(nt-k),radius(nt-k)
        for (k=1;k<=nt;k=k+1)   write (2,*) 270+angle(k),radius(k)
        for (k=1;k<nt;k=k+1)    write (2,*) 360-angle(nt-k),radius(nt-k)

        stop
        end

*****************************************************************

#       subroutine  :       difeq.r
#       written by  :       Martin Muschol
#       update      :       24 Feb 91

#       purpose     :       This subroutine is part  of a  set of programs to
#                           calculate the 'equilibrum shape' of a two-dimensional
#                           with anisotropic surface tension sitting in a radially
#                           symmetric, linear temperature field of known shape.
#                           The main program is called gradcrys. This subroutine
#                           is called by the ODE-solver routine solvde. It purpose
#                           is to calculate the Ejk's and Sjk's defined in Eqns. (B.7)
#                           and (B.11) of this appendix.
#                           It is written in ratfor.
#
#       link to     :           - gradcrys.r
#                                   ( main program )
```

```
#                       - solvde.f, red.f ,pinvs.f, bksub.f
#                             (ODE-solver  routines from Numerical
#                             Recipices book)
#
#     Variables   :
#
#     do          = γ*T_m / L in [ μm K] . Lumped material parameter.
#                 Value used here is for SCN.
#     eps         surface tension anisotropy ( decimal number)
#     delb        = T_b [K]. Undercooling at the coordinate origin r=0.
#     Rx          = Rmax (in μm). Radius at which the undercooling
#     tmin,tmax   minimum,maximum value of θ. Here tmin = 0,
#                 tmax = π/4.
#     k           index of the interface point (x_k,y_k)
#     k1,k2       first,last interface point
#     nyk         number of interface points in the interval θ ∈ [0,π/4]
#     nyj         number of equations (here = 2)
#     nsi         number of rows in S_j,k
#     nsj         number of columns in S_j,k
#     y(nyj,nyk)  array containing the interface coordinates (x_k,y_k) with
#                 x_k = y(1,k) and y_k = y(2,k).
#     s(nsi,nsj)  These are the central variables of the algoritm.
#                 s(j,5) j=1,2 and k=2,..,nyk are the E_j,k's of Eq. (B.7a),
#                 while s(j,n) j=1,2,n=1,..,4 and k=2,...,nyk are the partial
#                 derivatives introduced in Eq. (B.11)
#     t(201)      array containing the normal angles θ_k. Note that the
#                 program works with an array of equally spaced points
#                 in this parameter.
#     dtgk        = (θ_k -θ_k-1) g(θ_k,k-1)     (see Eqns. (B.4) and(B.5))
#     cos_tgk     = A(θ_k -θ_k-1) cos(θ_k,k-1) (see Eqns. (B.5) and (B.8))
#     sin_tgk     = A(θ_k -θ_k-1) sin(θ_k,k-1) (see Eqns. (B.5) and (B.8))
#     delTk       = U(r_k,k-1)                  (see Eqns. (B.3) and (B.6))
#     ddel_dy1    = ∂_x U^-1(r_k,k-1)           (see Eq. (B14a))
#     ddel_dy2    = ∂_y U^-1(r_k,k-1)           (see Eq. (B14b))
#
#     For more detail see: W.H. Press et al., Numerical Recipes,
#     (Cambridge University Press, 1986) p588 f.
#
#*************************************************************#
```

```
subroutine difeq(k,k1,k2,jsf,is1,isf,indexv,ne,s,nsi,nsj,y,nyj,nyk)

      implicit double precision (a-h,o-z)
      dimension         y(nyj,nyk),s(nsi,nsj),indexv(nyj)
      double precision  do,eps,delb,Rx,dtgk,cos_tgk,
                        sin_tgk,delTk,ddel_dy1,ddel_dy2
      common /input1/   do,eps,delb,Rx
      common /input2/   tmin,tmax,t(201)

#     Evaluate all θk -dependent functions for internal points

      if (k != k1)
      {
      dtgk  = (t(k)-t(k-1))*do*
              (1-15*eps*cos(4*(.5*(t(k)+t(k-1)))))
      cos_tgk     = cos(.5*(t(k)+t(k-1)))*dtgk
      sin_tgk     = sin(.5*(t(k)+t(k-1)))*dtgk

#     Call a little subroutine to evaluate the temperature field and its
#     derivatives.

      call  lin_under(y(1,k),y(1,k-1),y(2,k),y(2,k-1),
                      delTk,ddel_dy1,ddel_dy2)
      }

#     If the point is at the first boundary (θ=0) evaluate Eqn. (B.19) and
#     B(20)

      if(k == k1)
      {
            s(2,indexv(1))     = 0
            s(2,indexv(2))     = 0
            s(2,2+indexv(1))   = tan(tmin)
            s(2,2+indexv(2))   = -1.
            s(2,jsf)           = -y(2,1)
      }

#     If the point is at the last boundary (θ=π/4) evaluate Eqn. (B.21) and
#     B(22)

      else if(k == k2+1)
      {
            s(1,indexv(1))     = 0.
```

```
            s(1,indexv(2))      = 0.
            s(1,2+indexv(1))    = 0
            s(1,2+indexv(2))    = -1
            s(1,jsf)            = y(1,k2)-y(2,k2)
      }

#     Now evaluate  Eqns (B.15), (B.16) and E_{j,k}

      else
      {
            s(1,indexv(1))      = -1+sin_tgk*ddel_dy1
            s(1,indexv(2))      = sin_tgk*ddel_dy2
            s(1,2+indexv(1)) = s(1,indexv(1))+2
            s(1,2+indexv(2)) = s(1,indexv(2))
            s(1,jsf)       = y(1,k)-y(1,k-1)+sin_tgk/delTk

            s(2,indexv(1))      = -cos_tgk*ddel_dy1
            s(2,indexv(2))      = -1-cos_tgk*ddel_dy2
            s(2,2+indexv(1)) = s(2,indexv(1))
            s(2,2+indexv(2)) = s(2,indexv(2))+2
            s(2,jsf)       = y(2,k)-y(2,k-1)-cos_tgk/delTk
      }
      return
      end

**************************************************************

      subroutine lin_under( xk, xk_1, yk, yk_1, delTk,
                  invdel_dx, invdel_dy )

      double precision   xk,xk_1,yk,yk_1,delTk,invdel_dx,
                         invdel_dy,x,y,R,do,eps,delb,Rx
      common /input1/  do,eps,delb,Rx

      x     = .5*(xk + xk_1)/Rx
      y     = .5*(yk + yk_1)/Rx
      R     =  sqrt(x**2 + y**2)

      delTk       = delb*(1 - R)
      invdel_dx   = .5*x/(delb*R*Rx*(1-R)**2)
      invdel_dy   = .5*y/(delb*R*Rx*(1-R)**2)
      return
      end
```

Appendix C

Image Analysis Procedures to Extract Interface Coordinates

C.1 Digital Images and Their Preprocessing

The video images of our crystal interfaces are digitized by a Data Translation *Quickcapture* video board with 640 x 480 pixel spatial resolution and 256 shades of gray. Each image point therefore is characterized by a triplet of integers (x,y,I) where (x,y) are its coordinates in units of pixels and I is its intensity value. For the following discussion we assume that white corresponds to I=0 and that black corresponds to I=256. The data are stored on the hard disk of our Mac II in TIFF-format. This special file format was developed to handle image-data and is described in detail e.g. in ref. [C.11]. We chose this file format since most commercial image processing programs are able to access it.

The image files are preprocessed using either *Image* or *Enhance*, the two commercial image analysis programs on our computer. The main purpose is to remove any specks of dirt from the images which might disturb our interface-extraction program. It is important to point out, however, that the quality of the original image is essential for good results. The images should have a very uniform background, preferably adjusted to be white, and the interface should be a dark, thin band against this background. Even sophisticated image processing software can't make up for a blurry image with weak contrast. Images with a background intensity different from white are thresholded: we subtract a fixed number from the intensity values of all pixels until the background intensity is close to zero.

After this preprocessing the images are ready for processing with our custom-programs.

C.2 Programs to Extract Interface Coordinates

All programs for extracting the interface coordinates were written in the C-language using MPW-C from APDA (Apple Program Developers Association). The goal of the programs is to extract a highly accurate set of polar interface coordinated (r_i,φ_i) of the crystal-melt interface. The task is divided into the following steps:

(1) Open the image files

The subroutine **ReadTiff** performs the task of opening the TIFF-files, reading their header information correctly and transferring the image data into computer memory for further processing. Note that each image contains 640 x 480 pixels with 256 different shades of gray. We store this information in a continuous one-dimensional array of length 640 x 480 = 307 200 bytes. The first 640 bytes represent the first row of the image, the next 640 bytes the second row and so on. The value of each byte represents the 2^8=256 intensity values the corresponding pixel can carry. A pointer to the array containing the image data and the dimensions of the image are passed back to the main program.

(2) Extract the 'features'

In the next step we extract a rough first estimate for the center of the crystal melt interface, which is assumed to be close to circular in shape. All pixels with intensity values higher than a given threshold are considered to be part of the interface and we call them features. The use of a threshold allows for small variations in the background intensity and noise.The

subroutine **MassCenter** performs the task of finding all the features in the image and determines a rough center of the crystal by calculating the "center of gravity" of all features giving each feature equal weight. Upon return the calling program obtains the x- and y-coordinates of the "center of gravity" (in pixels) and a count of how many features the image contains.

(3) Convert features to scaled polar coordinates

In the next step the main program, called **GetCirIfaceT**, converts the (x,y) coordinates of all feature pixels into polar coordinates (r,o) with the center of mass as preliminary origin of the coordinate system. At the same time the x- and y-scales are converted from pixels into μm. This eliminates the distortion of the images mentioned in section 5.2.3. The results of this conversion are stored in three arrays, one for the angular coordinate, one for the radius, and one for the intensity value of the feature.

(4) Sort the features with respect to the polar angle

The previous conversion is done by going through the image line by line and converting the feature coordinates as they are encountered. We now need to sort them with respect to the polar angle and reshuffle the two other arrays accordingly. A typical image contains several thousand features and a simple bubble sort algorithm would take about fifteen minutes on our computer. Since we have to perform this sorting task several times, we use a fast sorting subroutine, called **Indexx**. It is again taken from the Numerical Recipes book of Press et al. [P4].

(5) Extract a set of polar interface coordinates

So far the interface is still a band of features with varying intensity and radial distances. In the next step we use the intensity profile across the interface to obtain an interface position with sub-pixel resolution. The features are divided into angular slices of typically 1-3° degrees. The slices are chosen small enough to consider the corresponding interface segment as essentially flat (given a typical radius of about 160 pixels of the interface). A typical slice will contain about 10 features. We drop the angular dependence of the features within each slice and fit a parabola through the radial intensity profile I(r). A typical intensity profile is shown in Fig. 32. The result is a set of interface coordinates (r_i,ϕ_i) with a resolution of about 0.2 pixels for the radial distance r_i. The program **FitIntToPar** performs the parabolic least square fit of the intensity profile just discussed and returns the extracted polar interface coordinates (r_1,ϕ_1).

(6) Correct the crystal center and recalculate the interface coordinates

The interface coordinates (r_1,ϕ_1) extracted in the previous step were dependent on the position of the coordinate origin determined by the subroutine **MassCenter**. We correct the position of the crystal origin by fitting the extracted interface coordinates with a least-square fit routine to the shape of a circle and making the center of the circle a fitting parameter. This provides a correction for the coordinate origin. The subroutine performing this task is called **LsqCircle**.

(7) Repeat step (4) to (6) twice

We reevaluate the polar coordinates of all image features using the newly extracted coordinate origin, resort them and extract the interface coordinates again. This way we correct the errors introduced by using an incorrect origin. After running through this loop three times the resulting

corrections of the interface coordinates are negligible. The final set of interface coordinates is stored in a file and provides the input to our Fourier analysis.

Table 1: Definitions of rescaled quatities for pure and binary sytems.

Quantity	pure melts	binary mixtures
dim.less diffusion field	$u(\vec{r}) = \frac{T_\infty - T_m}{L / c_p}$	$u(\vec{r}) = \frac{C(\vec{r}) - C_\infty^{eq}}{\Delta C}$
dim.less undercooling / supersaturation	$\Delta = \frac{T_\infty - T_m}{L / c_p}$	$\Delta = \frac{C_\infty - C_\infty^{eq}}{\Delta C}$
unit undercooling / unit supersaturation	L / c_p	$\Delta C = C_\infty(1-k)/k$
capillary length	$d_o^{th} = \frac{\gamma}{L} \frac{T_m}{L / c_p}$	$d_o^{chem} = \frac{\gamma}{L} \frac{T_m}{m_L \Delta C}$
selection parameter	$\sigma^* = \frac{2 d_o^{th} D_T}{\rho^2 v}$	$\sigma^* = \frac{2 d_o^{chem} D_{chem}}{\rho^2 v}$

In the above table C_∞ is the actual solute concentration at the set temperature T of the solution, C_∞^{eq} is the corresponding equilibrium solute concentration at that temperature, $m_L = dT_{eq}/dC$ is the slope of the liquidus in the binary phase diagram and $k = C_S/C_l$ is the segregation coefficient.

Table 2: Relevant physical properties of materials reviewed in chapter 4.2. Underlined values are based on estimates. Values in italics have been cited in the given reference without identification of their source.

		SCN	PVA	CMP	CHXL	Water	^{4}He(1)	Kr	Xe
mol. wt.	[g/mol]	80.09 W4	102.13 M10	136.23 M10	100.16 M10	18.015 H11	4.0026 H11	83.80 H11	131.30 H11
crys. str	---	bcc W4	*fcc* R2	bcc J6	fcc J6	hex	hcp / fcc F1	fcc A3	fcc A3
T_m	[°C]	58.080 R1	35.935 S8	53.05 R3	25.15 H11	0.00 H11	-238.11 F1	-111.76 B18	-157.39 B18
L	[J/mol]	3703 W4	*2267* R2	2390 R3	1751 S7	6008 H11	263.9 F1	1639 B18	2299 B18
C_p(liq)	[J/mol K]	160.0 W4	*204.26* R2	279 R3	206.9 S7	75.97 H11	11.9 F1	43.0 B18	44.6 B18
C_p(sol)	[J/mol K]	154.8 W4	*183.94* R2	251 R3	---	38.44 H11	12.0 F1	35.7 B18	37.0 B18
D_T(liq)	x10^{-3}[cm^2/s]	1.14 G2	*0.70* R2	0.65 R3	*0.62* S7	1.32 T4	6.62 F1	7.42 B18	7.29 B18
D_T(sol)	x10^{-3}[cm^2/s]	1.16 G2	*0.74* R2	0.77 R3	----	13.5 T4	0.96 F1	2.08 B18	4.96 B18
γ_o	x10^{-7}[J/cm^2]	8.94 S9	2.84 S8	0.97 R3	4(2) S7	16 H12	2.5 F1	90 B18	110 B18
ρ(liq)	[g/cm^3]	0.970 W4	*0.908* R2	0.800 R3	----	0.9998 H11	0.4105 F1	----	----
ρ(sol)	[g/cm^3]	1.016 W4	*0.946* R2	*0.879* R3	0.965 S7	0.9168 H11	0.4281 F1	----	----

(1) values for p=4200 bar
(2) value quoted in [S7] has wrong units and might be misprint

Table 3: Experimentally determined values of selection parameter $\sigma^*_{exp} = 2d_0D/v\rho^2$ and surface tension anisotropy ε_m; d = dimension of experiment; all anisotropy values are for four-fold symmetric materials,except for ice and HET.

Material	σ^*_{exp}	peclet number	d	Ref.	ε_m (%)	Ref.
SCN	0.0195	$2x10^{-4}$ - $3x10^{-2}$	3	H2	0.5	G5
PVA	0.022	$9x10^{-4}$ - $1x10^{-3}$	3	S6	5	R2
PVA+1%eth.	0.05±0.02	$8x10^{-3}$ - $5x10^{-2}$	3	D3	0.6±0.2	D3
Cyclohex.	0.027	$2x10^{-3}$ - $4x10^{-2}$	3	S7	----	---
Camphene	----	----	3	----	3(2)	R3
NH_4Br (soln.)	0.081±0.02	$5x10^{-4}$ - $2x10^{-3}$	3	D4	1.6±0.4	D4
NH_4Br (soln.)	0.072±0.037	$1x10^{-3}$ - $5x10^{-3}$	3	H6	----	---
NH_4Br (gel)	0.120±0.025	----	3	M9	----	---
Helium	0.0013	$2x10^{-3}$ - $2x10^{-2}$	3	F1	----	---
Krypton	0.017±0.009	$2x10^{-5}$ - $1x10^{-3}$	3	B18	----	---
Xenon	0.022±0.012	$1x10^{-5}$ - $8x10^{-4}$	3	B18	----	---
Ice	0.025	----	3	F2	----	---
Ice	0.075(1)	$5x10^{-5}$ - $2x10^{-3}$	3	K13	0.2±0.1	K13
HET	0.038	$3x10^{-3}$	2	O3	0.3±0.1	O3

(1) From Fig. 13 in ref. [K13]

(2) based on twofold shape distortion

Table 4: Summary of the j=2,4 and j=8 shape anisotropies for a series of experiments with SCN, PVA and PVA/Ethanol samples. Note the scatter in the data due to orientational effects.

	s_2 [%]	s_4 [%]	s_8 [%]
SCN:			
23. Apr. 91	0.23 ± 0.25	0.41 ± 0.02	0.026 ± 0.009
23. May 91	0.18 ± 0.12	0.45 ± 0.015	0.023 ± 0.005
13. June 91	0.11 ± 0.03	0.53 ± 0.01	0.029 ± 0.005
20. June 91	0.16 ± 0.15	0.51 ± 0.02	0.027 ± 0.008
02. Oct. 91	0.074 ± 0.02	0.571 ± 0.02	0.037 ± 0.003
final result	---	$\varepsilon_4 = 0.55 \pm 0.15$	$\varepsilon_8 \leq 0.025$ (1)
PVA:			
08.July 91	0.51 ± 0.27	1.81 ± 0.06	0.076 ± 0.017
14. Aug. 91	0.88 ± 0.37	1.45 ± 0.10	0.049 ± 0.025
16. Aug. 91	0.53 ± 0.07	2.25 ± 0.07	0.123 ± 0.007
28. Aug. 91	0.56 ± 0.22	2.47 ± 0.07	0.15 ± 0.015
04. Sept. 91	0.52 ± 0.07	1.91 ± 0.06	0.11 ± 0.020
final result	---	$\varepsilon_4 = 2.5 \pm 0.2$	$\varepsilon_8 \leq -0.09$ (1)
PVA/Ethanol			
26. July 91	1.15 ± 0.27	2.00 ± 0.13	0.080 ± 0.013
01. Aug. 91	1.35 ± 0.21	2.22 ± 0.15	0.114 ± 0.016
03. Aug. 91	1.06 ± 0.31	2.21 ± 0.16	0.128 ± 0.022
06. Aug. 91	1.10 ± 0.14	1.90 ± 0.06	0.065 ± 0.011
14. Oct. 91	0.48 ± 0.03	2.26 ± 0.03	0.137 ± 0.036
15. Oct. 91	0.18 ± 0.10	2.65 ± 0.07	0.16 ± 0.02
final result	---	$\varepsilon_4 = 2.6 \pm 0.2$	$\varepsilon_8 \leq -0.1$ (1)

(1) The final estimates for ε_8 have the contribution from ε_4 subtracted (see Fig.17)

Table 5: σ^*_{th} computed from experimentally determined surface tension anisotropy $\gamma(\theta) = \gamma_o [1 + \varepsilon_m(\cos(m\theta))]$ - comparison with σ^*_{exp}

Material	m	$\varepsilon_m(\%)$	Ref.	$\alpha = (m^2-1)\varepsilon_m$	μ	σ^*_{th}	σ^*_{exp}	Ref.
A: Previous Measurements								
SCN	4	0.5	H2	.075	0.97	0.009	0.0195	H2
PVA	4	5	S6	0.75	0.95	0.14	0.022	S6
PVA+1%ethanol	4	0.6±0.2	D3	0.09±0.03	0	0.024±0.01	0.05±0.02	D3
NH4Br (solution)	4	1.6±0.4	D4	0.24±0.06	0	0.072±0.018	0.081±0.02	D4
HET (solution)	6	0.3±0.1(1)	O3	0.11±0.04	0	0.033±0.014	0.038	O3
Ice	6	0.2±0.1	K13	0.07±0.03	0.5	0.012±0.005	≈ 0.075	K13
B: This Work								
SCN	4	0.55±0.15		0.083±0.023	0.97	0.011±0.004	0.0195	H2
PVA	4	2.5±0.2		0.375±0.03	0.95	0.054±0.004	0.022	S6
PVA+1%ethanol	4	2.6±0.2		0.390±0.03	0.95	0.107±0.007	0.05±0.02	D3

(1) This is 1/35 times the value cited in ref. [O3] and corresponds to their Eq.(5) revised to read $R(\theta) = R_o [1-\varepsilon_6\cos(6\theta)]$

References

[A1] Handbook of Mathematical Functions, ed. by M. Abramowitz and I.A. Stegun, (National Bureau of Standards, Washington, 1967), p. 376

[A2] S. Arora, A. Buka, P. Palffy-Muhoray, Z. Racz, and R. Vora, Europhys. Lett. **7**, 43 (1988)

[A3] AIP Handbook, 2nd. ed. (McGraw Hill, New York, 1963)

[B1] D. Bensimon, L.P. Kadanoff, S. Liang, B.I. Shraiman, and C. Tang, Rev. Mod. Phys. **58**, 977 (1986)

[B2] E.A. Brener and V.I. Mel'nikov, Advan. Phys. **40**, 53 (1991)

[B3] E. Ben-Jacob, Nigel Goldenfeld, J.S. Langer, and Gerd Schön, Phys. Rev. A **29**, 330 (1984)

[B4] E. Ben Jacob, N. Goldenfeld, B.G. Kotliar, and J.S. Langer, Phys. Rev. Lett. **51**, 1930 (1983)

[B5] E. Ben Jacob, N. Goldenfeld, B.G. Kotliar, and J.S. Langer, Phys. Rev. Lett. **53**, 2110 (1984)

[B6] R.C. Brower, D.A. Kessler, J. Koplik, and H. Levine, Phys. Rev. Lett. **51**, 1111 (1983)

[B7] R.C. Brower, D.A. Kessler, J. Koplik, and H. Levine, Phys. Rev. A **29**, 1335 (1984)

[B8] R.C. Brower, D.A. Kessler, J. Koplik, and H. Levine, Scripta Metall. **13**, 463 (1984)

[B9] M. Ben Amar and Y. Pomeau, Europhys. Lett. **2**, 307 (1986)

[B10] A. Barbieri, D.C. Hong, and J.S. Langer, Phys. Rev. A **35**, 1802, (1987)

[B11] D. Bensimon, P. Pelce, and B.I. Shraiman, J. Physique **48**, 2081 (1987)

[B12] E.A. Brener, C.E. Esipov, and V.I. Mel'nikov, Pis'ma Zh.E.T.F. **45**, 595 (1987)

[B13] E.A. Brener, C.E. Esipov, and V.I. Mel'nikov, Sov. Phys. JETP **67**, 565 (1988)

[B14] E.A. Brener, M.B. Geilikman, and D.E. Temkin, Sov. Phys. JETP **67**, 1002 (1988)

[B15] A. Barbieri and J.S. Langer, Phys. Rev A **39**, 5314 (1989)

[B16] E.A. Brener and V.I. Mel'nikov, Advan. Mod. Phys. **40**, 53 (1991)

[B17] J.H. Bilgram, M. Firmann, and W. Känzig, Phys. Rev. B **37**, 685 (1988)

[B18] J.H. Bilgram, M. Firmann, and E. Hürlimann, J. Crystal Growth **96**, 175 (1989)

[B19] T. Bolthauser, E. Hürlimann, and J.H. Bilgram, Helv. Phys. Acta **61**, 189 (1988)

[B20] J.H. Bilgram and E. Hürlimann, in Proceedings VIIth. European Symposium on Materials and Fluids in Microgravity, (Oxford, U.K., 1990), p. 173

[B21] A. Buka and P. Palffy-Muhoray, J. Phys. France **49**, 1319 (1988)

[B22] M. Ben Amar (private communication)

[B23] E. Brener (private communication)

[B24] Yu. A. Bychkov and S.V. Iordansky, J. Phys. Chem. Solids **43**, 377 (1982)

[C1] S. Coriell and R.L.Parker, J. Appl. Phys. **36**, 632 (1965)

[C2] S.R. Coriell and R.L. Parker, in Crystal Growth, ed. by H.S.Peiser (Pergamon Press, Oxford, U.K.,1967)

[C3] S.R.Coriell and R.F.Sekerka, J. Crystal Growth **34**, 157 (1976)

[C4] H.S. Carslaw and J.C. Jaeger, Conduction of Heat in Solids, 2nd. Ed., p. 282 (Claderon, Oxford 1959)

[C5] B. Caroli, C. Caroli, B. Roulet, and J.S. Langer, Phys. Rev. A **33**, 442 (1986)

[C6] B. Caroli, C. Caroli, C. Misbah, and B. Roulet, J. Physique **47**, 1623, (1986)

[C7] B. Caroli, C. Caroli, C. Misbah, and B. Roulet, J. Physique **48**, 547 (1987)

[C8] J.W. Cahn and D.W. Hoffman, Acta Met. **22**, 1205 (1974)

[C9] B. Chalmers, The Principles of Solidification, (Wiley, New York, 1968)

[C10] S.K. Chan, H.-H. Reimer, and M. Kahlweit, J. Crystal Growth **32**, 303 (1976)

[C11] C.A. Lindley, Practical Image Processing in C, (Wiley & Sons, New York, 1990), p. 231 f.

[C12] Y. Couder, N. Gérard, and M. Rabaud, Phys. Rev. A **34**, 1986

[D1] A. Dougherty, P.D. Kaplan, and J.P. Gollub, Phys. Rev. Lett. **58**, 1652 (1987)

[D2] S. de Cheveigné, C. Guthmann, P. Kurowski, E. Vicente, and H. Biloni, J. Crystal Growth **92**, 616 (1988)

[D3] A. Dougherty, J. Crystal Growth **110**, 501 (1991)

[D4] A. Dougherty and J.P. Gollub, Phys. Rev. A **38**, 3043 (1988)

[D5] A. Dougherty, P.D. Kaplan, and J.P. Gollub, Phys. Rev. Lett. **58**, 1652 (1987)

[F1] J.P. Franck and J. Jung, J. Low Temp. Phys. **64**, 165 (1986)

[F2] T. Fujioka, Ph.D. Thesis, Carnegie-Mellon University (1978)

[G1] M.E. Glicksman and P.W. Voorhees, Met. Trans. A **15**, 995 (1984)

[G2] M.E.Glicksman, R.J.Schaefer, and J.D.Ayers, Met. Trans. A **7**, 1747 (1976)

[G3] M.E. Glicksman, in Solidification, (American Metals Society, Metals Park, Ohio, 1971), p. 155 f.

[G4] M.E. Glicksman, N.B. Singh, and M. Chopra, in Materials Processing in the Reduced Gravity Environment of Space, ed. by G.E. Rindone (Elsevier Science Publication, The Netherlands, 1982) p. 461 f.

[G5] M.E. Glicksman and N.B. Singh, in Rapidly Solidified Powder Aluminum Alloys, ed. by M.E. Fine and E.A. Starke,Jr. (American Society of Testing and Materials, Philadelphia, 1986) p. 44 f.

[G6] M.E. Glicksman and R.J. Schaefer, Acta. Met. **14**, 1126 (1966)

[H1] H. Chou and H.Z. Cummins, Phys. Rev. Lett. **61**, 173 (1988)

[H2] S.-C. Huang and M.E. Glicksman, Acta Met. **29**, 701 (1981)

[H3] C. Herring, in Structure and Properties of Solid Surfaces, ed. by R. Gomer and C.S. Smith (Chicago University Press, Chicago, 1953)

[H4] C. Herring, Phys. Rev. **82**, 87 (1951)

[H5] J.D. Hunt, K.A. Jackson, and H. Brown, Rev. Sci. Instr. **37**, 805 (1986)

[H6] H. Honjo and Y. Sawada, J. Crystal Growth **58**, 297 (1982)

[H7] H. Honjo, S. Ohta, and M. Matsushita, Phys. Rev. A **36**, 4555 (1987)

[H8] H. Honjo, S. Ohta, and Y. Sawada, Phys. Rev. Lett. **55**, 841 (1985)

[H9] H. Honjo, S. Ohta, and M Matsushita, J. Phys. Soc. Jpn **55**, 2487 (1986)

[H10] J. Hallet, J. Atmos. Sci. **21**, 671 (1964)

[H11] Handbook of Chemistry and Physics, 60th. ed. (CRC Press, Florida, 1979)

[H12] S.C. Hardy and S.R. Coriell, J. Crystal Growth **3**, 569 (1968)

[I1] G.P. Ivantsov, Dokl. Akad. Nauk. SSSR **58**, 567 (1947)

[J1] D. Jasnow and J. Viñals, Phys. Rev. A **40**, 3864 (1989)

[J2] D. Jasnow and J. Viñals, Phys. Rev. A **41**, 6910 (1990)

[J3] K.A. Jackson, D.R. Uhlmann, and J.D. Hunt, J. Crystal Growth **1**, 1 (1967)

[J4] K.A. Jackson, in Liquid Metals and Solidification, (American Society of Metals,

Cleveland, 1958), p. 174

[J5] K.A. Jackson, in Growth and Perfection of Crystals, ed. by R.H. Doremus, D. Turnbull and B.W. Roberts (Wiley, New York, 1958)

[J6] K.A. Jackson and J.D. Hunt, Acta Met. **13**, 1212 (1965)

[K1] W. Kurz and D.J. Fisher, Fundamentals of Solidification, (Trans Tech, Switzerland 1984), p. 14

[K2] D.A. Kessler, J.Koplik, and H. Levine, Phys. Rev. A **30**, 2820 (1984)

[K3] D.A. Kessler, J.Koplik, and H. Levine, Phys. Rev. A **30**, 3161 (1984)

[K4] D.A. Kessler, J.Koplik, and H. Levine, Phys. Rev. A **31**, 1712 (1984)

[K5] D.A. Kessler, J.Koplik, and H. Levine, Phys. Rev. A **33**, 3352 (1986)

[K6] D.A. Kessler and H. Levine, Phys. Rev. B **33**, 3069 (1986)

[K7] D.A. Kessler and H. Levine, Phys. Rev. Lett. **57**, 2704 (1986)

[K8] D.A. Kessler and H. Levine, Phys. Rev. A **36**, 4123 (1987)

[K9] D.A. Kessler and H. Levine, Phys. Rev. A **34**, 4980 (1986)

[K10] D.A. Kessler and H. Levine, Advan. Phys. **37**, 255 (1988)

[K11] W. Kurz and D.J. Fisher, Fundamentals of Solidification, (Trans Tech, Switzerland 1984), p. 3

[K12] A. Karma and J.S. Langer, Phys. Rev. A **30**, 3147 (1984)

[K13] K. Koo, R. Ananth, and W.N. Gill, Phys. Rev. A **44**, 3782 (1991)

[K14] J.P. Kallungal and A.J. Barduhn, AIChE J. **23**, 294 (1977)

[L1] J.S.Langer, Rev. Mod. Phys. **52**, 1 (1980)

[L2] J.S.Langer and H.Müller-Krumbhaar, J. Crystal Growth **42**, 11 (1977)

[L3] J.S.Langer and H.Müller-Krumbhaar, Acta metall. **26**, 1681 (1978)

[L4] J.S.Langer and H.Müller-Krumbhaar, Acta metall. **26**, 1689 (1978)

[L5] J.S.Langer and H.Müller-Krumbhaar, Acta metall. **26**, 1697 (1978)

[L6] J.S.Langer and H.Müller-Krumbhaar, Phys. Rev. A **27**, 499 (1983)

[L7] J.S. Langer, Mat. Science and Engineering **65**, 37 (1983)

[L8] M.A. Lemieux, J. Liu, and G. Kotliar, Phys. Rev. A **36**, 1849 (1987)

[L9] J. Lipton, M.E. Glicksman, and W. Kurz, Mat. Sci. Eng. **65**, 57 (1984)

[L10] J. Lipton, M.E. Glicksman, and W. Kurz, Metall. Trans. A **18**, 341 (1987)

[L11] F. Liu and N. Goldenfeld, Phys. Rev. A **42**, 5052 (1990)

[L12] C. Lindenmeyer and B. Chalmers, J. Chem. Phys. **45**, 2807 (1966)

[M1] W.W. Mullins and R.F. Sekerka, J. Appl. Phys. **34**, 323 (1963)

[M2] W.W. Mullins and R.F. Sekerka, J. Appl. Phys. **35**, 444 (1964)

[M3] J.W. McLean and P.G. Saffman, J. Fluid Mech. **102**, 455 (1981)

[M4] D.I. Meiron, Phys. Rev. A **33**, 2704 (1986)

[M5] W.W.Mullins, in Metal Surfaces: Structure, Energetics and Kinetics, American Society of Metals (Metals Park, Ohio 1963)

[M6] J. Maurer, P. Bouissou, B. Perrin, and P. Tabeling, Europhys. Lett.**8**, 67 (1989)

[M7] W.C. Macklin and B.F. Ryan, Philos. Mag. **4**, 847 (1966)

[M8] W.C. Macklin and B.F. Ryan, Philos. Mag. **17**, 83 (1968)

[M9] J. Maurer, B. Perrin, and P. Tabeling, Europhys. Lett. **14**, 575 (1991)

[M10] The Merck Index, 10th. ed. (Merck&Co, New Jersey, 1983)

[O1] D.E.Ovsienko and G.A.Alfintsev, in Crystal Growth, Properties and Applications ed. by H.C. Freyhardt (Springer-Verlag, Berlin 1980)

[O2] S. Ohta and H. Honjo, Phys. Rev. Lett. **60**, 611 (1988)

[O3] P. Oswald, J. Phys. France **49**, 1083 (1988)

[O4] P. Oswald, J. Malthête, and P. Pelcé, J. Phys France **50**, 2121 (1989)

[P1] Dymanics of Curved Fronts, ed. by P. Pelcé (Academic Press, New York, 1988)

[P2] R. Pieters and J.S. Langer, Phys. Rev. Lett. **56**, 1948 (1986)

[P3] P.Pelce and Y.Pomeau, Studies in Applied Maths. **74**, 245 (1986)

[P4] W.H. Press, B.P. Flannery, S.A. Teukolsky, and W.T. Vetterling, Numerical Recipes (Cambridge University Press, New York, 1986), p. 588 ff

[P5] H.R. Pruppacher, J. Colloid Interface Sci. **25**, 285 (1967)

[P6] V.K. Pinus and P.L Taylor, Phys. Rev. B **32**, 5362 (1985)

[P7] V.K. Pinus and P.L. Taylor, Phys. Rev. B 33, 8697 (1986)

[R1] E. Rubinstein, M.E. Glicksman, B.W. Magnum, Q.T. Fang, and N.B. Singh, J. Crystal Growth **89**, 101 (1988)

[R2] E.R. Rubinstein and M.E. Glicksman, J. Crystal Growth **112**, 84 (1991)

[R3] E.R. Rubinstein and M.E. Glicksman, J. Crystal Growth **112**, 97 (1991)

[R4] E. Raz, S.G. Lipson, and E. Polturak, Phys. Rev A **40**, 1088 (1991)

[S1] J.Strain, Physica D **30**, 297 (1988)

[S2] R.J. Schaefer and S.R.Coriell, Met. Trans. A **15**, 2109 (1984)

[S3] R.F.Sekerka, R.G.Seidensticker, D.R.Hamilton, and J.D.Harrison, Investigation of desalination by freezing, Westinghouse Research Laboratory Report, chap.3 (1967)

[S4] P.G. Saffman and G.I. Taylor, Proc. Roy. Soc. London, Ser. A **245**, 312 (1958)

[S5] Y.Saito, G. Goldbeck-Wood, and H.Müller-Krumbhaar, Phys. Rev. Lett. **58**, 1541 (1987) and Phys. Rev. A **38**, 2148 (1988)

[S6] N.B. Singh and M.E. Glicksman, J. Crystal Growth **98**, 277 (1989)

[S7] N.B. Singh and M.E. Glicksman, J. Crystal Growth **98**, 534 (1989)

[S8] N.B. Singh and M.E. Glicksman, J. Crystal Growth **98**, 573 (1989)

[S9] R.J. Schaefer, M.E. Glicksman and J.D. Ayers, Phil. Mag. **32**, 725 (1975)

[T1] D.E.Temkin, Dokl. Akad. Nauk. SSSR **132**, 1307 (1960)

[T2] S.H. Tirmizi and W.N. Gill, J. Crystal Growth **85**, 488 (1987)

[T3] S.H. Tirmizi and W.N. Gill, J. Crystal Growth **96**, 277 (1989)

[T4] Thermophysical Properties of Matter, vol. 10, Thermal Diffusivities (IFI/Plenum Data Corp., New York, 1973), p390

[T5] P. Tabeling and A.Libchaber, Phys. Rev. A **33**, 794 (1986)

[V1] J. Vanden-Broeck, Phys. Fluids **26**, 2033 (1983)

[V2] P.W. Voorhees, S.R. Coriell, G.B. McFadden, and R.F. Sekerka, J. Crystal Growth **67**, 425 (1984)

[W1] see e.g.: D.P.Woodruff, The solid-liquid interface, (Cambridge University Press, London 1973)

[W2] G. Wulff, Z. Krist. **34**, 449 (1901)

[W3] R.B. Williamson and B. Chalmers, in Crystal Growth, ed. by H.S. Peiser (Pergamon Press, Oxford, U.K.,1967), p. 739

[W4] C.A. Wulff and E.F. Westrum, Jr., J. Phys. Chem. **67**, 2376 (1963)

[Z1] C. Zener, J. Appl. Phys. **20**, 950 (1949)